The Hydroclimate of East Africa: Seasonal cycle, Decadal Variability, and Human-induced Climate Change

Wenchang Yang

Submitted in partial fulfillment of the
requirements for the degree
of Doctor of Philosophy
in the Graduate School of Arts and Sciences

COLUMBIA UNIVERSITY

2015

ABSTRACT

The Hydroclimate of East Africa: Seasonal cycle, Decadal Variability, and Human-induced Climate Change

Wenchang Yang

The hydroclimate of East Africa shows distinctive variabilities on seasonal to decadal time scales and poses a great challenge to climatologists attempting to project its response to anthropogenic emissions of greenhouse gases (GHGs). Increased frequency and intensity of droughts over East Africa in recent decades raise the question of whether the drying trend will continue into the future. To address this question, we first examine the decadal variability of the East African rainfall during March–May (MAM, the major rainy season in East Africa) and assess how well a series of models simulate the observed features. Observational results show that the drying trend during MAM is associated with decadal natural variability of sea surface temperature (SST) variations over the Pacific Ocean. The multimodel mean of the SST-forced, Coupled Model Intercomparison Project Phase 5 (CMIP5) AMIP experiment models reproduces both the climatological annual cycle and the drying trend in recent decades. The fully coupled models from the CMIP5 historical experiment, however, have systematic errors in simulating the East African rainfall annual cycle by underestimating the MAM rainfall while overestimating the October–December (OND, the second rainy season in East Africa) rainfall. The multimodel mean of the historical coupled runs of the MAM rainfall anomalies, which is the best estimate of the radiatively-forced change, shows a weak wetting trend associated with anthropogenic forcing. However, the SST anomaly pattern associated with the MAM rainfall has large discrepancies with the observations.

The errors in simulating the East African hydroclimate with coupled models raise

questions about how reliable model projections of future East African climate are. This motivates a fundamental study of why East African climate is the way it is and why coupled models get it wrong. East African hydroclimate is characterized by a dry annual mean climatology compared to other deep tropical land areas and a bimodal annual cycle with the major rainy season during MAM (often called the "long rains" by local people) and the second during OND (the "short rains"). To explore these distinctive features, we use the ERA-Interim Re-Analysis data to analyze the associated annual cycles of atmospheric convective stability, circulation and moisture budget. The atmosphere over East Africa is found to be convectively stable, in general, year-round but with an annual cycle dominated by the surface moist static energy (MSE), which is in phase with the precipitation annual cycle. Throughout the year, the atmospheric circulation is dominated by a pattern of convergence near the surface, divergence in the lower troposphere and convergence again at upper levels. Consistently, the convergence of the vertically integrated moisture flux is mostly negative across the year, but becomes weakly positive in the two rainy seasons. It is suggested the semi-arid/arid climate in East Africa and its bimodal rainfall annual cycle can be explained by the ventilation mechanism, in which the atmospheric convective stability over East Africa is controlled by the import of low MSE air from the relatively cool Indian Ocean off the coast and the cold winter hemisphere. During the rainy seasons, however, the off-coast SST increases (and is warmest during the long rains season) and the northerly or southerly weakens, and consequently the air imported into East Africa becomes less stable.

The MSE framework is then applied to study the coupling-induced bias of the East African rainfall annual cycle often found in CMIP3/5 coupled models that overestimates the OND rainfall and underestimates the MAM rainfall, by comparing the historical (coupled) and the AMIP runs (SST-forced) for each model. It is found that a warm north and cold south SST bias over the Indian Ocean induced in coupled models is responsible for the dry MAM rainfall bias over East Africa while the ocean dynamics induced warm west and cold east SST bias over the Indian Ocean contributes to the wet OND rainfall bias in East Africa.

Finally, to understand the East African regional climate in the context of the broader tropical climate and circulation, zonal momentum balance of the tropical atmospheric circulation during the global monsoon mature months (January and July) are analyzed in three dimensions based on the ERA-Interim Re-Analysis. It is found that the dominant terms in the balance of the atmospheric boundary layer (ABL) in both months are the pressure gradient force, the Coriolis force and friction. The nonlinear advection term plays a significant role only in the Asian summer monsoon regions including off East Africa. In the upper troposphere, the pressure gradient force, the Coriolis force and nonlinear advection are the dominant terms. The transient eddy force and the residual force (which can be explained as convective momentum transfer over open oceans) are secondary yet can not be neglected near the equator. Zonal mean equatorial upper troposphere easterlies are maintained by the absolute angular momentum advection associated with the cross-equatorial Hadley circulation. Equatorial upper troposphere easterlies over the Asian monsoon regions are also controllled by the absolute angular momentum advection but are mainly maintained by the pressure gradient force in January. The equivalent linear Rayleigh friction, which is widely applied in simple tropical models, is calculated and the corresponding spatial distribution of local coefficient and damping time scale are estimated from the linear regression. It is found that the linear momentum model is in general capable of crudely describing the tropical atmospheric circulation dynamics yet the caveat should be kept in mind that the friction coefficient is not uniformly distributed and is even negative in some regions.

TABLE OF CONTENTS

LIST OF TABLES

LIST OF FIGURES

ACKNOWLEDGMENTS

First of all, I would like to express my deepest gratitude to my advisors Professor Richard Seager and Professor Mark A. Cane, and to my third committee member Professor Mingfang Ting, for their excellent mentorship, continuous encouragement, strong support and great patience, without which this thesis would not have been possible.

I would like to extend my kind regards to Dr. Bradfield Lyon, who brought me into the field of East African hyroclimate research and inspired me in writing this thesis. I also wish to thank Professor William Boos for kindly agreeing to serve on my thesis committee.

I would also like to show my gratitude to Dr. Naomi Henderson, Dr. Lawrence Rosen, Dr. Haibo Liu and Dr. Jennifer Nakamura for their computational support and contribution to this work, and to everyone in the Division of Ocean and Climate Physics (DOCP) at the Lamont-Doherty Earth Observatory (LDEO) for their helpful guidance and discussions as well as the enjoyable atmosphere they have created here.

I owe a tremendous debt of gratitude to my parents as well as other family members, who have always been so supportive with their best wishes. Last but not least, I would like to thank my wife, Shichong Liu, for her love and support.

To my daughter Rosalyn Haining Yang.

CHAPTER 1

Introduction

East Africa is a region of unique hydroclimate in the deep tropics, with annual mean precipitation largely much lower than other land areas of similar latitudes and a bimodal annual cycle of precipitation over much of the region (Yang et al., 2014a). The two rainy seasons are March–May (MAM) and October–December (OND), which are usually called by local people the "long rains" and the "short rains", respectively. There is generally little rainfall over much of East Africa during January–February (JF) or June–September (JJAS), when many monsoon systems in the southern or northern hemisphere are established. The interannual variability of East African rainfall is dominated by the short rains (Beltrando, 1990; Camberlin and Wairoto, 1997; Mutai and Ward, 2000; Nicholson, 2000; Lyon, 2014), which correlate well with El Niño-Southern Oscillation (ENSO) (Beltrando, 1990; Beltrando and Camberlin, 1993; Goddard and Graham, 1999; Indeje et al., 2000; Schreck and Semazzi, 2004), with above (below) normal rainfall during El Niño (La Niña) events. However, no such strong correlation with large scale climate anomalies has been found for the MAM long rains (Ogallo, 1988; Hastenrath et al., 1993; Okoola, 1999; Camberlin and Okoola, 2003; Pohl and Camberlin, 2011).

There was a severe drought in East Africa during 2010–2011, the worst drought to occur in the region in the last 60 years, placing millions of people into a humanitarian crisis in this politically and socioeconomically vulnerable region (FEWS NET, 2011; Lyon and DeWitt, 2012; Dutra et al., 2013). The drought was characterized by failure of both the 2010 short rains and the subsequent 2011 long rains. While the short rains failure was expected and successfully predicted on the basis of La Niña conditions in 2010 (Dutra et al., 2013) given the robust relationship with ENSO, there was difficulty in explaining the long rains failure since no robust large scale forcing of the precipitation in this season, either oceanic or atmospheric, had been identified in past studies.

Lyon and DeWitt (2012) considered the below normal long rains in 2011 against a

longer time scale background and found it is associated with an abrupt change in MAM precipitation over East Africa in 1998–99. Based on observational analysis and global climate model (GCM) simulations, they further linked the drying with a shift to warmer sea surface temperatures (SSTs) over the western topical Pacific and cooler SSTs over the central and eastern tropical Pacific but found little or no relationship with SSTs over the Indian Ocean. More recently, Lyon et al. (2013) have shown that the shift is part of natural multidecadal variability in the Pacific. The decline of the long rains in recent decades has also been documented in other related studies (Funk et al., 2008; Williams and Funk, 2011), yet a different mechanism was proposed to explain the decline. Williams and Funk (2011) associated the drying trend with an anthropogenic-forced relatively rapid warming of the Indian Ocean SSTs, which they contend extends the warm pool and Walker circulation westward, resulting in a subsidence anomaly and drying over East Africa.

To test which mechanism is responsible for the recent drying trend, it is necessary to examine the East African long rains history over a longer time range. If the recent drying is the extension of an earlier long time drying starting from the time when anthropogenic forcing became important, the forced warm pool westward extension mechanism might work. On the other hand, if the recent drying is just a phase of the long rains variability on decadal or longer time scale, then the tropical Pacific control mechanism is more likely to work. Fortunately, there are two datasets that provide an opportunity to investigate the long rains history since as early as 1901: the Global Precipitation Climatology Centre (GPCC,Rudolf et al. (2010)) and Climatic Research Unit at the University of East Anglia (CRU, Mitchell and Jones (2005)) precipitation datasets. Although these two datasets have differing inputs and therefore can potentially yield different results over some regions, they agree very well for the East African long rains. In this thesis, we show that the 9-year-running-averaged long rains have experienced four cycles since the beginning of the twentieth century and the drying trend in recent decades is part of this decadal variability, although the recent trend in GPCC is around two times stronger than the CRU. Furthermore, both linear regression and composite analyses show that the dry phase of the long rains is related to a La Niña-like SST anomaly pattern over the Pacific,

consistent with findings in Lyon and DeWitt (2012). Our results suggest that the drying trend of the East African long rains in recent decades most likely arises from natural decadal variability and is not anthropogenic in origin.

The decline of the long rains also raises the question of how the East African hydroclimate will respond to the warming climate forced by anthropogenic emissions of greenhouse gases (GHGs). Climate model simulations assessed in the Intergovernmental Panel on Climate Change (IPCC) Fourth Assessment Report (AR4) or the more recent Coupled Model Intercomparison Project Phase 5 (CMIP5, Taylor et al. 2012) suggest an expansion of the Hadley circulation (Lu et al., 2007), enhancement of the precipitation-minus-evaparation ($P - E$) pattern (i.e. wet area gets wetter and dry area gets drier) (Held and Soden, 2006; Seager et al., 2010), weakening of the Walker circulation (Vecchi and Soden, 2007), and regional drying trends (Seager et al., 2007; Hoerling et al., 2011; Kelley et al., 2012). Of these changes, the $P - E$ pattern enhancement implies that the East African long rains, which are part of the Intertropical Convergence Zone (ITCZ), will increase. In addition, weakening of the Walker circulation also suggests a wetting trend over East Africa, if the relationship between the East African long rains and the SSTs in Lyon and DeWitt (2012) and Lyon et al. (2013) are correct, where the enhancement of the Walker circulation is reducing the long rains. However, observational studies have shown that the Walker circulation seemed to be strengthening over the twentieth century (Cane et al., 1997; Chen et al., 2002; Compo and Sardeshmukh, 2010; L'Heureux et al., 2013). Further, the multimodel mean of the CMIP5 projections shows a wetting trend over East Africa (Figure 1.1) during both rainy and dry seasons. In contrast, high-resolution regional climate models forced with ensemble-mean of GCM output on the boundaries leads to drier conditions in the future 21st century (Vizy and Cook, 2012a; Cook and Vizy, 2013). These differences could be because of model error representing the forced change or because the observed record is dominated by natural variability. Determining whether the future in East Africa will be drier or wetter requirers a careful examination of the ability of models to simulate realistic natural variability and forced changes.

Paleoclimate studies have shown that East Africa has undergone dramatic hydrocli-

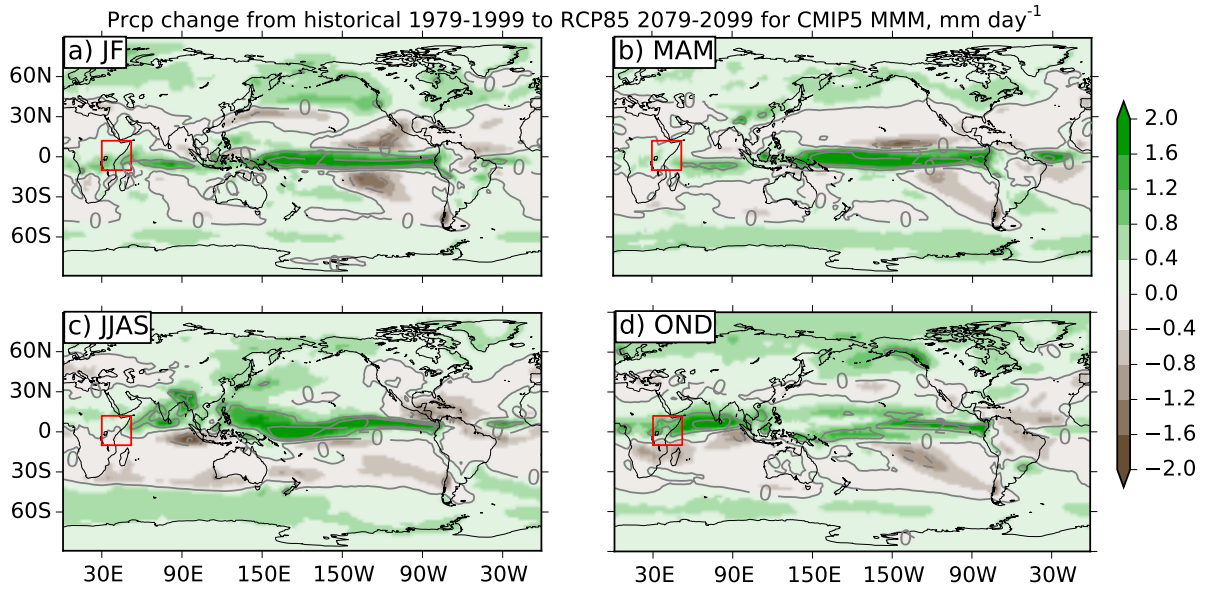

Figure 1.1: Multimodel mean (MMM) precipitation change from 1979–1999 historical runs to 2079–2099 RCP8.5 runs for CMIP5 for season a) JF; b) MAM; c) JJAS and d) OND.

mate variability on multidecadal or longer time scales (Verschuren et al., 2000; Russell and Johnson, 2007) although the temporal resolution in paleoclimate records is not able to distinguish long rains from short rains. By using a Monte Carlo empirical orthogonal function (MCEOF) approach (Anchukaitis and Tierney, 2013) to synthesize different hydroclimatic proxy records, Tierney et al. (2013) not only revealed many features of East African hydroclimate found in previous paleoclimate studies but also identified the spatial patterns of the features and associated uncertainties. In addition, Tierney et al. (2013) concluded on the basis of millennium-long control simulations from different coupled GCMs and proxy records of ocean variability that hydroclimate variability of East Africa on multidecadal timescales is controlled by the Indian Ocean. However, this conclusion depends in part on the capability of these models to simulate aspects of the current climate of East Africa (e.g. climatology and relationship with SSTs), which needs further validation.

In this thesis, we assess the performance of the current GCMs in simulating the pre-

cipitation over East Africa with a series of model simulations, including the International Research Institute for Climate and Society (IRI) forecast models, SST-forced CMIP5 AMIP runs and the CMIP5 historical runs (coupled models). We focus on the simulations of the decadal variability of the long rains as well as the precipitation annual cycle, which is the fundamental aspect of the East African hydroclimate that is supposed to be reproduced by models if the models are considered to be good models. Our results show that the SST-forced ECHAM4.5 and ECHAM5 used for forecasting at the IRI are able to reproduce the precipitation annual cycle over East Africa, decadal variability and its relationship with the pattern of the SST anomalies over the Pacific. Most of the SST-forced models of the CMIP5 AMIP experiment also capture the climatology of the East Africa precipitation as well as the recent observed drying trend of the long rains in the multimodel mean. The multimodel mean of the fully coupled models of the CMIP5 historical experiment, however, underestimates the East African long rains and overestimates the short rains with a considerable range of performance among the individual models. The multimodel mean of the precipitation anomalies shows a weak wetting trend since 1950 that is much smaller than the internal variability. The SST anomaly pattern associated with the dry phase of the East African long rains is associated with a SST gradient over the tropical Pacific, although the magnitude of this is weak compared to observations.

The difficulty for GCMs, especially coupled GCMs, to simulate the annual cycle of East African precipitation raises the question regarding the mechanisms that drive this fundamental aspect of the hydroclimate over this region. Actually, the uniqueness of climate in East Africa has been noticed since at least as early as the 1960s by Trewartha (1961) and the dryness was explained by the divergent and subsident monsoon winds, which are southeasterly in boreal summer and northeasterly in winter. Yet the reasons why the monsoonal flows are divergent and subsident are not clear, but have been generally explained in terms of surface frictional contrast between land and ocean (Bryson and Kuhn, 1961; Nicholson, 1996). However, the wind stress mechanism would be greatest along the immediate coastal areas while observations have demonstrated that the divergence and subsidence are predominant across major areas to the east of the highlands

(Yang et al., 2014a).

Unlike extra-tropical precipitation, which is mainly driven by synoptic scale baroclinic eddies (Lee and Held, 1993; Pierrehumbert and Swanson, 1995; Chang et al., 2002; Yang et al., 2007), tropical rainfall mostly arises from moist convection, in which the subcloud moist static energy (MSE) plays a key role in the framework of quasi-equilibrium (QE, Emanuel et al. (1994)). The QE framework has been applied to study the mechanisms that limit the poleward extent of summer monsoons (Chou and Neelin, 2001, 2003), the location of monsoons (Privé and Plumb, 2007a,b), and the role of orography in monsoons (Boos and Kuang, 2010, 2013; Boos and Hurley, 2013; Ma et al., 2014). An important and relevant idea from these studies is that ventilation (which was defined as the import of low MSE air by advection from cooler oceans) depresses local convection and precipitation by decreasing the subcloud MSE. It should be noted that the ventilation mechanism in these studies is generally applied only in the subtropics because SST is usually cool there but warm over tropical oceans. However, in the case of East Africa, there are strong low-level cross-equatorial monsoonal winds during the dry seasons, especially in summer, which can bring much lower MSE air from the winter hemisphere into East Africa and stabilize the atmosphere. The north-south orientated highlands act to block the import of high MSE air from the west as well as leading to the formation of the East African low-level jet (Findlater, 1969). Indeed, numerical experiments without topography (e.g. Fig. 1a in Chou and Neelin (2003) and Fig. 4a in Boos and Kuang (2010)) demonstrated that East Africa is much wetter during the boreal summer season due to the fact that the low-level jet in observations is weakened (Boos and Kuang, 2010) or even replaced by westerlies in the simulation (Chou and Neelin, 2003). Furthermore, SSTs near the coast are generally cool compared to values further offshore and a west-east SST gradient off the coast exists year-round. Therefore, even in the rainy seasons when the air is imported from the western tropical Indian Ocean by the weak onshore winds, it is still difficult for East Africa to develop high subcloud MSE. Since the saturated MSE above the boundary layer is near uniform across the tropics, and influenced by the warmest of tropical regions, low subcloud MSE in East Africa ensures overwhelming stable conditions

to moist convection.

After the observed annual cycle of East African precipitation has been examined in the new QE framework, the next natural step is to directly analyze mechanisms that cause GCMs' bias in simulating the annual cycle. Previous studies have found various deficiencies of the GCMs that might potentially impact the correct simulation of East African precipitation annual cycle, either due to incorrect response of the atmosphere to prescribed SSTs (Bollasina and Ming, 2013) or due to unrealistic representation of air-sea interactions in the ocean-atmosphere coupled models (Cai and Cowan, 2013; Wang et al., 2014). One pronounced bias found in Yang et al. (2014b) is overestimation of the short rains but underestimation of the long rains in the multimodel mean results. Of all the available CMIP5 models, the MRI-CGCM3 is of particular interest because its AMIP run reproduces the East African precipitation annual cycle very well, while its historical run greatly overestimates the short rains and underestimates the long rains, very similar to the bias for the multimodel mean result. Therefore, MRI-CGCM3 serves as a ideal model to analyze the cause of bias of the CMIP5 models' simulation of the East African precipitation annual cycle.

From a broader point of view, the regional climate over East Africa can be seen as a component of the gigantic Asian monsoon system or even the global monsoon system in the tropics and inevitably interacts with other components within the larger scale system. For example, the onset of the Indian monsoon is usually accompanied by the onset of the East African low level jet and the termination of the East African long rains season. To understand the East African climate, it is helpful to understand the climate in the tropics in general. Since its introduction by Matsuno (1966), the equatorial beta-plane linear model has been serving as a simple dynamical framework for simulating the tropical circulation (Gill, 1980; Davey and Gill, 1987; Seager, 1991). Most of these works assume that the total troposphere can be approximated by the single first baroclinic mode in the vertical such that the shallow water equations can be used to represent the dynamics driven by middle troposphere heating. Lindzen and Nigam (1987) used a different approach that only considers the dynamics of the atmospheric boundary layer

(ABL) driven by the pressure gradients due to the SST gradients but this too yielded a set of shallow water equations with dynamics equivalent to that of the first baroclinic mode method (Neelin, 1989). Later works combined these two ideas to construct a new model structure with an ABL at the bottom plus a first baroclinic mode of the free troposphere above (Wang and Li, 1993; Fu and Wang, 1999).

Despite the success in simulating the general features of the tropical circulation, this type of simple tropical atmospheric circulation model has been challenged because the nonlinear advection terms have been ignored and large Rayleigh friction coefficients have to be applied in order to obtain realistic simulations. Diagnostics of the observational circulation confirmed the suitability of a linear approximation of the surface wind momentum dynamics (Zebiak, 1990; Deser, 1993), although the Rayleigh friction coefficients were demonstrated to be latitudinally dependent and have different magnitudes for zonal and meridional winds (Deser, 1993; Chiang and Zebiak, 2000). Recent studies (Lin et al., 2008) revealed the potential sources of the strong Rayleigh friction over different regions within the Walker circulation: in the deep convection region (the western branch of the Walker circulation), both nonlinear advection and convective momentum transfer (CMT) contribute in the upper troposphere as well as in the lower troposphere; in the shallow convection region (the eastern branch of the Walker circulation), the nonlinear advection contributes in the upper troposphere while the CMT only contributes in the lower troposphere. However, Lin et al. (2008) focused on the zonal momentum balance in the longitude-pressure cross section near the equator instead of the whole tropics and only the annual mean circulation was investigated.

Another issue relevant to the zonal momentum budget is how the equatorial upper troposphere zonal winds are maintained. In their explanation of why the climatological zonal winds are dominated by easterlies in the equatorial upper troposphere, Lee (1999) challenged the idea that the easterlies are maintained by the momentum flux divergence of the midlatitude-generated synoptic eddies (Suarez and Duffy, 1992) and proposed that they are maintained by the transient zonal mean meridional circulation associated with the seasonal cycle of the Hadley circulation and decelerated by tropical transient eddies

with intraseasonal, intraannual and interannual time scales. GCM studies also showed that the easterlies in the equatorial upper troposphere are driven by the cross-equatorial mean meridional circulation while the tropical eddies tend to decelerate them (Kraucunas and Hartmann, 2005). Dima et al. (2005) conducted a systematic investigation on the tropical zonal mean zonal momentum balance based on the NCEP/NCAR reanalysis dataset and confirmed the ideas in Lee (1999) and Kraucunas and Hartmann (2005). However, only the global zonal mean circulations have been examined in these studies and the zonal asymmetry has not been considered. This is important because tropical upper troposphere easterlies are not uniformly distributed in the zonal direction and westerlies can dominate under some conditions (e.g. over the east Pacific during boreal winter). It is interesting to examine if the easterly maintenance mechanism for the global zonal mean flow can be extended to local longitudes and, in contrast, what mechanism is responsible for the maintenance of local westerlies at other longitudes.

The major questions that we address in this thesis include:

1. What causes the recent drying of the long rains over East Africa? What mechanisms are responsible for the dry conditions of the long rains on decadal time scale in the past century?

2. Are GCMs able to reproduce the variability of the East African long rains on decadal time scales (for the SST-forced models) or the observed long rains–SST relationship on this time scale (for the coupled models)?

3. How can we explain the uniqueness of the East African rainfall annual cycle and annual mean climatology?

4. What causes the bias of the rainfall annual cycle over East Africa in the coupled GCMs?

5. What are the key characteristics of the zonal momentum balance in the tropical atmosphere?

This thesis is organized as follows. In Chapter 2, we examine the decadal variability of the East African long rains and assess a series of models in simulating the observed features. We conclude the recent drying trend of the long rains most likely arises from natural decadal variability and is not anthropogenic in origin. While SST-forced GCMs in general can reproduce the observed decadal variability of the long rains as well as the rainfall annual cycle over East Africa, coupled models tend to have a common bias that overestimates (underestimates) the short rains (long rains) climatology, casting doubt on the reliability of the East African hydroclimate projections in CMIP3/5. This work has been published in *Journal of Climate* as Yang et al. (2014b). In Chapter 3, we examine the observed annual cycle of East African precipitation by using the ERA-Interim Re-Analysis data to analyze the seasonal climatologies and annual cycles of the associated atmospheric thermal condition, circulation and moisture budget and propose that the ventilation mechanism, or the import of low moisture static energy air from the off-coast cooler oceans or extratropics, plays an important role in modulating the East African rainfall annual cycle and annual mean climatology. This work has been submitted to *Journal of Climate*. In Chapter 4, we will analyze the coupled model induced bias of the East African rainfall annual cycle by comparing the historical run and AMIP run for each model, with particular emphasis to the model of MRI-CGCM3, which serves as an ideal model representing the miltimodel mean. It is concluded that warm north and cold south SST biases over the Indian Ocean in coupled models are responsible for the dry MAM rainfall bias over East Africa while the ocean dynamics induced warm west and cold east SST biases over the Indian Ocean contribute to the wet OND bias. This work is currently in preparation for publication. In Chapter 5, zonal momentum balance of the tropical atmospheric circulation during the global monsoon mature months (January and July) are analyzed in three dimensions based on the ERA-Interim Re-Analysis. This work has been published in *Journal of the Atmospheric Sciences* as Yang et al. (2013). Finally, in Chapter 6, we conclude with a brief summary of this thesis and discussion on future work.

CHAPTER 2

Decadal Variability of the East African Long Rains in Observations and Models *

2.1 Introduction

East Africa was struck by a severe drought in 2010-2011, the worst drought to occur in the region in the last 60 years, placing millions of people into a humanitarian crisis in this politically and socioeconomically vulnerable region (FEWS NET, 2011; Lyon and DeWitt, 2012). The drought is characterized by failure of two consecutive rainy seasons: the short rains, which is the October–December (OND) rainy season; and the long rains, which is the March–May (MAM) rainy season (Camberlin and Philippon, 2002). While the short rains failure was expected in the La Niña year of 2010 given the robust relationship with El Niño-Southern Oscillation (ENSO) (Ogallo, 1988; Mason and Goddard, 2001), there was difficulty in explaining the long rains failure since no robust forcing of the precipitation in this season, either oceanic or atmospheric, had been identified in past studies (Camberlin and Philippon, 2002).

Lyon and DeWitt (2012) considered the below-normal long rains in 2011 against a longer time scale background. In contrast to Williams and Funk (2011), who have suggested the long rains have been in a multidecadal decline, Lyon and DeWitt (2012) proposed a different explanation. Williams and Funk (2011) associated the drying trend with an anthropogenic-forced relatively rapid warming of Indian Ocean sea surface temperatures (SSTs), which they contend extends the warm pool and Walker circulation westward, resulting in a subsidence anomaly and drying over East Africa. On the contrary, Lyon and DeWitt (2012) linked the decline in the East African long rains with a

* The work of this chapter has been published as: Yang, W., R. Seager, M. A. Cane, and B. Lyon, 2014: The East African long rains in observations and models. *J. Climate*, **27 (19)**, 7185–7202, doi: 10.1175/JCLI-D-13-00447.1.

shift to warmer SSTs over the western tropical Pacific and cooler SSTs over the central and eastern tropical Pacific in 1998–99. Most recently, Lyon et al. (2013) have shown the shift is part of natural multidecadal variability in the Pacific.

Paleoclimate studies have shown that East Africa has undergone dramatic hydroclimate variability on multidecadal or longer time scales (Verschuren et al., 2000; Russell and Johnson, 2007) although the temporal resolution in paleoclimate records is not able to distinguish long rains from short rains. By using a Monte Carlo empirical orthogonal function (MCEOF) approach (Anchukaitis and Tierney, 2013) to synthesize different hydroclimatic proxy records, Tierney et al. (2013) not only revealed many features of East African hydroclimate found in previous paleoclimate studies but also identified the spatial patterns of the features and associated uncertainties. In addition, Tierney et al. (2013) concluded on the basis of millennium-long control simulations from different atmosphere-ocean general circulation models (AOGCMs) and proxy records of ocean variability that hydroclimate variability of East Africa on multidecadal timescales is controlled by the Indian Ocean. However, this conclusion depends in part on the capability of these models to simulate aspects of the current climate of East Africa (e.g. climatology and relationship with SSTs), which needs further validation.

A highly relevant issue is how the East African long rains will respond to the warming climate forced by anthropogenic emissions of greenhouse gases (GHGs). Climate model simulations assessed in the Intergovernmental Panel on Climate Change (IPCC) Fourth Assessment Report (AR4) or the more recent Coupled Model Intercomparison Project Phase 5 (CMIP5, Taylor et al. 2012) suggest an expansion of the Hadley circulation (Lu et al., 2007), enhancement of the precipitation-minus-evaparation ($P - E$) pattern (i.e. wet area gets wetter and dry area gets drier) (Held and Soden, 2006; Seager et al., 2010), weakening of the Walker circulation (Vecchi and Soden, 2007), and regional drying trends (Seager et al., 2007; Hoerling et al., 2011; Kelley et al., 2012). Of these changes, the $P - E$ pattern enhancement implies that the East African long rains, which are part of the Intertropical Convergence Zone (ITCZ), will increase. In addition, weakening of the Walker circulation also suggests a wetting trend over East Africa, if the relationship

between the East African long rains and the SSTs in Lyon and DeWitt (2012) and Lyon et al. (2013) are correct. However, observational studies have shown that the Walker circulation seemed to be strengthening over the twentieth century (Cane et al., 1997; Chen et al., 2002; Compo and Sardeshmukh, 2010; L'Heureux et al., 2013). Further, the multimodel mean of the CMIP5 medium mitigation scenario (RCP4.5) projections shows a wetting trend over East Africa (Fig. 2.1a) during the long rains season over the first half of the twenty-first century while high-resolution regional climate models forced with ensemble-mean GCM output on the boundaries leads to drier 21st century long rains (Vizy and Cook, 2012a; Cook and Vizy, 2013), which is probably consistent to the observed drying trend over the past three decades (Fig. 2.1b and Fig. 2.2a). These differences could be because of model error representing the forced change or because the observed record is dominated by natural variability. Determining whether the future in East Africa will be drier or wetter requires a careful examination of the ability of models to simulate realistic natural variability and forced changes.

In this study, we will investigate the decadal variability of the East African long rains and its relationship with SSTs in observations and compare them with a series of model simulations, including the International Research Institute for Climate and Society (IRI) forecast models, SST-forced CMIP5 experiments (so called Atmosphere Model Intercomparison Project, AMIP) and the CMIP5 historical simulations (coupled models). The key questions include: what is the character of decadal variability of the East African long rains in the observations over the past century? What is its relationship with the observed SSTs? Do the simulations from the SST-forced models and the fully coupled models capture the these features? What does that imply for the model projections of the East African long rains precipitation in the near future? The chapter is organized as follows: data and methods are described in Section 2.2; Section 2.3 presents the observational results; Section 2.4 describes SST-froced model (IRI forecast models and CMIP5 AMIP experiment models) simulations and comparison with the observations; results from CMIP5 historical experiments are presented in Section 2.5 conclusions and a discussion are presented in Section 2.6.

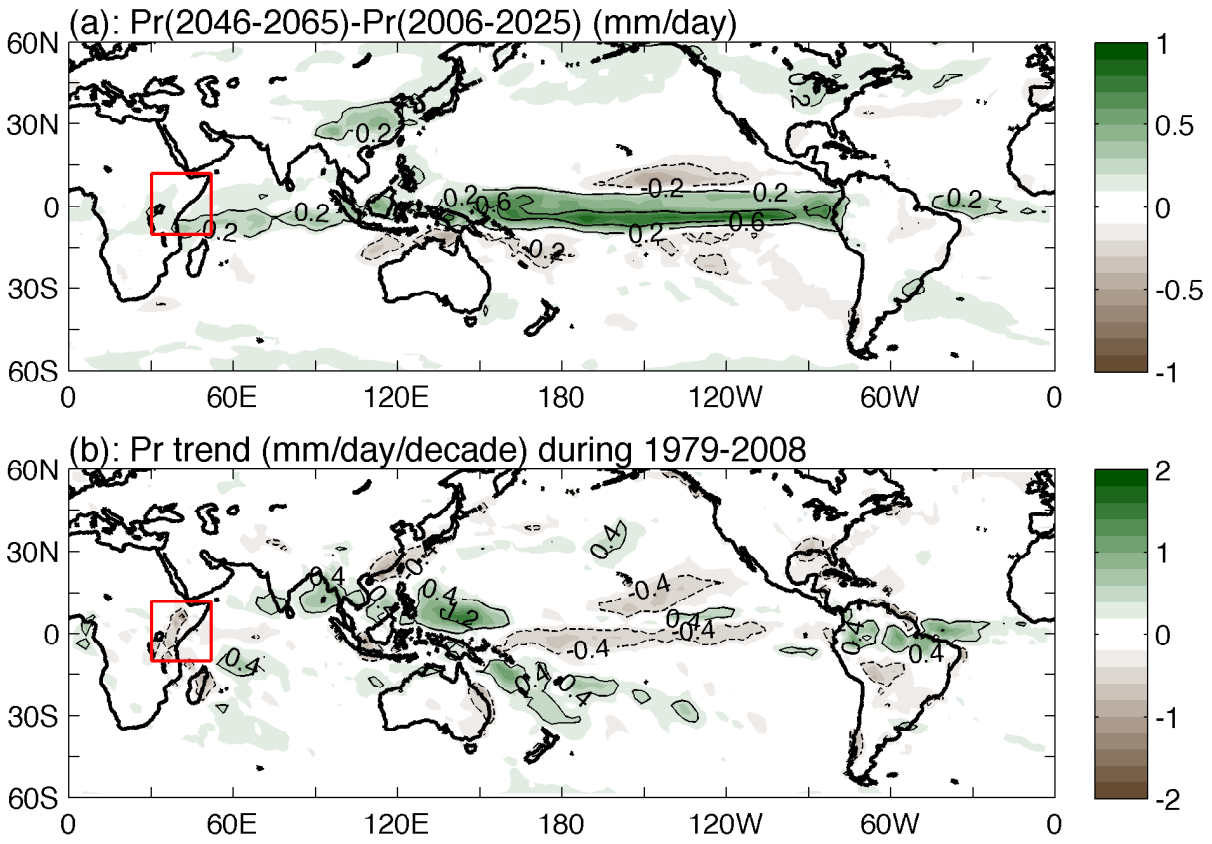

Figure 2.1: (a): MAM precipitation rate difference between 2046–2065 and 2006–2025 from CMIP5 RCP4.5 projection multimodel mean. (b): MAM precipitation rate linear trend over the period of 1979–2008 from GPCP dataset. Red boxes in the two panels denote the East Africa area between 30^0E and 52^0E and 10^0S and 12^0N.

2.2 Data and methods

For precipitation, we use the following datasets: version 5 of Global Precipitation Climatology Centre (GPCC) monthly precipitation (Rudolf et al., 2010), which is a gauge-based, gridded global land surface dataset for the period from 1901 to the near present; version TS 3.1 of monthly precipitation over global land areas from Climatic Research Unit at the University of East Anglia (CRU hereafter, Mitchell and Jones 2005); version 2.2 of the Global Precipitation Climatology Project (GPCP) monthly precipitation dataset from 1979 to 2012 (Huffman et al., 2009), which combines gauge observations and satellite

data into $2.5^0 \times 2.5^0$ global grids; Climate Prediction Center (CPC) Merged Analysis of Precipitation (CMAP) (Xie and Arkin, 1997), which is also monthly satellite and gauge data and covering from 1979 to the present.

The observational sea surface temperature (SST) is from the version 3b of the NOAA National Climate Data Center (NCDC) Extended Reconstructed Sea Surface Temperature (ERSST) (Smith et al., 2008), which is a globally gridded monthly dataset with a spatial resolution of 2^0 by 2^0 and covers the period from 1854 to the present.

Historical simulations (from 1950 to the present) from three different International Research Institute for Climate and Society (IRI) forecast models forced only with observed SST (`http://iridl.ldeo.columbia.edu/SOURCES/.IRI/.FD/`) include: ECHAM4.5 (Roeckner et al., 1996), ECHAM5 (Roeckner et al., 2006) and CCM3.6 (Kiehl et al., 1996). Each model has twenty-four ensemble members initialized with different atmospheric conditions. Both the ensemble mean and its range (represented as the 5th and 95th percentiles) are estimated for the climatology and historical time series but only the ensemble mean is used to examine the relationship between East African precipitation and SSTs.

The SST-forced models used in this study also include twelve models from the CMIP5 AMIP experiment (Table 2.1). Each model has at least one ensemble member and some have as many as ten (e.g. CSIRO-Mk3-6-0). For each model, we only analyze the period between 1979 to 2008 which is the longest period shared by the twelve models. We also use the fully coupled models from the CMIP5 historical experiment (Table 2.2), of which there are forty three in total and the period of 1850–2005 common for almost all of the models is used in the multimodel mean estimation. Note that the analysis of observations and the SST-forced models uses observed SSTs while the coupled models generate their own natural variability of SSTs and climate which is not expected to be synchronous with natural variability in nature.

Table 2.1: Models of the CMIP5 AMIP experiment used in our analysis.

Index	Name	Time Span	Ensemble #
1	CanAM4	1950-2009	4
2	CNRM-CM5	1979-2008	1
3	CSIRO-Mk3-6-0	1979-2009	10
4	GFDL-HIRAM-C180	1979-2008	3
5	GFDL-HIRAM-C360	1979-2008	2
6	GISS-E2-R	1880-2010	1
7	HadGEM2-A	1979-2008	1
8	inmcm4	1979-2008	1
9	IPSL-CM5A-LR	1979-2009	5
10	MPI-ESM-LR	1979-2008	3
11	MRI-AGCM3-2H	1979-2008	1
12	NorESM1-M	1979-2008	3

Table 2.2: Models of the CMIP5 historical experiment used in our analysis.

Index	Name	Time Span	Ensemble #
1	ACCESS1-0	1850-2005	1
2	ACCESS1-3	1850-2005	1
3	bcc-csm1-1	1850-2012	3
4	bcc-csm1-1-m	1850-2012	3
5	BNU-ESM	1850-2005	1
6	CanCM4	1961-2005	10
7	CanESM2	1850-2005	5
8	CCSM4	1850-2005	6
9	CESM1-BGC	1850-2005	1
10	CESM1-CAM5	1850-2005	3
11	CESM1-CAM5-1-FV2	1850-2005	4
12	CESM1-FASTCHEM	1850-2005	3
13	CESM1-WACCM	1955-2005	4
14	CMCC-CESM	1850-2005	1
15	CMCC-CM	1850-2005	1
16	CMCC-CMS	1850-2005	1
17	CNRM-CM5	1850-2005	10
18	CSIRO-Mk3-6-0	1850-2005	10
19	FGOALS-g2	1900-2005	5
20	FGOALS-s2	1850-2005	3
21	FIO-ESM	1850-2005	3
22	GFDL-CM3	1860-2005	5
23	GFDL-ESM2G	1861-2005	3
24	GFDL-ESM2M	1861-2005	1

Continued on Next Page...

Table 2.2 – Continued

Index	Name	Time Span	Ensemble #
25	GISS-E2-H	1850-2005	5
26	GISS-E2-R	1850-2005	6
27	HadCM3	1860-2005	10
28	HadGEM2-CC	1960-2004	3
29	HadGEM2-ES	1860-2004	4
30	inmcm4	1850-2005	1
31	IPSL-CM5A-LR	1850-2005	5
32	IPSL-CM5A-MR	1850-2005	1
33	IPSL-CM5B-LR	1850-2005	1
34	MIROC-ESM	1850-2005	3
35	MIROC-ESM-CHEM	1850-2005	1
36	MIROC4h	1950-2005	3
37	MIROC5	1850-2005	4
38	MPI-ESM-LR	1850-2005	3
39	MPI-ESM-MR	1850-2005	3
40	MPI-ESM-P	1850-2005	2
41	MRI-CGCM3	1850-2005	3
42	NorESM1-M	1850-2005	3
43	NorESM1-ME	1850-2005	1

In this study, the region of East Africa is represented by the land area between 30^0E and 52^0E and 10^0S and 12^0N (red box in Fig. 2.1). In order to reveal the SST anomaly pattern associated with the decadal variability the East African long rains, three types of analysis have been applied: Empirical Orthogonal Function (EOF) analysis (Wilks, 2011), linear regression analysis (regression of SST at each grid point on the time series of the East African long rains anomalies) and composite analysis (composite of SST anomalies

over years when the East African long rains anomalies are one standard deviation below from the mean). In all the analyses, a nine-year running average is applied to both the precipitation and SST datasets before performing the analysis.

2.3 Observational analysis

Fig. 2.2a shows the nine-year-running-averaged anomalies (relative to the 1979-2000 base) of the East African long rains in four observational datasets: GPCC, GPCP, CMAP and CRU. The four datasets are consistent in showing drying over the most recent decades when all have data. The GPCC anomalies have a slightly smaller magnitude than the two satellite-gauge datasets GPCP and CMAP and the magnitude of the CRU drying is only about half that of GPCC. The estimated linear trends from 1983 on are -0.19 mm day^{-1} decade^{-1} in GPCC, -0.33 mm day^{-1} decade^{-1} in GPCP, -0.35 mm day^{-1} decade^{-1} in CMAP and -0.08 mm day^{-1} decade^{-1} in CRU. All of these trends are statistically significant at the 0.05 level. Estimation of the precipitation anomalies based on the multi-satellite product (pure satellite product) from GPCP shows little difference from the satellite-gauge result, indicating that the recent drying trend is not driven by the loss of gauge coverage. The longer GPCC and CRU datasets suggest that the drying trend in the most recent decades is part of the decadal variability of climate over East Africa. There are at least four wet-dry cycles in the GPCC precipitation data for East Africa. The first one started around the beginning of the data period and ended around 1930. The second one extended from about 1930 to the beginning of 1960s. The third one is relatively short, from the end of the second cycle to the middle of 1970s. The last one started from the end of the third cycle to the present day and probably continues. The CRU data is generally consistent with the GPCC over the whole period and shows similar decadal variability as in GPCC.

Besides the decadal variability described above, there is also a small centennial-scale drying trend of -0.019 mm day^{-1} decade^{-1} (or -0.19 mm day^{-1} century^{-1} in GPCC, similar to the time series over the same period in Figure 1b from Tierney et al. (2013). It is unclear whether this trend is part of natural variability on longer time scales as

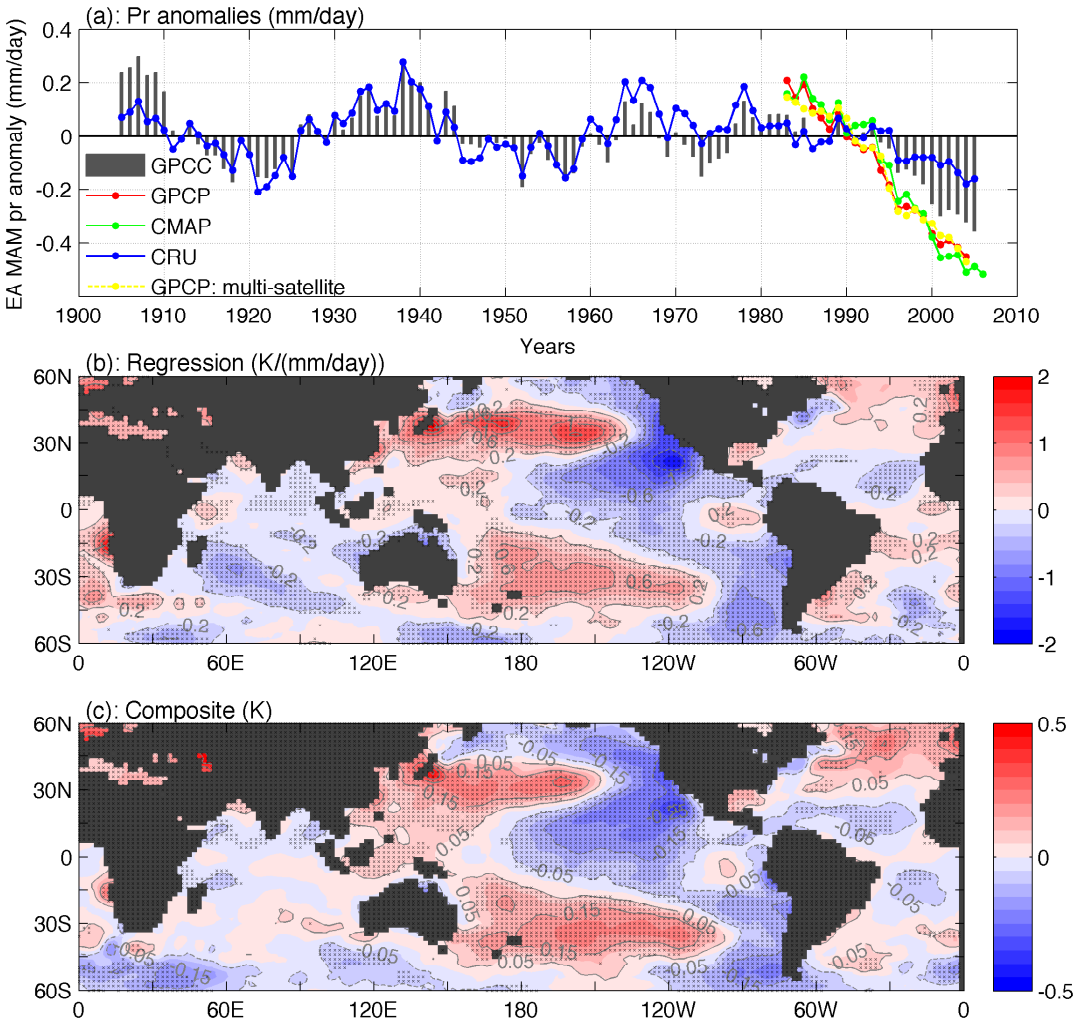

Figure 2.2: (a): East Africa (30^0E–52^0E, 10^0S-12^0N) MAM precipitation rate anomaly relative to the 1979–2000 base period in observations. Nine-year running average has been applied to all the time series (though the 1979–2000 base is chosen and estimated based on the non-running-averaged time series). (b): Regression of SST anomaly on the negative of East Arica precipitation rate anomaly (i.e. b as in $sst_a = -b \times pr_a$) in MAM over the period of 1901–2009. (c): Composite of MAM SST anomaly from years when East Africa MAM precipitation anomaly is one standard deviation below the mean. In both (b) and (c), The global average SST has been removed from the SST data by linear regression and a nine-year running average has been applied to both the SST and the precipitation. The SST and precipitation data are from ERSST and GPCC respectively. Cross markers indicate being statistically significant at the 0.05 level.

in Tierney et al. (2013) or an indication of a global warming signal as in Williams and Funk (2011) or even associated with data issues (e.g. quality of data, the number of rain gauges used per grid point and the way data have been interpolated) since the trend is much weaker in the CRU dataset (only -0.041 mm day^{-1} century^{-1}). However, if we assume the trend is due to global warming, as represented by either global mean SST or CO_2 concentration, and there is a linear relationship between the warming and the corresponding response in East Africa MAM precipitation, we can estimate the relative importance of natural and forced variability in East Africa MAM precipitation on decadal to centennial time scales. Fig. 2.3a shows the nine-year-running-averaged East Africa MAM precipitation in GPCC before and after removing the postulated global warming component, as represented by global mean SST anomalies from ERSST. Removing the presumed global warming component decreases the magnitudes of wet anomalies at the beginning of the period and the dry anomalies over the last decade but does not change much the precipitation time series. The whole time series and the drying trend in recent decades are still dominated by natural variabilities. Using CO_2 instead of global mean SST to represent the global warming forcing shows similar results (Fig. 2.3c). Since there is little drying trend on the centennial scale in the CRU dataset, the global warming component revealed by the linear regression method is much weaker than that of GPCC and the dominance of natural variability is even stronger (Fig. 2.3b and 2.3d).

Lyon et al. (2013) associated the recent East African long rains drought with maps of global MAM precipitation and SST anomalies and attributed the recent increase in drought frequency to multidecadal variability of SSTs in the tropical Pacific, with cooling in the east and warming in the west. Can similar SST anomaly patterns be found in historical intervals when East African long rains are also in dry phases? Fig. 2.4 shows the maps of MAM precipitation anomalies over land and SST anomalies in the four periods when East African long rains are dry. Even though each dry period has its own features, it seems the SST anomaly patterns over the Pacific Ocean are generally consistent over the four periods. Warm SST anomalies appear in the northern, northwestern and southern Pacific while cool SST anomalies appear over the the central to eastern Pacific. A small

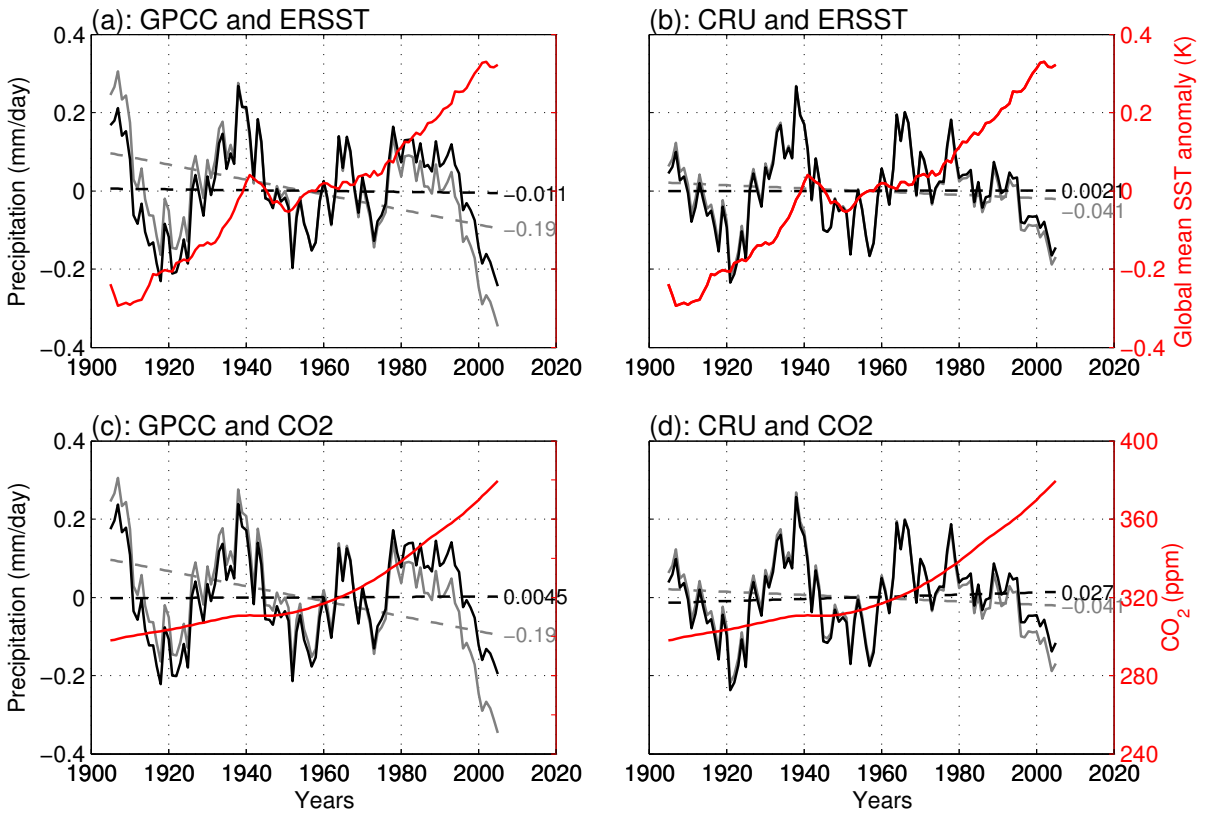

Figure 2.3: East Africa MAM precipitation anomalies (gray lines) and their residuals (black lines) after removing the global warming signals (red lines). Dashed lines are the corresponding linear trends (mm day^{-1} century^{-1}). (a) and (c) use the GPCC dataset while (b) and (d) use the CRU precipitation dataset. Global mean of MAM ERSST is used as the global warming signal in (a) and (b) while annual mean CO_2 concentration is used in (c) and (d). All time series have been low-pass filtered by applying a nine-year running average.

inconsistency is found over the central tropical Pacific during the period of 1945-1963 (Fig. 2.4b) where warm SST anomalies appear. However, the SST anomalies over the eastern Pacific are still negative. Over other oceans, however, SST anomaly patterns are in general inconsistent. For example, the tropical Indian Ocean has warm SST anomalies during the periods of 1914-1925 (Fig. 2.4a) and 1994-2005 (Fig. 2.4d) but cool anomalies during the periods of 1945-1963 (Fig. 2.4b) and 1968-1976 (Fig. 2.4c). Over the Atlantic Ocean, the periods of 1914-1925 (Fig. 2.4a) and 1968-1976 (Fig. 2.4c) have a pattern of cooling in the north but warming in the south while opposite patterns are found during the other two periods. Fig. 2.5 shows the composite from the sign functions of the four SST anomaly maps in Fig. 2.4. Large positive or negative values appear over vast areas of the Pacific Ocean but not the Indian Ocean or the Atlantic Ocean, consistent with the previous analysis. Therefore, decadal variations in the East African long rains appear to be controlled by SST over the Pacific, consistent with the numerical experiment results in Lyon and DeWitt (2012) and Lyon et al. (2013), even though some studies suggest that Pacific, Indian and Atlantic Oceans all contribute to the decadal variability of the East African long rains (Omondi et al., 2013). The SST patterns over the Pacific are similar to those found in the studies of Pacific interdecadal climate variability such as Deser et al. (2004), although they focused on the boreal winter season. Along with the SST anomaly patterns over the Pacific, there are also consistent precipitation anomaly patterns around the global land areas (as noted by Herweijer and Seager 2008), including wet anomalies in the southern Africa, dry anomalies in the western North America and the wet-dry-wet pattern from the north to the south in South America. These consistent precipitation anomalies indicate that they might also be attributed to the same SST anomaly pattern in the Pacific as in the East African long rains case.

To obtain a more general relationship between the East African long rains and the global SST pattern, Fig. 2.2b shows the map of regression of SST anomaly on the negative of the East African precipitation anomaly during the long rains. The global average has been removed from the SST by regression and a nine-year running average applied to both the SST and the precipitation data. The regression coefficients show a La Niña-like

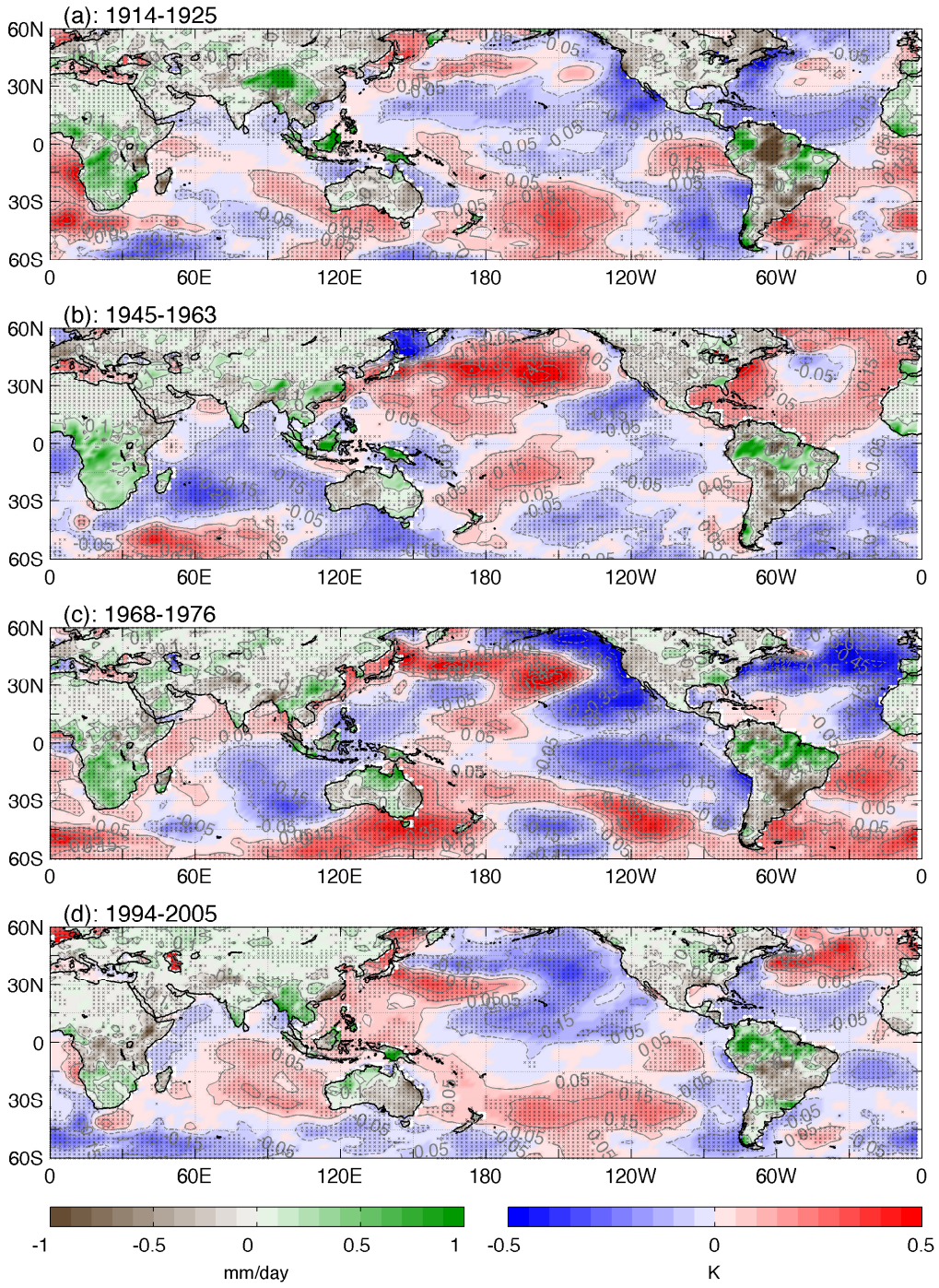

Figure 2.4: Composite of MAM GPCC precipitation rate anomalies over land (brown-green colors) and MAM ERSST anomalies (blue-red colors). Global mean has been removed from the SST by linear regression and a nine-year running average has been applied to both the SST and precipitation datasets before performing the composite analysis. Cross markers indicate being statistically significant at the 0.05 level.

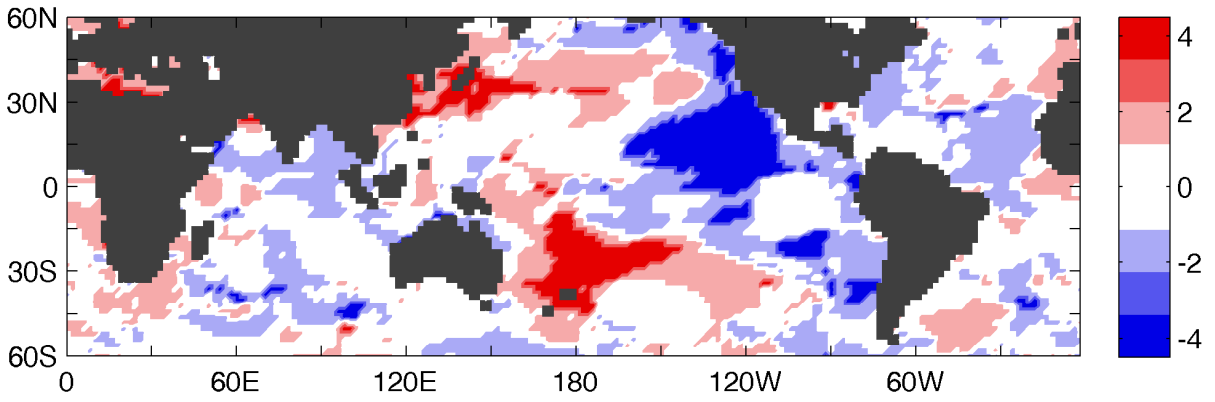

Figure 2.5: Composite from the sign functions of the four SST anomaly maps in Fig. 2.4, i.e. set the values on each grid to be 1/0/-1 if the SST anomaly on the grid is greater than/equal to/less than zero and add the four sign maps up. Large positive or negative values indicate strong consistence across the four maps of SST anomalies in Fig. 2.4.

spatial pattern, with negative values over the central and eastern tropical Pacific and positive values over the western tropical Pacific. Positive values are also found in the northern Pacific (around 40^0N) and southern Pacific (around 30^0S). These features are consistent with the composite results from different dry periods in Fig. 2.4. Choosing the years when the East African long rains anomalies are one standard deviation below from the mean during the whole period and making a composite map of the SST anomalies for these years again shows a similar pattern, confirming the robustness of the SST pattern (Fig. 2.2c). The SST anomaly composite in Fig. 2.2c also shows large values over the northern Atlantic but it does not mean it is associated with the East African long rains, as discussed in the previous paragraph.

Can we find a mode directly from the SST data that has a similar spatial pattern to that shown above and at the same time correlates with the East African long rains? Fig. 2.6 shows the first EOF of the MAM SST after removing the global-averaged value so as to focus on natural variability. A nine-year running average has also been applied to emphasize the decadal variability. The first EOF explains 22% of the total variance and shows a La Niña-like spatial pattern, with negative values over the central and eastern tropical Pacific and positive values over the western tropical Pacific. Positive values

also appear over the northern Pacific (centered around 40^0N) and the southern Pacific (centered around 30^0S). This pattern is very similar to that derived by regressing or compositing based on the precipitation data. The first principal component (PC1, time series from the EOF analysis) shows decadal variability with positive and negative anomalies lasting from years to decades. PC1 is closely correlated with the East African long rains anomaly (correlation coefficient of -0.62). During the recent drying phase and that in the 1970s, PC1 had positive values. In contrast, during the wet phases in the 1980s, 1930s and 1900s, PC1 had negative values. Therefore, the decadal variability of the East African long rains has a clear association with decadal SST variation over the Pacific, which is consistent with Lyon et al. (2013) but based on an analysis going further back in time.

2.4 SST-forced models

We begin by showing the East African precipitation climatology for the SST-forced ECHAM4.5 simulations and the GPCC observations in Fig. 2.7. Unlike typical monsoon regions such as the Asian monsoon region where there is only one rainy season within a year and the rainy season appears in the summer months (Yang et al., 2013), there are primarily two rainy seasons across much of East Africa: the long rains (MAM) and the short rains (OND). In some areas there is a relative maximum in July and August since our East Africa region covers some area to the northwest where typical monsoon features emerge. The model simulations in general overestimate the precipitation climatology in every month but the overestimation is least in our months of interest, i.e. March, April and May (the long rains). The belt specified by the 5th and 95th percentiles of the 24 ensemble members is generally narrow, indicating that the simulated climatology does not differ much across the ensemble members. This gives us some confidence with regard to the capability of the model to simulate East African precipitation.

Fig. 2.8a then shows the East African long rains anomaly in the ECHAM4.5 model simulations. Comparing with the GPCC data, the ensemble mean time series captures the drying trend since 1990. The ensemble mean also captures the wetting trend from

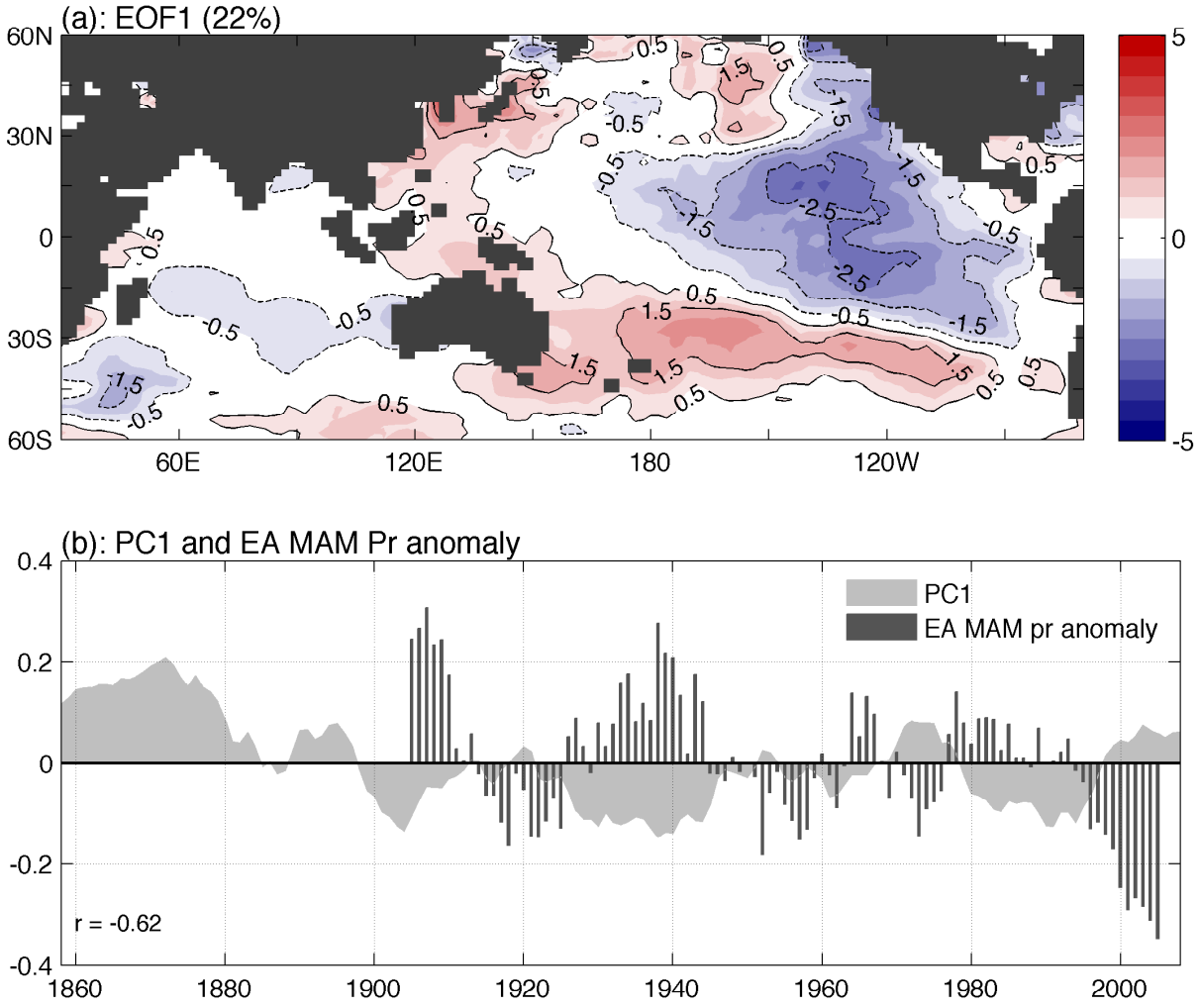

Figure 2.6: The first EOF of the ERSST in MAM over domains of 30E-70W and 60S-60N after removing the global mean SST and performing a 9-year running average. (a): The first EOF spatial pattern. (b): The first principal component (time series from the EOF analysis, lighter gray area plot, unit K) and East Africa MAM precipitation anomaly from GPCC (gray bars, unit mm day^{-1}).

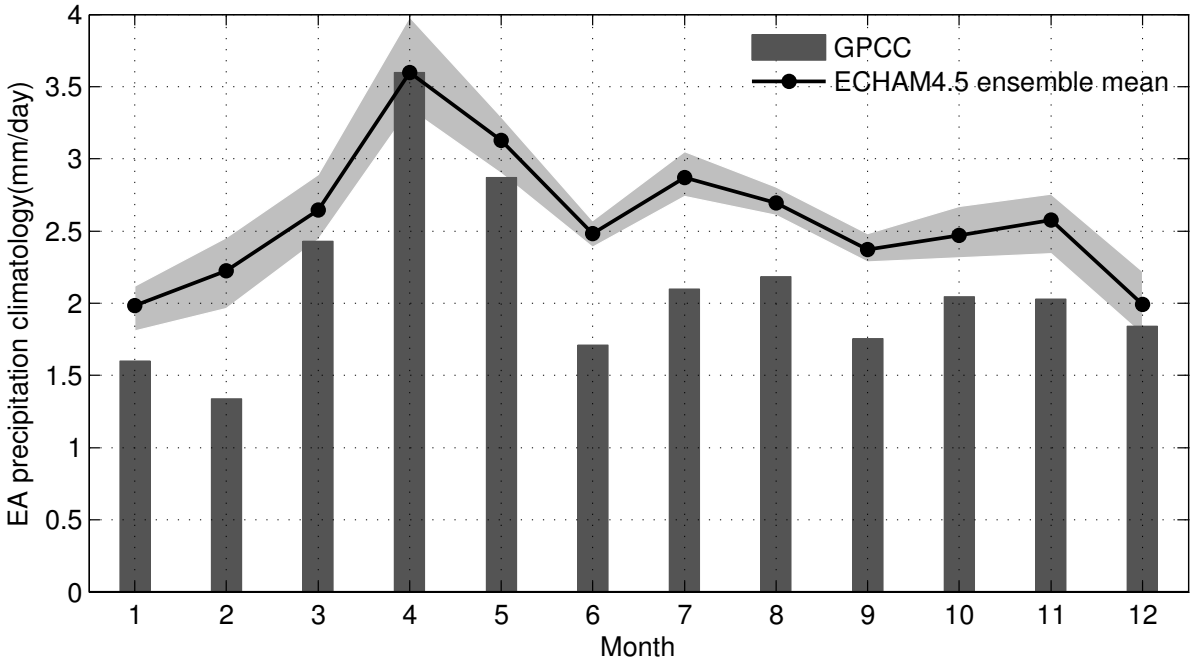

Figure 2.7: East Africa (30^0E-52^0E, 10^0S-12^0N) precipitation rate climatology in GPCC and ECHAM4.5 model simulations estimated over the period of 1979–2005. The gray area indicates the range between the 95th and the 5th percentiles of the 24 ensemble members.

middle 1950s to the late 1960s, but does not simulate the dry anomalies in the 1950s. An even larger discrepancy appears in the 1970s and 1980s when there seems little relation between modeled and observed precipitation. The width of the belt between the 5th and 95th percentiles exceeds the standard deviation of the ensemble mean time series, indicating that the modeled East African long rains are strongly influenced by internal variability in addition to the SST forced component.

To determine the SST pattern associated with East African long rains variability, Fig. 2.8b shows the regression of ERSST on the ECHAM4.5 ensemble mean East African long rains precipitation. Comparing with the observed pattern (Fig. 2.2b), we see that the modeled regression pattern captures major large scale observed features over the Pacific, although the modeled regression values over the northern Atlantic are much larger than the observed. For example, positive SST values appear in the western tropical Pacific while negative values lie in the central and eastern tropical Pacific. Similarly, there are also positive bands in the southern Pacific centered around 30^0S and in the northern Pacific centered around 40^0N. The composite SST anomaly map over the East African region during anomalously dry long rains years (Fig. 2.8c) also resembles the ECHAM4.5 model captures the main features of the East African long rains-SST relationship.

We also did this analysis for the two other IRI forecast models, ECHAM5 and CCM3.6 (not shown). ECHAM5 underestimates the long rains precipitation climatology but resembles ECHAM4.5 in many of the features described above. CCM3.6 has the worst performance among the three models as it not only overestimates the long rains precipitation climatology but also has a wetting trend after 1996, which is opposite to the observed trend.

Fig. 2.9 shows the East African precipitation climatology in the SST-forced CMIP5 AMIP experiments along with the observed values from GPCC. The multimoldel ensemble mean agrees quite well with the GPCC climatology. The maximum model precipitation correctly appears in the long rain season, i.e. March, April and May. Compared with Fig. 2.7, the major difference is the broad spread among ensemble members. The width between the 5th and 95th percentiles in the CMIP5 AMIP ensemble is much larger than for

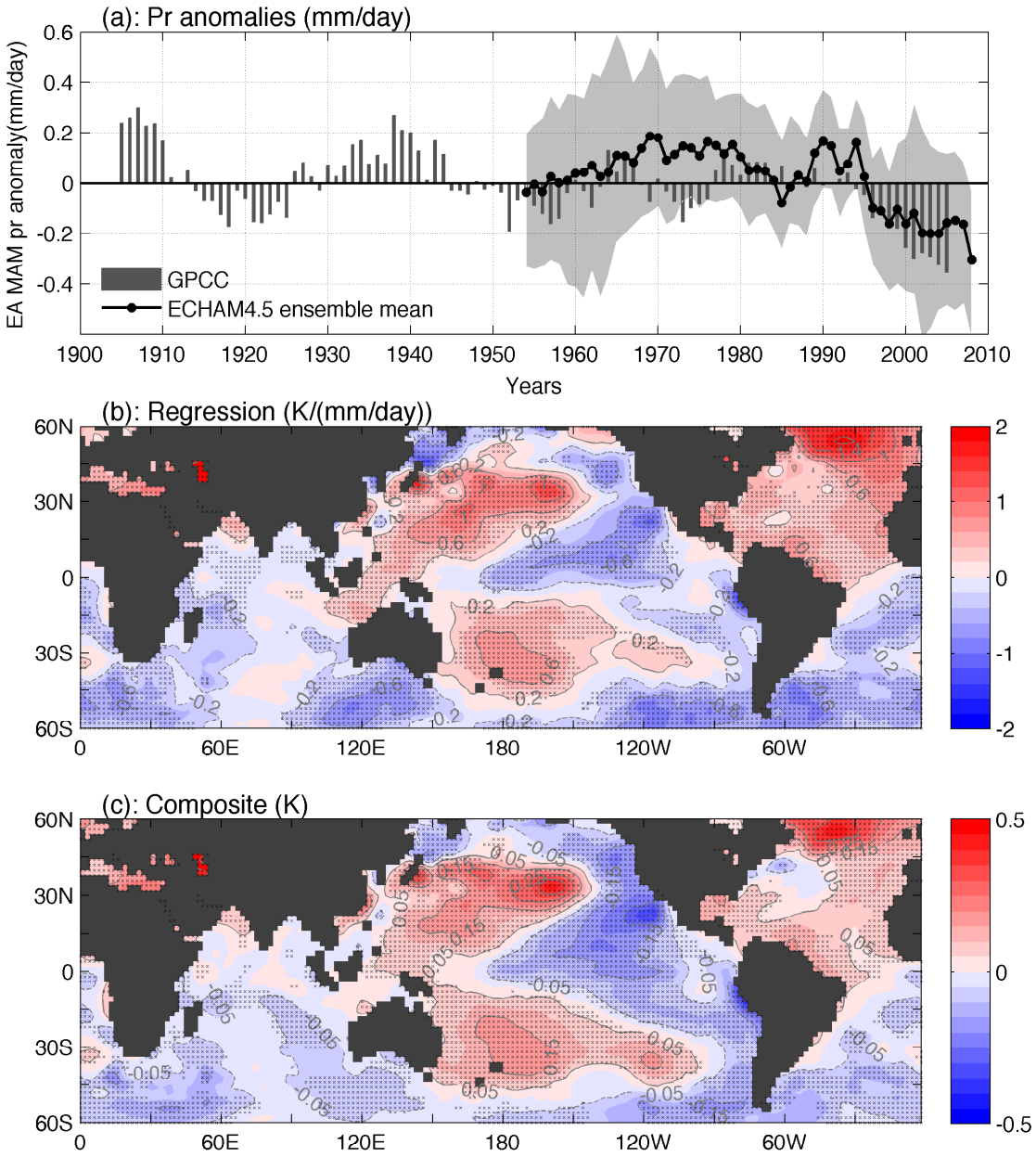

Figure 2.8: Same as Fig. 2.2 but for ECHAM4.5 instead of observations. The gray area in (a) indicates the range between the 95th and the 5th percentiles of the 24 ensemble members. The ensemble mean time series in (a) is used in (b) and (c).

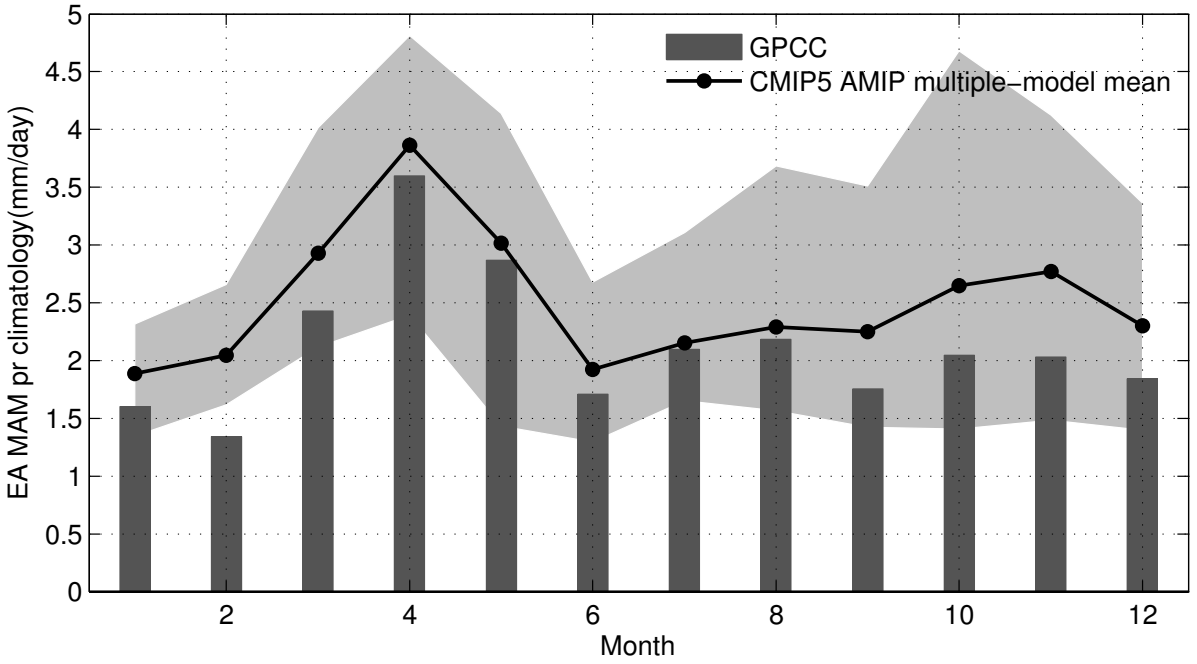

Figure 2.9: Same as Fig. 2.7 but for CMIP5 AMIP multimodel runs instead of ECHAM4.5.

the ECHAM4.5 ensemble, indicating greater internal variability introduced by differences among models.

As most models in the CMIP5 AMIP experiment only cover the period from 1979 to the present day, it is difficult to examine the decadal variability in these simulations. However, we can assess whether the simulations produce the behavior since 1979. Fig. 2.10a shows the time history of the East African long rains anomaly in the CMIP5 AMIP experiment models. The ensemble mean shows an overall drying trend, especially after 1990. The magnitude of the drying trend, however, is smaller than for GPCC and occurs amidst a large spread among the ensemble members.

Both the regression of SST anomaly on the East African long rains anomaly (Fig. 2.10b) and the East African dry MAM years composite of SST anomalies (Fig. 2.10c) show La Niña-like patterns, similar to the results in the observations and the IRI forecast models. This indicates that the ensemble mean of the CMIP5 AMIP experiment simulations is capable of capturing the relationship between the East African long rains and

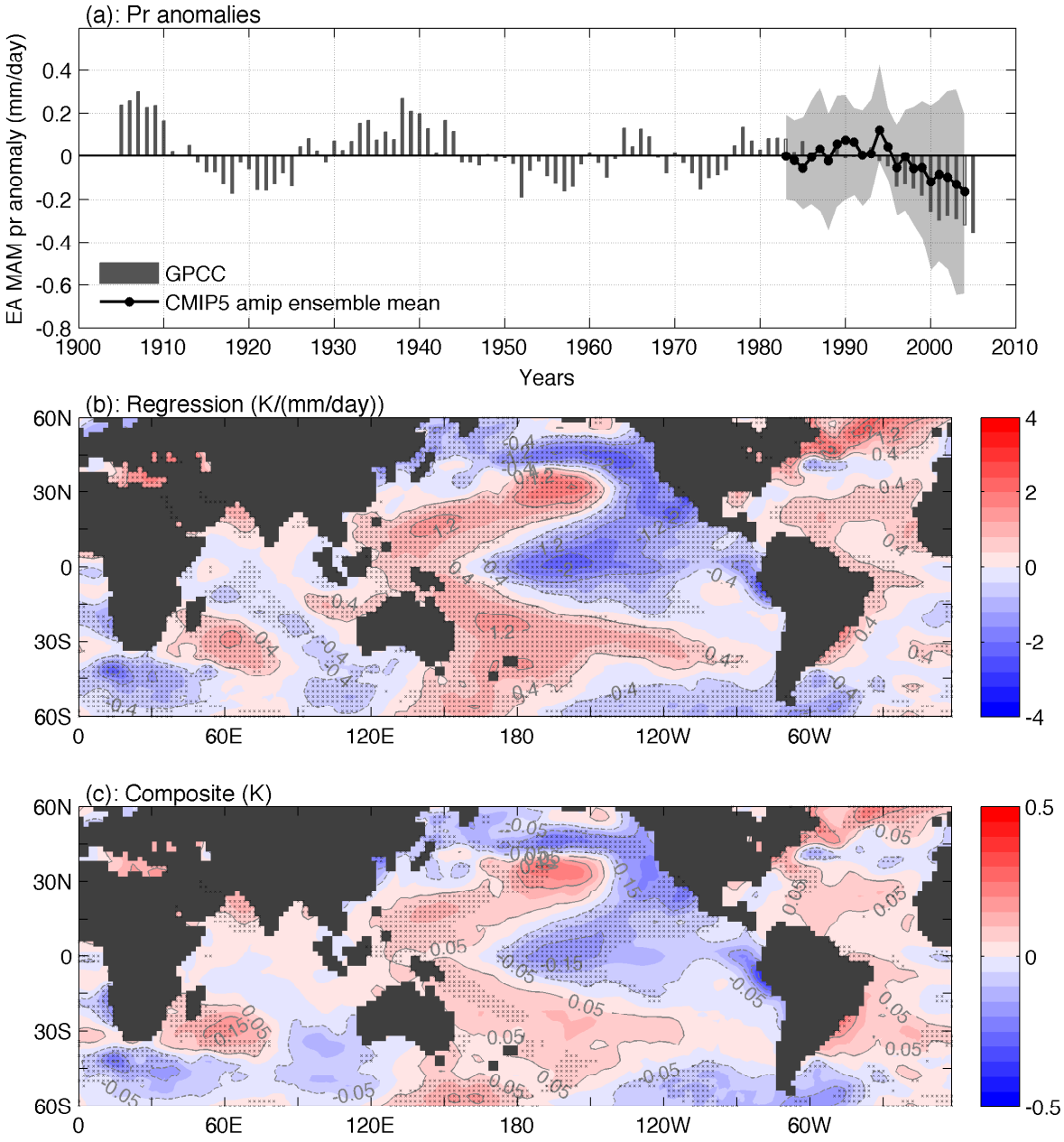

Figure 2.10: Same as Fig. 2.8 but for CMIP5 AMIP multimodel runs instead of ECHAM4.5.

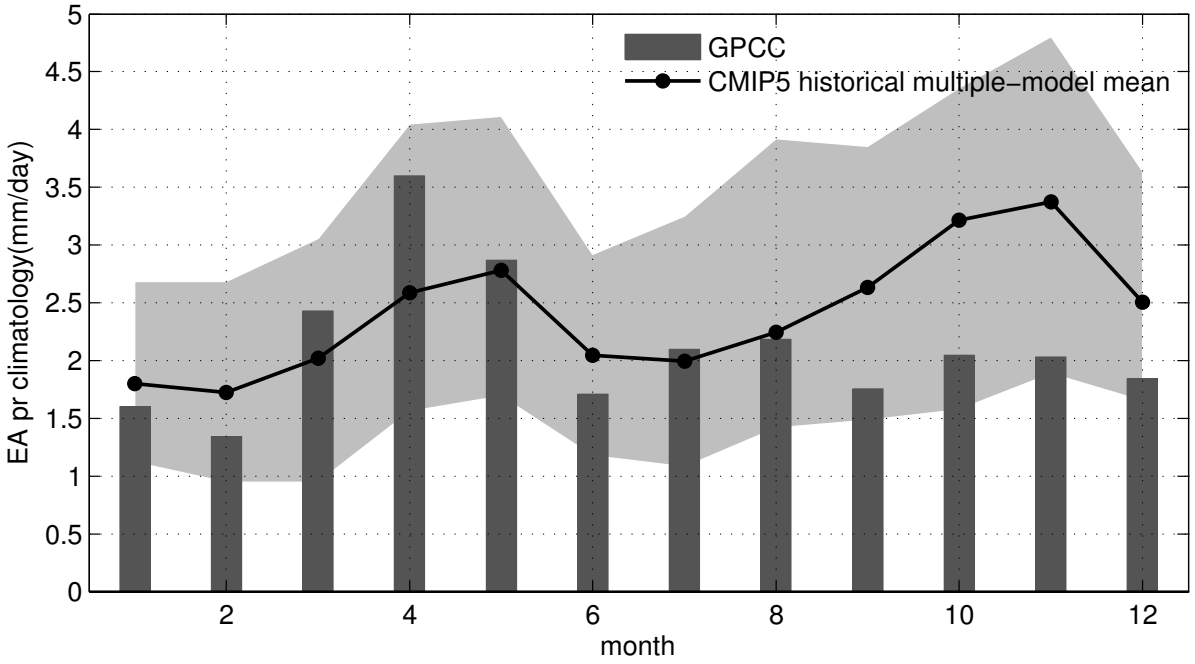

Figure 2.11: Same as Fig. 2.7 but for CMIP5 historical multimodel runs instead of ECHAM4.5.

the SST anomaly pattern, although capability is limited only to recent decades.

2.5 CMIP5 historical experiment

Fig. 2.11 shows the East African precipitation climatology in the coupled CMIP5 historical experiments. The multimodel mean climatology does not agree with the observations; it is clearly worse than the SST-forced IRI forecast models and CMIP5 AMIP simulations. It underestimates the long rains (March, April and May) and overestimates the short rains (October, November, December). The long rains peak during May instead of April as in the observations. The spread is quite large. All of these problems have also been reported in CMIP3 models (Anyah and Qiu, 2012). The drop in realism of the precipitation simulation relative to the SST-forced atmosphere models arises in errors introduced by the simulation of SSTs.

The multimodel mean among coupled models cancels out most of the internal variabilities, whether generated by internal atmospheric or coupled atmosphere-ocean variability,

and isolates the externally forced change. The CMIP5 historical multimodel mean does not capture the time series of the East African long rains anomaly (Fig. 2.12a) showing only a weak wetting trend after 1950. This forced wetting trend is consistent with the 21st century projections of the IPCC AR4 models (Figure 7a in Held and Soden 2006) and the CMIP5 models (Fig. 2.1a). However, as the forced response is still weak relative to the natural variability, it is difficult to say whether East Africa will have drier or wetter long rains in the near future since this will strongly depend on the future evolution of natural variability.

Fig. 2.12b shows the multimodel composite SST anomaly pattern for dry East African MAM years of the CMIP5 historical simulations, after a 9-year running mean has been applied. Comparing with Fig. 2.2c, there are many differences from the observations. However, the CMIP5 historical simulations capture the observed relation with the SST gradient over the tropical Pacific Ocean, although the cool anomalies over the central tropical Pacific and the gradient are much weaker than observed. The significance of the composite SST anomaly pattern is indicated in Fig. 2.12c, where the composite is performed for each model and the number of models with positive composite values at each grid point is counted. This pattern is in general consistent with Fig. 2.12b with warm anomalies in the western tropical Pacific being the most robust model feature. The large negative values appearing over the Indian Ocean in Fig. 2.12b and 2.12c suggest that the Indian Ocean also is important for the decadal variability of the East African long rains in the CMIP5 coupled models. Comparing to Fig. 2.2, we see that the CMIP5 coupled models overestimate the Indian Ocean's relation to the East African long rains climate on these timescales.

As the multimodel mean of the CMIP5 historical experiments is poor in capturing the East African long rains-SST relationship and even simulates an incorrect climatology, it is interesting to examine the performances of the individual models. Fig. 2.13 shows the scatter plot of correlation coefficients against the differences of annual mean between the seasonal cycles of the East African precipitation in the CMIP5 historical simulations and that in GPCC. The mean values among the ensemble members for each individual model

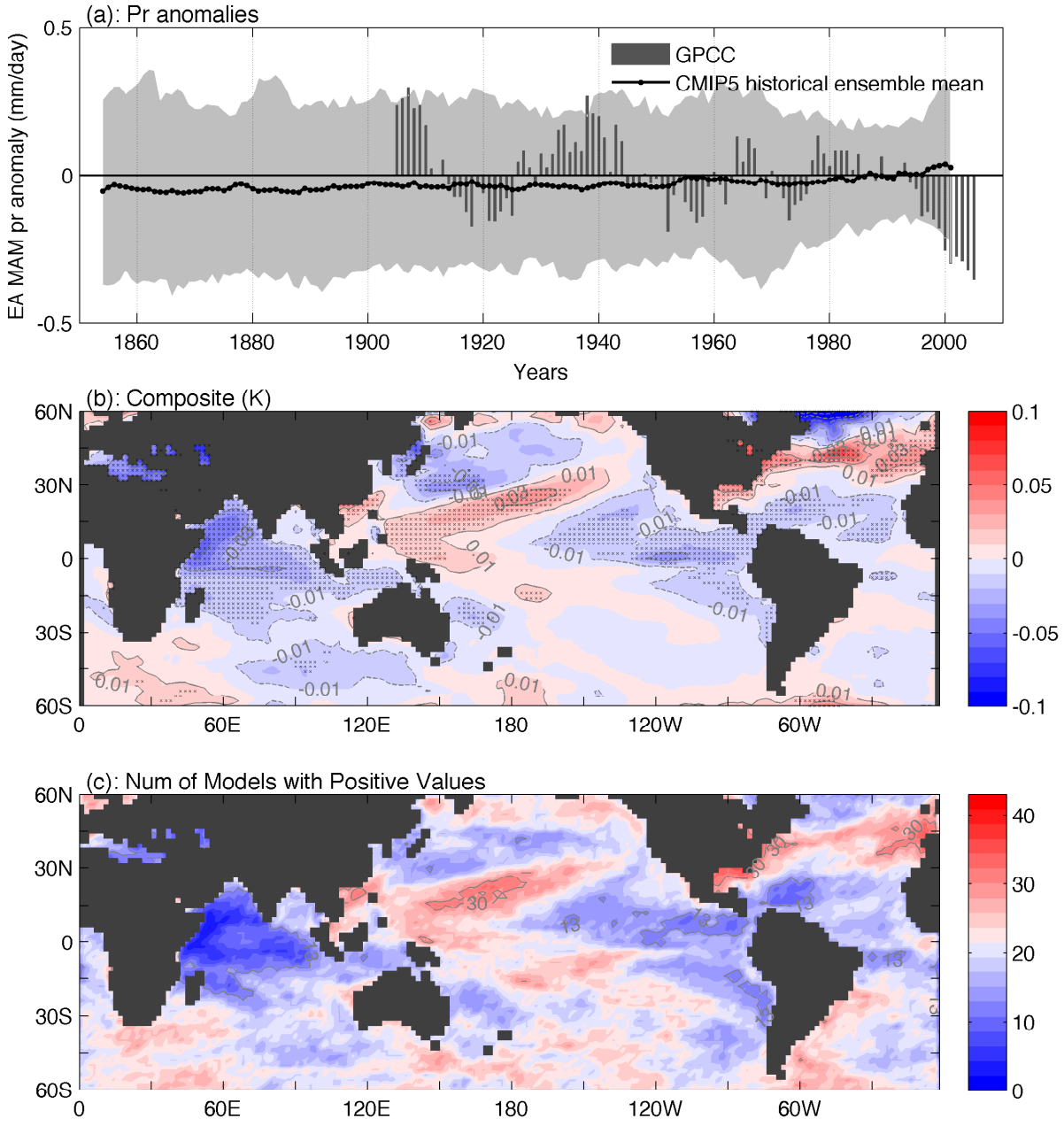

Figure 2.12: (a) and (b) are same as Fig. 2.8a and 2.8c respectively, but for CMIP5 historical multimodel runs instead of ECHAM4.5. (c): Number of models with positive values in the composite analysis.

are denoted by dots and the corresponding ranges are denoted by lines. The larger the correlation coefficients and the smaller the absolute values of the differences, the better the models' performance. The criteria that the correlation coefficients are > 0.6 and the absolute values of the differences are < 0.6 mm day^{-1} (denoted by the green box) leaves four models that are best in simulating the East African precipitation seasonal cycle: CSIRO-Mk3-6-0, HadCM3, IPSL-CM5A-MR and bcc-csm1-1-m. The four best coupled models indeed do a much better job in simulating the observed climatology (Fig. 2.14) than the multimodel mean (Fig. 2.11). Models CSIRO-Mk3-6-0 and bcc-csm1-1-m have almost the same long rains precipitation climatology as the observed although they both overestimate the short rains climatology, which is the same problem as in the case of the multimodel mean. Models HadCM3 and IPSL-CM5A-MR capture the short rains climatology very well but both underestimates the long rains climatology.

Are the four models that are best at simulating the East African precipitation climatology able to capture the precipitation-SST relationship in the observations as shown in Fig. 2.2c? Fig. 2.15 shows the ensemble mean of the composite SST anomalies when the East African long rains precipitation anomalies within each ensemble member are one standard deviation below from the mean and Fig. 2.16 shows the corresponding time series. Of the four coupled models, CSIRO-Mk3-6-0, IPSL-CM5A-MR and bcc-csm1-1-m capture the cool anomalies over the central and eastern Pacific, although the magnitudes are in general smaller than observed. HadCM3 has a contrast of cool/warm to the north/south of the equator over the tropical Pacific, which is totally different from the observed pattern. The observed positive bands in the southern and northern Pacific can only be seen in the CSIRO-Mk3-6-0 model. The CSIRO-Mk3-6-0 model seems to be the the only model that captures both the East African precipitation climatology and the East African long rains precipitation-SST relationship in the observations. The time series from the four models' simulations (Fig. 2.16) seem to have realistic amplitudes compared to the observed but they are not synchronous with it, which is expected due to internal variabilities. At least three of the four models (except CSIRO-Mk3-6-0) have a wetting trend for the multi-run mean since 1990, which is opposite to the observations, indicating limited skills of these

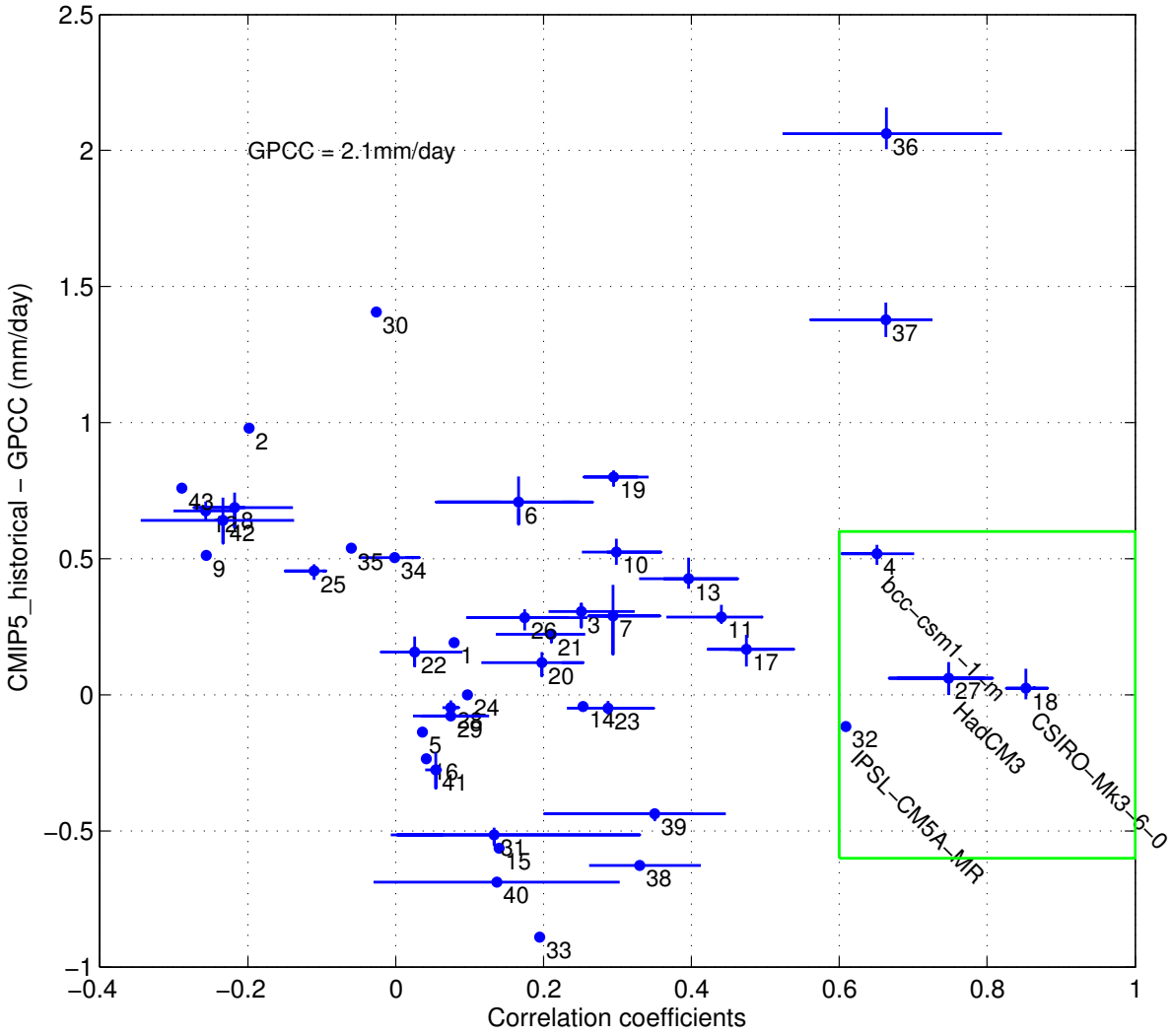

Figure 2.13: Scatter plot of correlation coefficients against annual mean differences between the climatology of East Africa precipitation in CMIP5 historical experiment models and that in GPCC. Blue dots denote the ensemble mean values of each model and the blue lines represent the range of ensemble members of each model. Numbers to the bottom-right of the blue dots are the indices of the forty-three CMIP5 historical experiment models. Models within the green box are the four best models based on the two scores of correlation coefficients and the annual mean difference.

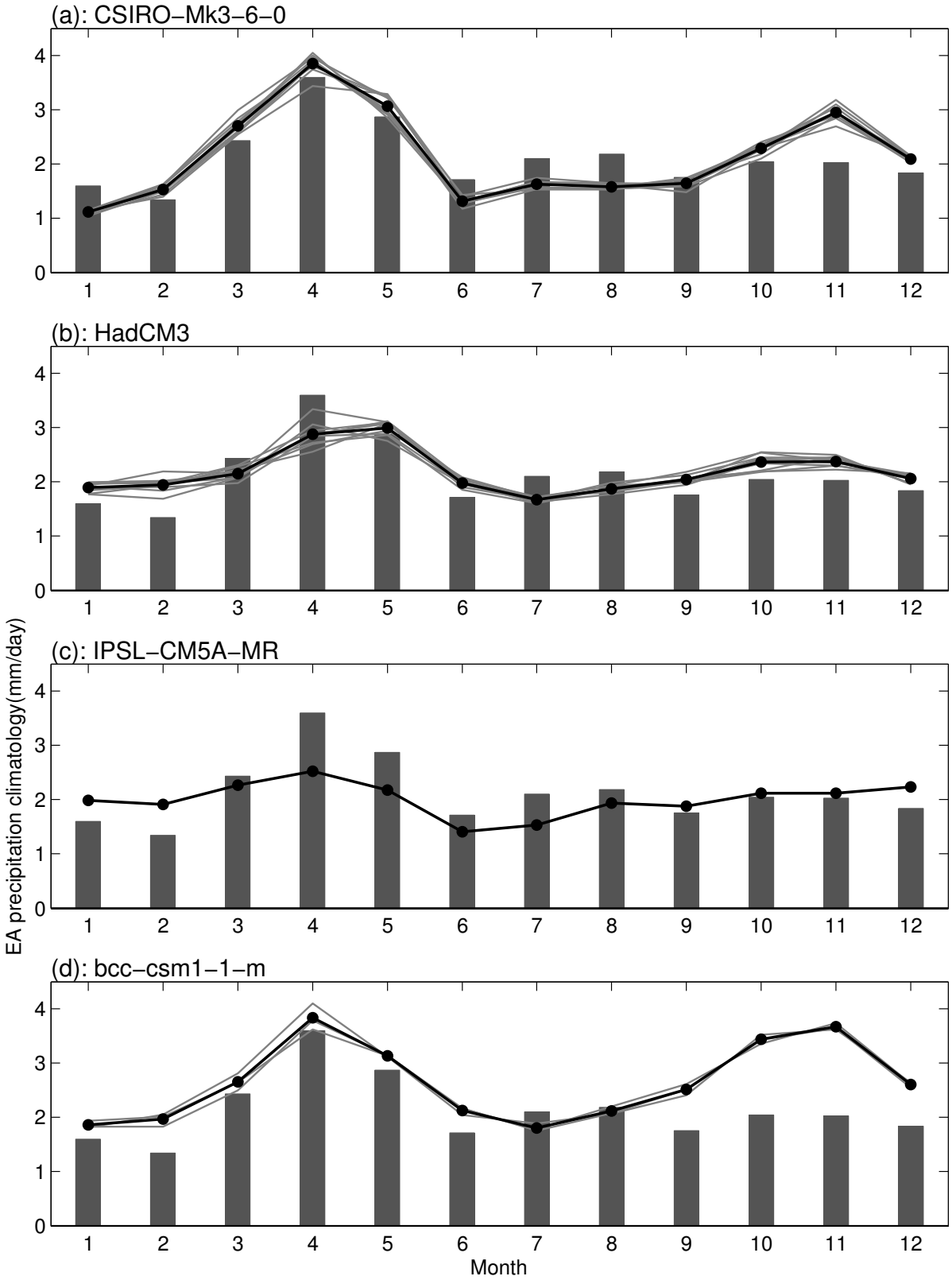

Figure 2.14: Same as Fig. 2.11 but for the four best models.

coupled models in predicting the East African long rains decadal variability.

2.6 Conclusion and discussion

The 2010-2011 East African severe drought raised the question of whether it is forced by anthropogenic emissions of greenhouse gases or just a phase of long term natural variability (Lott et al., 2013). Previous studies (e.g. Held and Soden 2006) and our own estimate from CMIP5 (Fig. 2.1a) show that the East African long rains are projected to get wetter under global warming, which is opposite to the recent drying trend. By using different methods of analysis and focusing on decadal variability, our study reveals that the drying trend is most likely part of decadal variability associated with natural SST variability mainly in the Pacific Ocean and with a La Niña-like pattern as in Lyon and DeWitt (2012) and Lyon et al. (2013). The following conclusions have been reached:

- The drying trend of the East African long rains in recent decades most likely arises from natural decadal variability and is not anthropogenic origin.

- The decadal variability of the East African long rains can be explained by the decadal variability of SST over the Pacific ocean. The dry phases of the East African long rains are associated with positive SST anomalies over the western tropical Pacific and negative anomalies over the central and eastern tropical Pacific (La Niña-like).

- ECHAM4.5 and 5 from the SST-forced IRI forecast models are able to capture the precipitation climatology, the SST anomaly pattern associated with decadal variability and the drying trend in recent decades. However, not all the models perform well (e.g. CCM3.6 is not even able to capture the recent drying trend.)

- The SST-forced models of the CMIP5 AMIP experiments also capture the climatology of the East Africa precipitation, although with varying skills. The simulated East African long rains anomaly, which is only available over a short period, does capture the recent observed drying trend in the multimodel mean and the associated SST anomaly pattern is consistent with the observed.

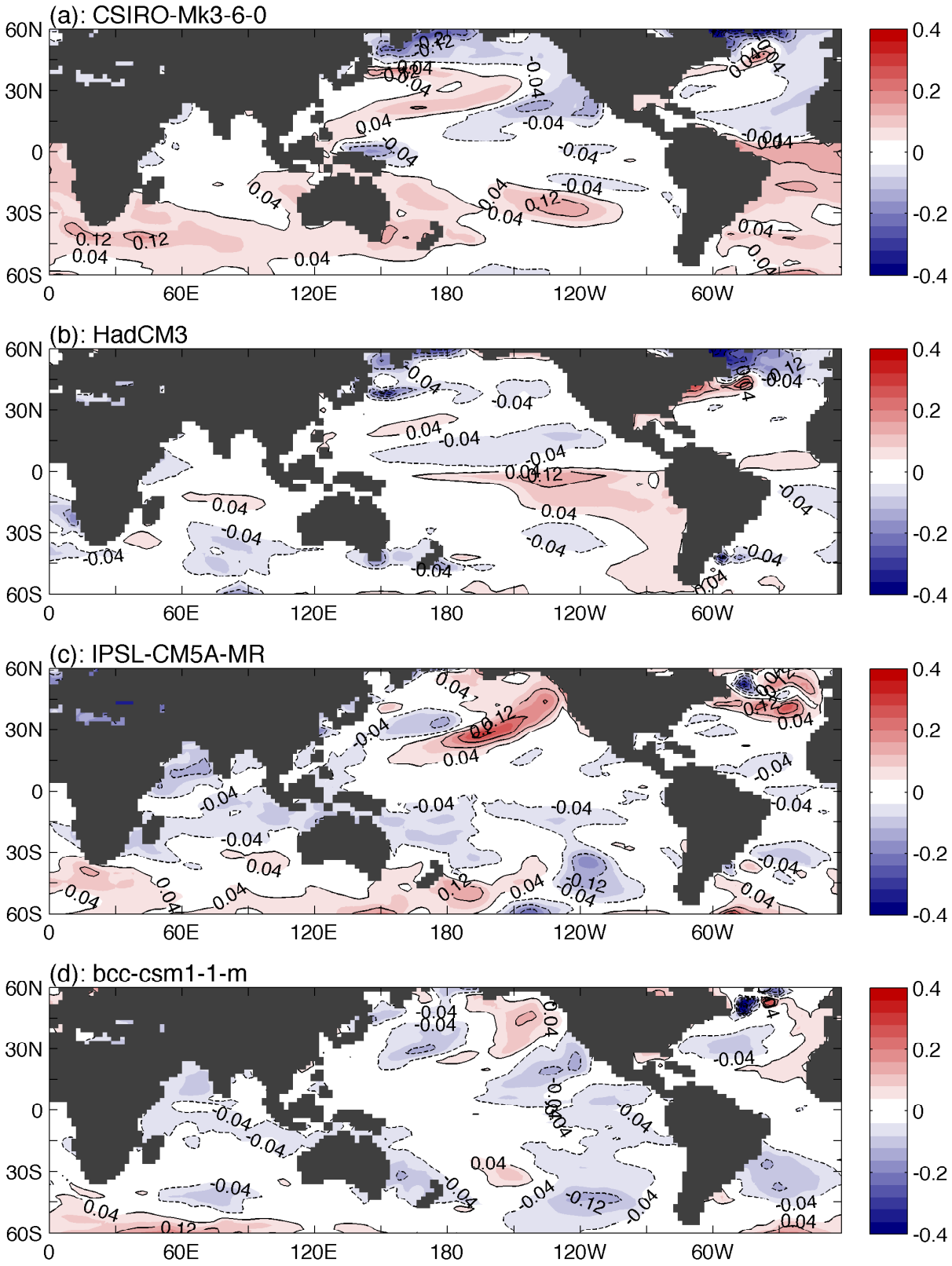

Figure 2.15: Same as Fig. 2.12b but for the four best models.

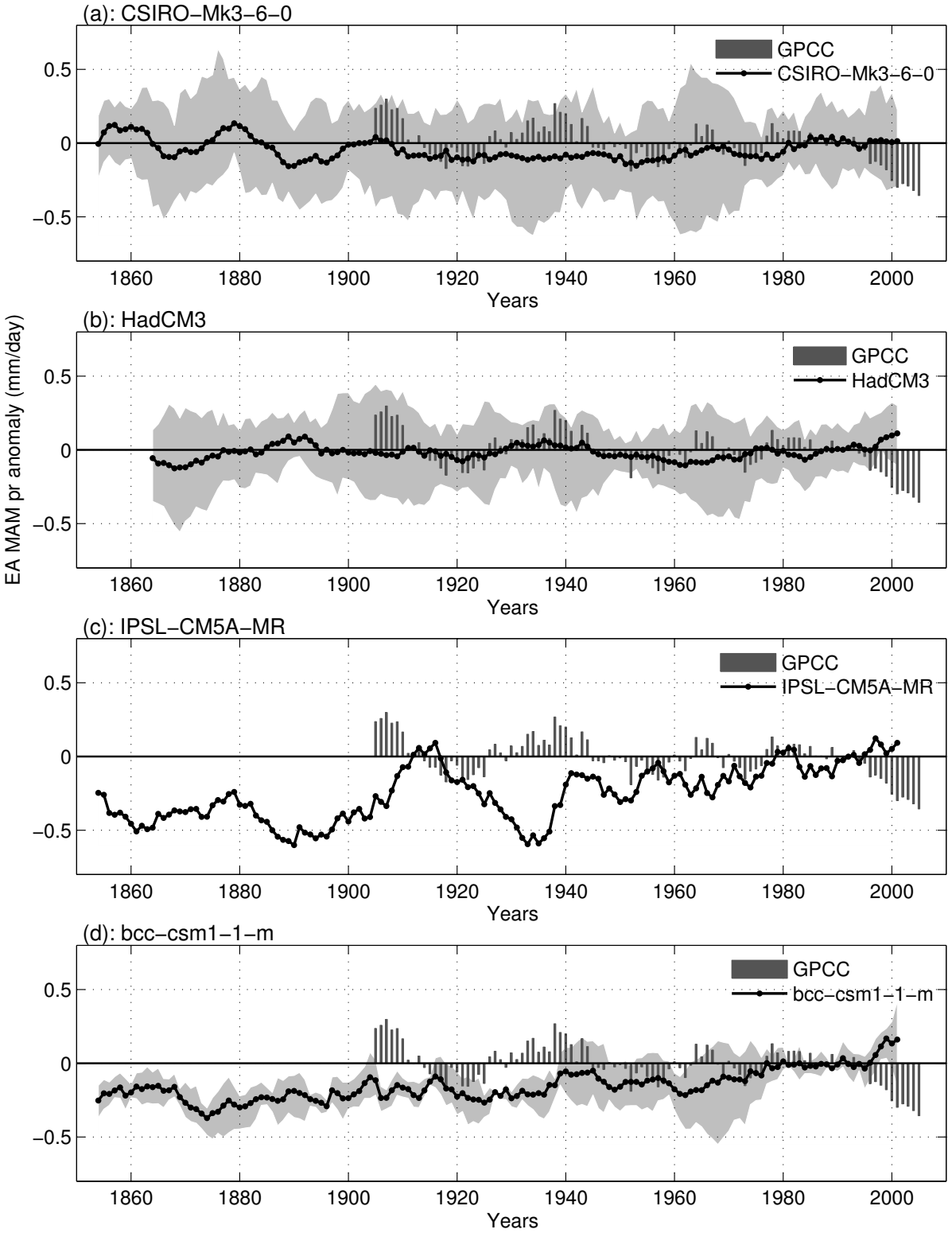

Figure 2.16: Same as Fig. 2.12a but for the four best models.

- The multimodel mean of the fully coupled models of the CMIP5 historical experiment underestimates the East African long rains and overestimates the short rains with a considerable range of performance among the individual models. The multimodel mean of the precipitation anomalies shows a weak wetting trend since 1950 that is much smaller than the internal variability. The SST anomaly pattern associated with the dry phase of the East African long rains is associated with a SST gradient over the tropical Pacific, although the magnitude of this is weak compared to observations.

- CSIRO-Mk3-6-0 is the best model among the CMIP5 historical experiment coupled models that captures both the East African precipitation climatology and the East African long rains-SST relationship in the observations.

While SST-forced models are able to capture the recent drying trend in the East African long rains and much of the decadal variability since 1950s, fully coupled models, however, have systematic errors in simulating the East African precipitation climatology (i.e. underestimating the long rains precipitation while overestimating the short rains precipitation) and give somewhat different SST patterns associated with decadal variability of the East African long rains. This lack of coupled model skill casts doubt on projections of future East African precipitation and on the use of these models to understand past variations (e.g. Tierney et al. 2013).

Strong internal decadal variability of the long rains precipitation in East Africa, and the generally poor ability of models to reproduce this and its atmosphere-ocean causes, means that our ability to predict future variations is very limited. It should not be assumed that recent drying trends represent an anthropogenically forced precipitation change and they will continue. Nor should it be assumed that the model projection of wetting in response to rising greenhouse gases is correct. We are distressingly far from an adequate understanding or a usable ability to model climate variability and change in this socially critical region.

CHAPTER 3

The Annual Cycle of East African Rainfall in Observations *

3.1 Introduction

East Africa has experienced an increased frequency of droughts in recent years, primarily due to the decline of rainfall during the March–May (MAM) "long rains" (a term used in Kenya/Tanzania/Uganda, which is called "belg" or "small rains" in Ethiopia, and "Gu" in Somalia), threatening the lives of millions of people in this hydrologically and politically vulnerable region (FEWS NET, 2011; Lyon and DeWitt, 2012). Various mechanisms have been proposed for this long rains drying trend. Williams and Funk (2011) related it to the westward extension of the Indo-Pacific warm pool and associated Walker circulation while Lyon and DeWitt (2012) and Lyon et al. (2013) linked it to a shift of sea surface temperature (SST) over the Pacific basin to a La Niña-like pattern, occurring around 1998–99. A recent study (Yang et al., 2014b) demonstrated that the East African long rains exhibit variability on decadal or longer time scales and the recent drying trend is very likely part of this Pacific-centered decadal variability. Yet droughts in recent years are unprecedented in terms of their severity over the past century.

Given the recent decline of the long rains, people are inevitably wondering what will happen in the next few decades, particularly as the climate warms due to continued anthropogenic emissions of greenhouse gases (GHGs). There is a strong consensus in model projections from the Intergovernmental Panel on Climate Change (IPCC) Fourth Assessment Report (AR4) and the more recent Coupled Model Intercomparison Project Phase 5 (CMIP5, Taylor et al. (2012)) that the pattern of precipitation minus evaporation ($P - E$) will be enhanced in the warming climate (Held and Soden, 2006; Seager et al., 2010; Laîné et al., 2014), which implies that the East African long rains will increase as

* The work of this chapter has been accepted and in press as: Yang, W., R. Seager, M. A. Cane, and B. Lyon, 2014: The Annual Cycle of the East African Precipitation. *J. Clim.*, **in press**, doi: 10.1175/JCLI-D-14-00484.1.

they are part of the Intertropical Convergence Zone (ITCZ). This implies a recovery from recent dry conditions, at least in part, in the coming decades. Indeed, this is the case in the CMIP5 model projections as shown in Fig. 2b of Yang et al. (2014b). However, some studies using high-resolution regional climate models forced by ensemble-mean global climate model (GCM) projections on the lateral and ocean boundaries indicate a reduction in the long rains (Vizy and Cook, 2012b; Cook and Vizy, 2013), leaving the long rains projections more uncertain.

While GCMs display some consistency in their projections of East African precipitation, the models' capabilities in simulating the observed climatology and temporal variability are less clear. By examining the performance of both SST-forced models and the coupled models used in the CMIP5 historical experiment in simulating the East African long rains, Yang et al. (2014b) showed that, while some of the SST-forced models are able to capture the observed decadal variability of the long rains, the coupled models, which are used for the 21st century climate projections, generally fail to capture the correct long rains-SST relationship. Moreover, the coupled models misrepresent the East African precipitation annual cycle by overestimating rainfall during the October–December (OND) "short rains", as was also reported for the CMIP3 coupled models (Anyah and Qiu, 2012).

To understand the discrepancy between the model simulations and observations, we first need to better understand the observed East African precipitation climatological annual cycle. This has drawn little attention in the past compared to inter-annual variability but is a very important issue and the motivation of this study. It is also of interest to explain why East Africa is in general semi-arid but has a bimodal annual cycle of precipitation. In this paper, we investigate the atmospheric thermal conditions, circulation, and moisture budget associated with the annual cycle of precipitation in this region and try to address the following questions: why is deep-tropical East Africa largely semi-arid/arid in terms of annual mean rainfall (Trewartha, 1961; Nicholson, 1996)? Why are there two rainy seasons? What atmospheric environment conditions set the difference between the rainy seasons and the dry seasons? What explains the difference between the two rainy seasons? Why are the long rains stronger than the short rains? The remainder of this

chapter is organized as follows: Section 4.2 describes the data used in the study; Section 3.3 briefly reviews the observed precipitation and topography in East Africa; analyses of the atmospheric thermal condition, atmospheric circulation and moisture budget are presented in Sections 3.4, 3.5 and 3.6, respectively; the main conclusions of the paper and associated discussion are provided in Section 4.5.

3.2 Data

For precipitation, we use version 6 of Global Precipitation Climatology Centre (GPCC) monthly precipitation (Rudolf et al., 2010), which is a gauge-based, 0.5^0 longitude $\times$ 0.5^0 latitude gridded global land surface dataset for the period 1901–2010 available from `http://iridl.ldeo.columbia.edu/expert/SOURCES/.WCRP/.GCOS/.GPCC/.FDP/.version6/.0p5/.prcp/`. For comparison, we also use version 2.2 of the Global Precipitation Climatology Project (GPCP) monthly precipitation dataset from 1979 to 2010 (Huffman et al., 2009), which combines gauge observations and satellite data into 2.5^0 longitude $\times$ 2.5^0 latitude global grids and is available from `http://iridl.ldeo.columbia.edu/expert/SOURCES/.NASA/.GPCP/.V2p2/.satellite-gauge/.prcp/`. The observed sea surface temperature (SST) is from version 3b of the NOAA National Climate Data Center (NCDC) Extended Reconstructed Sea Surface Temperature (ERSST) (Smith et al., 2008), which is a globally gridded monthly dataset with a spatial resolution of 2^0 longitude $\times$ 2^0 latitude from 1854 to the present and available from `http://iridl.ldeo.columbia.edu/expert/SOURCES/.NOAA/.NCDC/.ERSST/.version3b/.sst/`.

To estimate the thermal conditions, circulation and moisture budget, we use the European Centre for Medium-Range Weather Forecasts (ECMWF) Interim Re-Analysis (ERA-Interim) (Dee et al., 2011), which covers the post-1979 period and is the latest of the ECMWF reanalyses. ERA-Interim is generally considered to be improved in many aspects compared to its precursor, the 40-yr ECMWF Re-Analysis (ERA-40) (Berrisford et al., 2011). In this paper, all seasonal climatologies and annual cycles are computed based on a 1979–2009 base period with the seasons defined as: winter dry season(January–February, or JF); the long rains season (MAM), the summer dry season (June–September,

or JJAS) and the short rains season (OND). These definitions follow the largely bimodal precipitation annual cycle found over much of this region.

3.3 Precipitation and topography

The uniqueness of East African precipitation can be seen from Fig. 3.1. While most tropical lands have a wet annual climatology, much of East Africa is dry with precipitation less than 2 mm day^{-1} (Fig. 3.1a), consistent with a previous study (e.g. Fig. 16.7 in Nicholson, 2011, p. 299). Some regions (including the western and eastern coastal areas of South America between 0^0 and 12^0S and the northern African interior around 10^0N) also have a precipitation climatology less than 2 mm day^{-1}, but the area is not comparable in scale with East Africa. The 12^0S–12^0N GPCC climatological annual mean precipitation as shown in Fig. 3.1b demonstrates that tropical land generally has less precipitation in Africa than South America and the Maritime continent, and East Africa is even drier than western Africa. The eastern Horn region is the precipitation minimum at all longitudes.

Fig. 3.1c (shading) shows the normalized annual cycle of GPCP monthly climatology at 5^0N (the latitude is denoted by a blue horizontal line in Fig. 3.1a). East African longitudes at this latitude have a distinctive bimodal annual precipitation cycle, with the major and minor peaks in April and October, respectively. Other longitudes over land generally only have a single peak, although the peak months differ for different longitudes. For example, the annual cycle of precipitation over South America largely peaks between May and July, while for the African interior longitudes, the peaks are between July and October. It should be noted that the western end of Africa at 5^0N does have a bimodal annual cycle, but the two peaks are often viewed as one rainy season that is interrupted by the so-called midsummer drought (Karnauskas et al., 2013). Fig. 3.1d shows the annual cycles of downward, top of the atmosphere (TOA) solar radiation at 5^0N (red line with circles). The two peaks of the solar radiation annual cycle (March and September) lead the two corresponding East African precipitation peaks by one month. The solar radiation is also greater in the boreal summer season than the winter season but precipitation over East African longitudes in boreal summer is comparable with or less than that in the

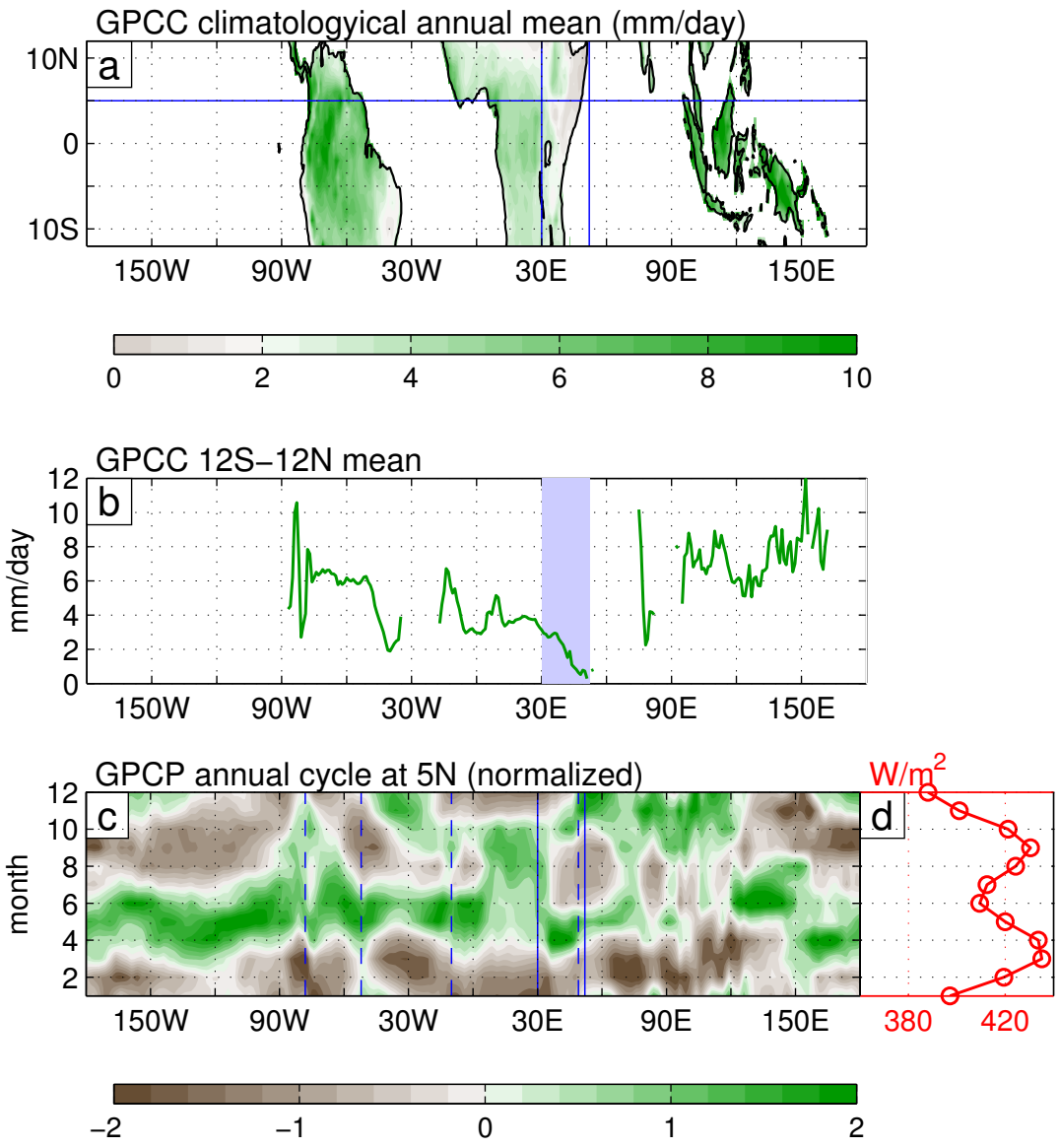

Figure 3.1: a) GPCC climatological annual mean precipitation. The vertical and horizontal blue lines are at the 30^0E and 52^0E longitudes and the 5^0N latitude, respectively. b) 12^0S–12^0N averaged GPCC climatological annual mean precipitation in panel a. The shaded rectangle marks the longitudinal range of East Africa (30^0E–52^0E). c) Normalized annual cycle of GPCP monthly climatology at 5^0N (shading). Vertical blue solid lines indicate 30^0E and 52^0E and dashed lines indicate the longitudinal edges of South America and Africa at 5^0N. d) Annual cycle of the monthly climatology of downward, top of the atmosphere solar radiation at 5^0N from NCEP/NCAR reanalysis. All climatologies are estimated based on the period of 1979–2009.

winter, suggesting that it is difficult to simply attribute the East African precipitation annual cycle directly to the incoming solar radiation forcing.

One of the major factors responsible for the climate in East Africa is the complex topography (Nicholson, 1996; Lyon, 2014). Fig. 3.2 shows the topographic elevation map of East Africa. The topography of East Africa can be roughly characterized by the coastal plain to the east and the generally north-south orientation of the interior highlands. The highlands to the north (the Ethiopian Highlands) and to the south (the East African Highlands) are separated by a narrow gap (the Turkana Channel), which connects the area of relatively low topography to the northwest and the eastern coastal plain. Local variations in climate over East Africa are greatly influenced by these topographical features as they play an important role in the low-level atmospheric circulations and moisture transport (Findlater, 1969; Kinuthia and Asnani, 1982; Kinuthia, 1992).

The annual cycle of precipitation over much of East Africa shows a bimodal distribution although in some regions a unimodal distribution dominates. In order to show the spatial distribution of the precipitation annual cycle types, the Fourier harmonics of the precipitation annual cycle are estimated in the GPCC data at each grid point and the ratio $|c_2/c_1|$ of the amplitude of the semi-annual-period harmonic c_2 (representing the bimodal distribution) to the annual-period harmonic c_1 (representing the unimodal distribution) is calculated. Fig. 3.3 shows the spatial distribution of the binary logarithm of this ratio so that positive (negative) values occur where the bimodal (unimodal) distribution dominates. It can be seen that the bimodal distribution dominates to the east of the highlands and near the equator while the unimodal distribution dominates over the southern and northwestern parts of the study domain. The average precipitation annual cycle over box 1 (shown to the right of the box) has the typical two rainy seasons in East Africa: the long rains in MAM and the short rains in OND. In contrast, boxes 2 and 3 only have one rainy season: the precipitation peaks during boreal summer over box 2 and during austral summer over box 3, both showing a typical monsoonal character.

An even simpler way to identify the bimodal areas from the unimodal areas is to compare the precipitation rate during the long rains season (pr_{MAM}) with that during

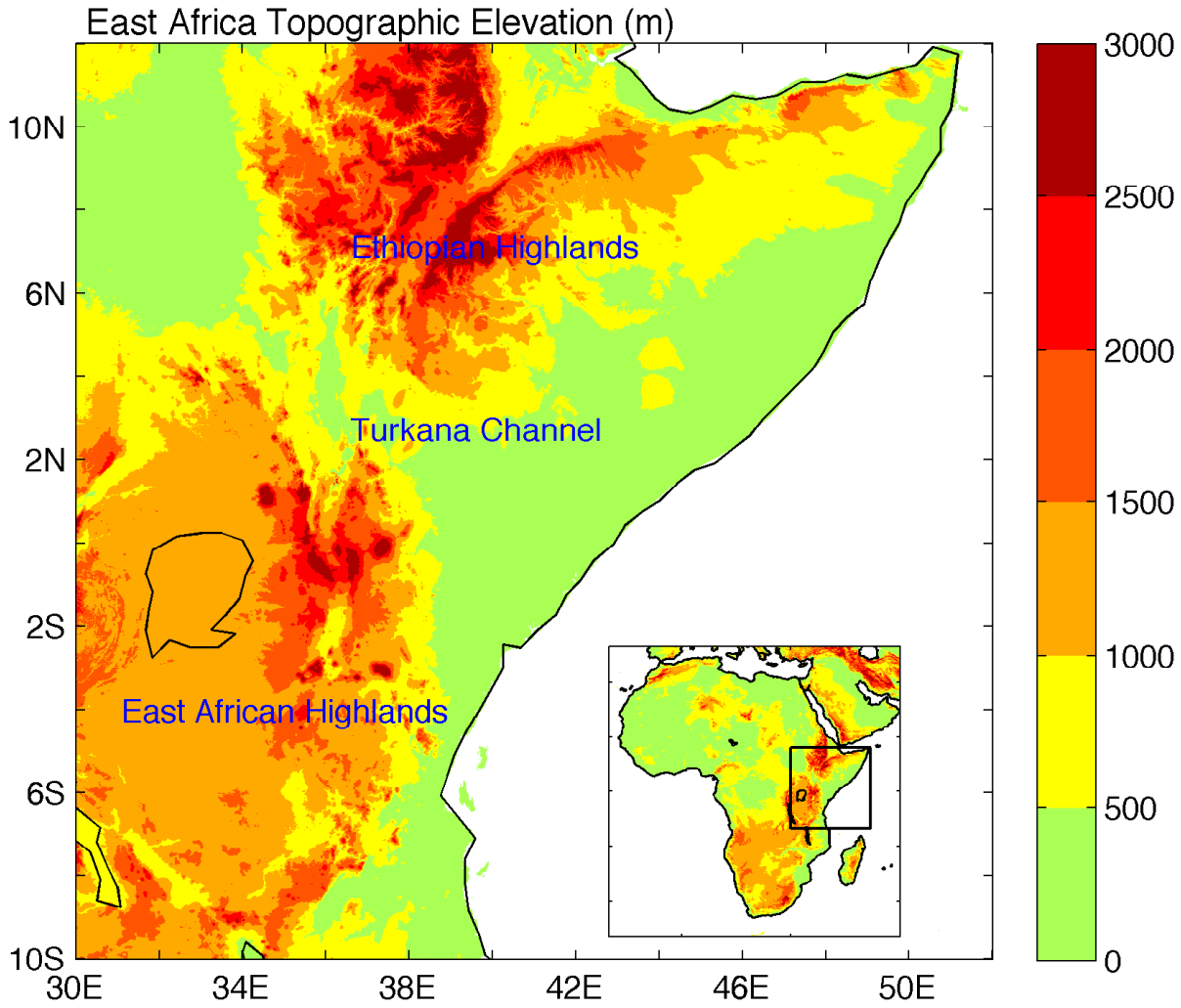

Figure 3.2: Topographic elevation map of East Africa. The insert shows the topographic elevation for all of Africa and a box indicating the East African region of focus in this study.

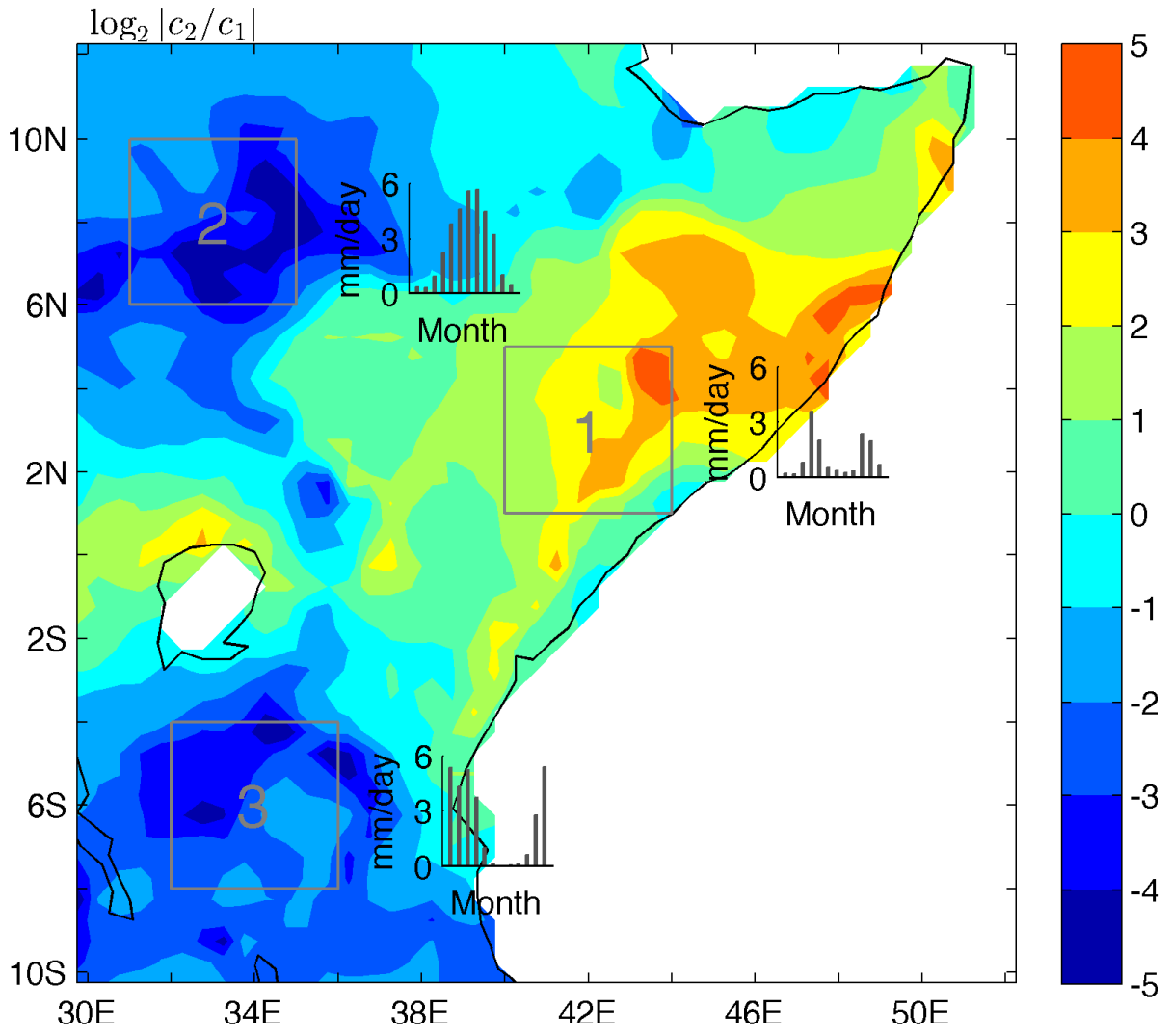

Figure 3.3: Distribution of precipitation (from GPCC) annual cycle type, which is measured by $\log_2 |c_2/c_1|$, where c_1 and c_2 are the Fourier harmonics of the annual period and the semi-annual period, respectively. Positive (negative) values occur when the semi-annual (annual) period mode dominates. Boxes 1, 2 and 3 have ranges of [40^0E, 44^0E] $\times$ [1^0N, 5^0N], [31^0E, 35^0E] $\times$ [6^0N, 10^0N] and [32^0E, 36^0E] $\times$ [8^0S, 4^0S] respectively. Bar graphs next to the boxes show the annual cycle of precipitation averaged over the corresponding boxes.

the boreal summer (pr_{JJAS}) and during the boreal winter (pr_{JF}) and select the areas satisfying the criteria: $pr_{MAM} > pr_{JJAS}$ and $pr_{MAM} > pr_{JF}$. The results are highlighted as gray shadings in the mini panel in the middle of Fig. 3.4 and mainly cover the areas to the east of the highlands, a similar pattern to that with the positive-values in Fig. 3.3. Hereafter the term "East Africa" is used to refer to the gray-shaded areas in Fig. 3.4 when an area average is implied. The area-averaged precipitation annual cycle over the shaded area is shown in Fig. 3.4 and has the typical bimodal annual precipitation cycle of East Africa. Both the GPCC and GPCP precipitation datasets show similar results, with wettest conditions during the long rains season (area average precipitation greater than 2 mm day^{-1}), relatively wet conditions during the short rains season (precipitation between 1.5 mm day^{-1} and 2.5 mm day^{-1}) and comparatively dry conditions during other seasons (precipitation less than 1.5 mm day^{-1}). April is the wettest month of the year, with precipitation close to 4 mm day^{-1}.

What is the spatial distribution of precipitation during the different seasons? Fig. 3.5 shows the seasonal climatologies of precipitation over East Africa. Months not covered by the long rains and the short rains are grouped into the boreal winter season (JF) and the boreal summer season (JJAS) as mentioned previously. During the long rains (Fig. 3.5b), the precipitation rate over the coastal areas to the east of the highlands peaks and in general exceeds 1 mm day^{-1} except in the northeastern extreme of the Horn. The short rains (Fig. 3.5d) show a similar precipitation pattern to the long rains but with a slightly weaker magnitude. During the boreal winter season (Fig. 3.5a), the precipitation maxima appear over the southern extreme of the study domain, and are part of the ITCZ. The northern half of the region is generally dry except for some small areas over the highlands. During the boreal summer season (Fig. 3.5c), the largest rainfall amounts are found in the northwest, especially over western areas of the northern highlands, where they form the eastern reach of the West African monsoon. Moderately wet conditions are also found right on the east coast between 6^0S and 2^0N during JJAS, probably caused by an onshore breeze. Other regions are generally dry during this season.

Fig. 3.5 also shows the climatological values of SSTs off the east coast and it is seen

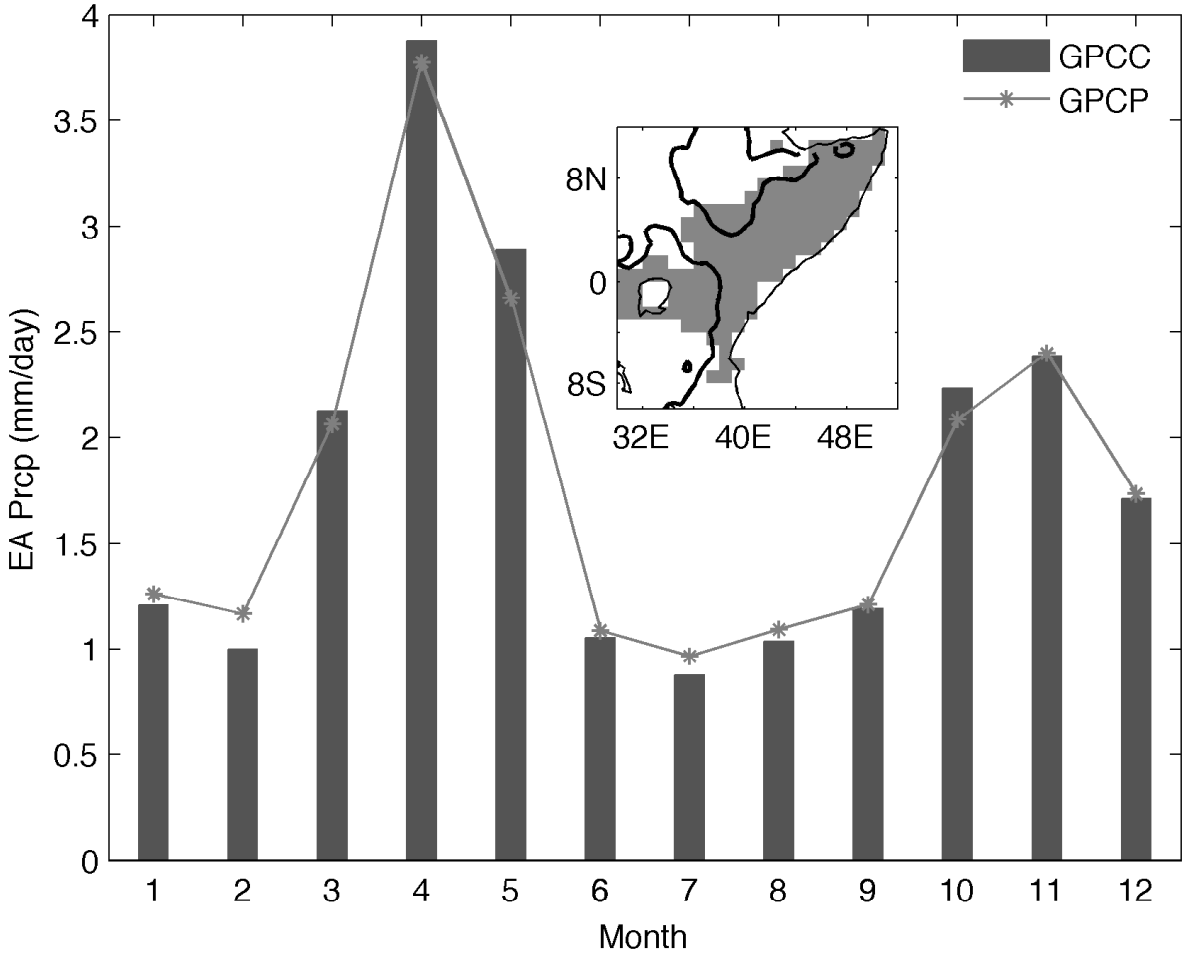

Figure 3.4: The annual cycle of East African area-averaged precipitation from GPCC and GPCP. The grid points to be averaged are chosen by the criteria that the precipitation rate during the long rains (MAM) is greater than that during both boreal summer (JJAS) and boreal winter (JF) so that the areas with bimodal precipitation annual cycle are focused on. The mini panel in the middle shows the areas satisfying the criteria (gray shading), which resemble the areas with positive values in Fig. 3.3. The thick black lines are the 1000 m topographical elevation contours.

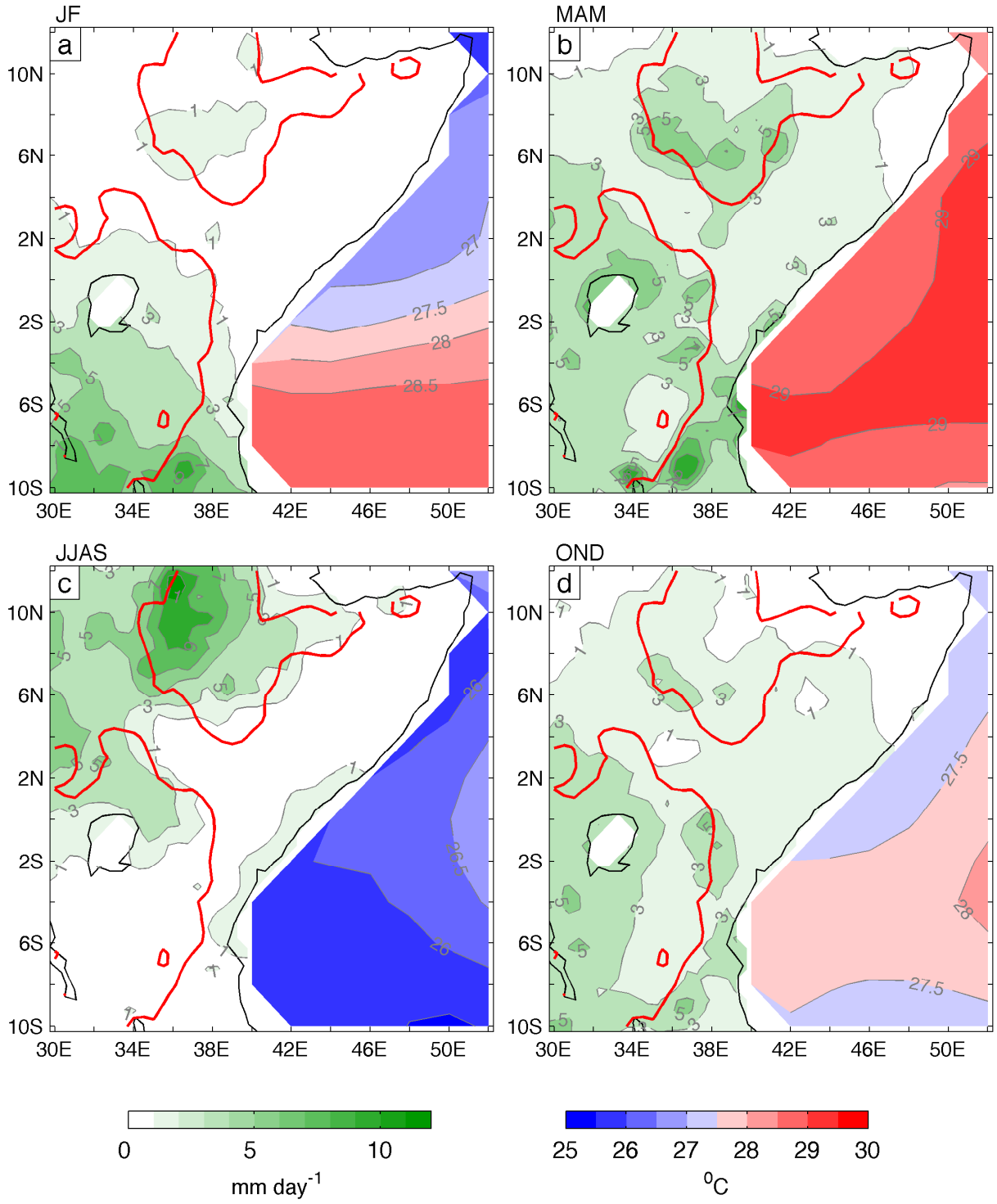

Figure 3.5: Seasonal climatologies of precipitation (mm day^{-1}) from GPCC over East Africa and SST (^{0}C) from ERSST off the east coast. The red lines are the smoothed contours of the 1000 m topographical elevation.

that the seasonal precipitation to the east of the highlands co-varies with the near-coast SSTs. SSTs are highest during the long rains season (greater than 28.5 ^{0}C) and are around 1.5 ^{0}C cooler, yet with a similar pattern, during the short rains season. SSTs are coolest during boreal summer when the overall coastal conditions are driest. During boreal winter, a relatively strong north-south SST gradient is evident and there is an associated gradient in precipitation between the north and the south. The relationship between the East African precipitation and the near-coast SST, or the western equatorial Indian Ocean (WEIO) SST, is further demonstrated in their annual cycles in Fig. 3.6. Despite of imperfect month-to-month covariation, both the precipitation and SST peak in April and have the overall lowest values during the July–September season. It is noted that the JF SSTs are as high as the November and December values, yet the JF season is as dry as the boreal summer season. This might be due to the strong north-south SST gradient in JF as shown in Fig. 3.5a: the cool SST in the north is related to the dry condition over much of East Africa while the warm SST in the south contributes to the similarly high area-averaged SST as in the OND season.

The precipitation-SST relationship suggests that SSTs might play an important role in the annual cycle of East African precipitation. Previous studies (McCreary et al., 1993; Murtugudde et al., 1996, 2007) demonstrated that both surface heat flux and ocean dynamics play import roles in the annual cycle of Indian Ocean SSTs. For example, during boreal summer, the cold SSTs off the coast of East Africa are driven by a wide range of processes including upwelling, horizontal advection, mixed layer entrainment and latent flux (McCreary et al., 1993). These results imply that external forcings that are responsible for the East African precipitation annual cycle might be intrinsically complex.

3.4 Atmospheric thermal condition

Tropical precipitation is strongly connected with the thermal state of conditional instability (Emanuel et al., 1994). One simple measurement of this instability is the difference between the surface moist static energy (MSE, which is defined as $h = c_pT + Lq + gz$, where c_p, T, L, q, g and z are specific heat capacity at constant pressure, absolute air

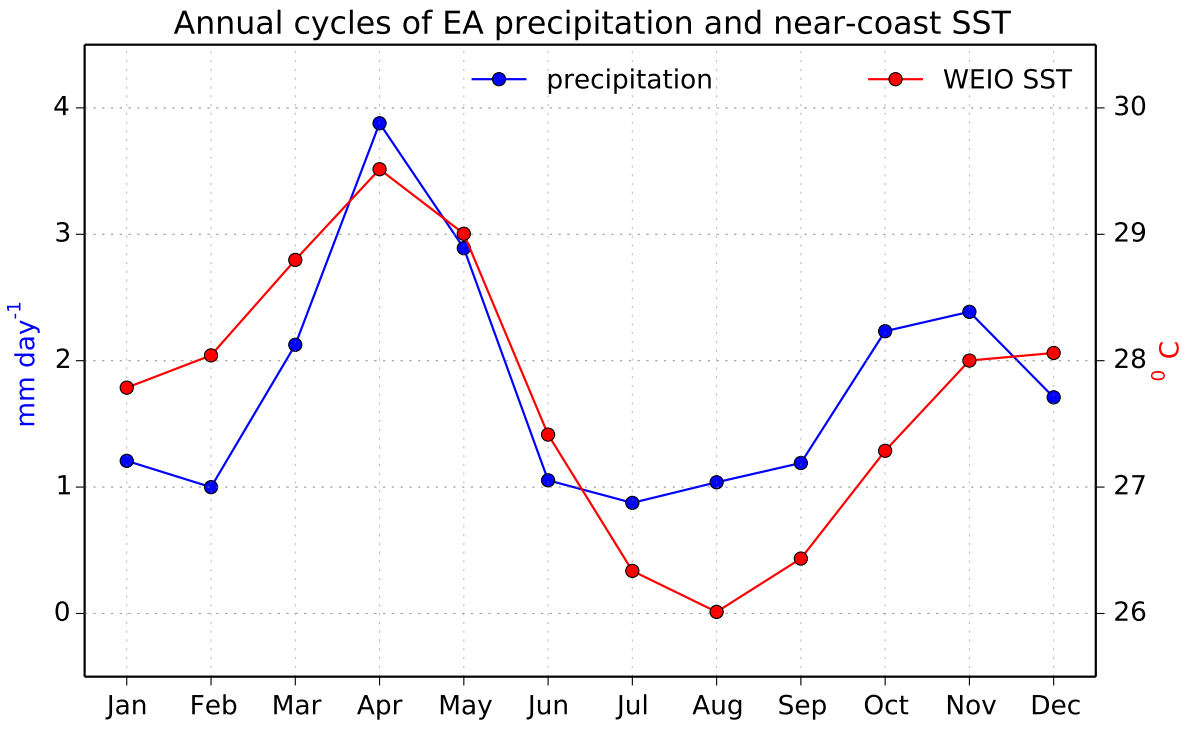

Figure 3.6: East African precipitation annual cycle from GPCC (blue line) and annual cycle of SST over the western equatorial Indian Ocean (WEIO, ocean area within 10^0S–10^0N and 30^0E–60^0E, red solid line).

temperature, latent heat of evaporation, gravity acceleration and the height above the surface, respectively) and the saturated MSE at 700 hPa (denoted as $h_s - h^*_{700hPa}$). 700 hPa is chosen as the first standard pressure level clearly above the boundary layer. A similar definition can also be seen in Cook and Seager (2013). Fig. 3.7 shows the seasonal climatologies of $h_s - h^*_{700\text{hPa}}$ (which has been normalized by the heat capacity of the air at constant pressure c_p so it has the unit of degree Kelvin). In JF (Fig. 3.7a), there is a strong north-south gradient of the conditional instability seasonal climatology (colors). Most areas over the northern half of the region are also extremely stable, corresponding to the dry areas in Fig. 3.5a. Southern areas are less stable, favoring much wetter conditions. The north-south gradient in the seasonal climatology of stability and precipitation during JF arises mainly from a similar pattern of changes from the previous season (contours). In MAM (Fig. 3.7b), the stability weakens over northern areas and slightly strengthens over the extreme south which is accompanied by northward expansion of the precipitation and the occurrence of the long rains as shown in Fig. 3.5b. In JJAS (Fig. 3.7c), the stability continues to weaken over the northwest monsoon area but strengthens elsewhere, resulting in a northwest-southeast gradient of stability over the region, corresponding to a similar pattern of precipitation in this season (Fig. 3.5c). In OND (Fig. 3.7d), stability strengthens over the northwest but weakens over most of the east, which is accompanied by the short rains season (Fig. 3.5d).

The seasonal climatologies of the conditional instability and the season-to-season changes over East Africa are dominated by the changes in surface MSE (h_s, Fig. 3.8) rather than the 700 hPa saturated MSE ($h^*_{700\text{hPa}}$, not shown), as shown by the resemblance of Fig. 3.8 to Fig. 3.7 (colors and contours). Fig. 3.9 shows the annual cycles of the surface MSE and the saturated MSE at 700 hPa over the bimodal precipitation areas (shaded areas in Fig. 3.4). The amplitude of the surface MSE cycle is around three times stronger than that of the 700 hPa saturated MSE cycle. As a result, the difference between the two (the gray line) has a pattern similar to the surface MSE. While the annual cycle of the 700 hPa saturated MSE is dominated by the annual harmonic, which probably arises from the dominance of annual harmonic of SST near the equator

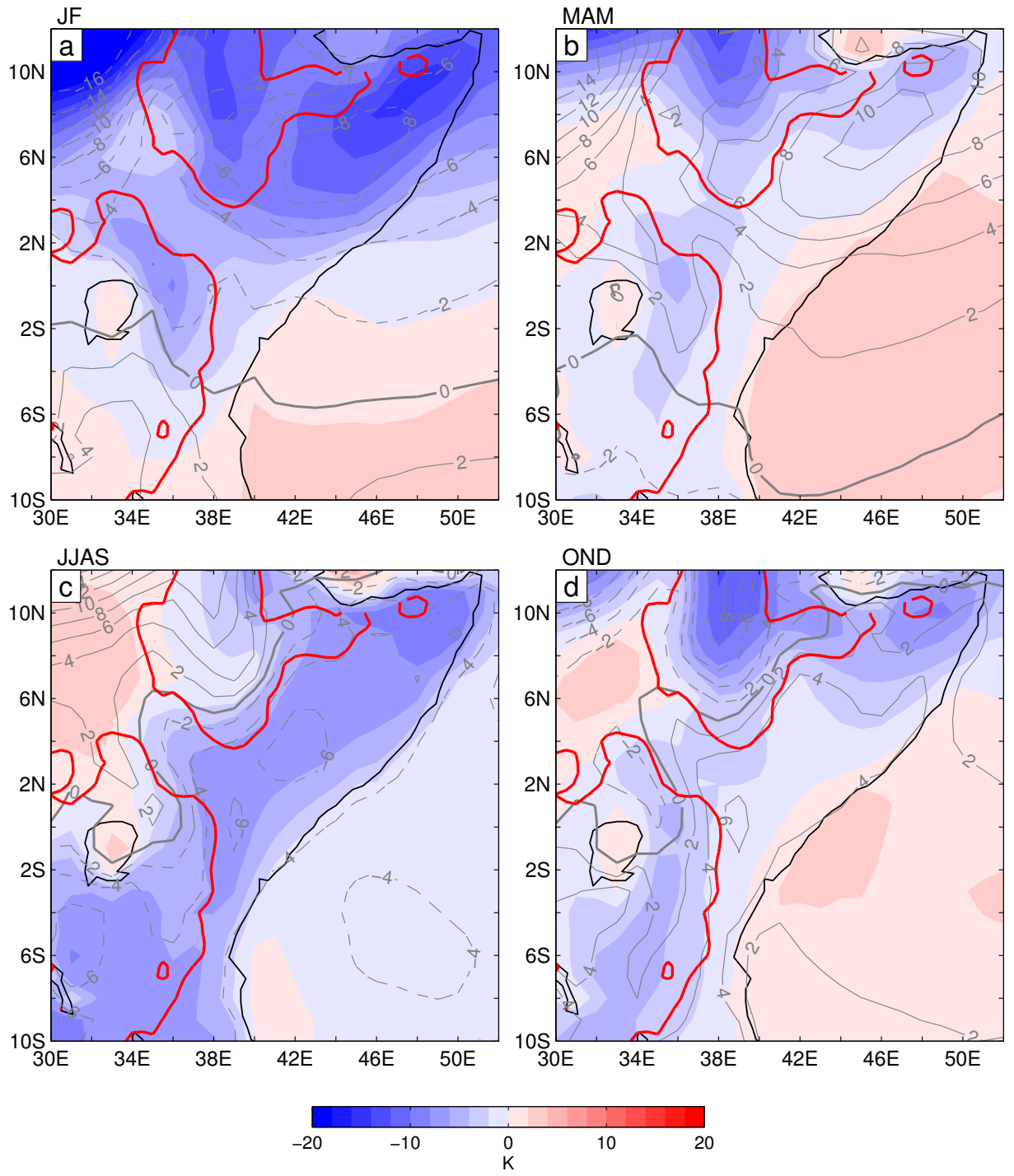

Figure 3.7: Seasonal climatologies of the surface moist static energy (MSE) minus the saturated MSE at 700 hPa (colors) and their changes from the previous season (contours), both from the ERA-Interim Re-Analysis. The MSE is normalized by the heat capacity of the air at constant pressure so that it has the unit of degree Kelvin. The thick red lines are the contours of the 1000 m topographical elevation.

(Schneider, 1996), the surface MSE is dominated by the semi-annual harmonic, similar to the precipitation annual cycle. Large surface MSE appears during the two rainy seasons, with values during the long rains larger than for the short rains. April is the month of maximum surface MSE across the year, consistent with the maximum precipitation rate during this month (Fig. 3.4).

We further decompose the surface MSE into the component associated with temperature and the component associated with moisture (the component of MSE associated with geo-potential height has little seasonal variation and is not discussed here). The seasonal cycle of the surface MSE is dominated by the moisture component (Fig. 3.10) and the variation of the temperature component can largely be neglected (only around one fifth of the moisture component and not shown here). Both the seasonal climatologies, and the season-to-season changes of the moisture component of the surface MSE, resemble those of the conditional instability in Fig. 3.7, suggesting that the annual cycle of the surface air conditional instability is largely explained by the moisture component of the surface MSE. Hence we need to explain the seasonal cycle of the moisture field across East Africa.

3.5 Atmospheric circulation

Fig. 3.11 shows the seasonal climatologies of 10 m winds from ERA-Interim Re-Analysis and their divergence. During JF (Fig. 3.11a), the Asian winter monsoon northeasterlies prevail and bring relatively cold and dry air into East Africa from the northeast. The 10 m winds are generally convergent to the east of the highlands, probably due to deceleration by surface friction as they penetrate inland. Yet most of the time these convergent winds are not able to bring precipitation because of the convectively stable atmosphere (as described in the previous section) as well as the shallowness of the convergence layer (as will be presented in the next paragraph).

During MAM (Fig. 3.11b), southeasterlies replace the northeasterlies and bring warm and moist air from the southeast, that is, from over the southwest Indian Ocean, where climatological SSTs are their highest of the year (Fig. 3.5b). The surface winds are convergent over the northeastern Horn of Africa and near the coastal land areas but

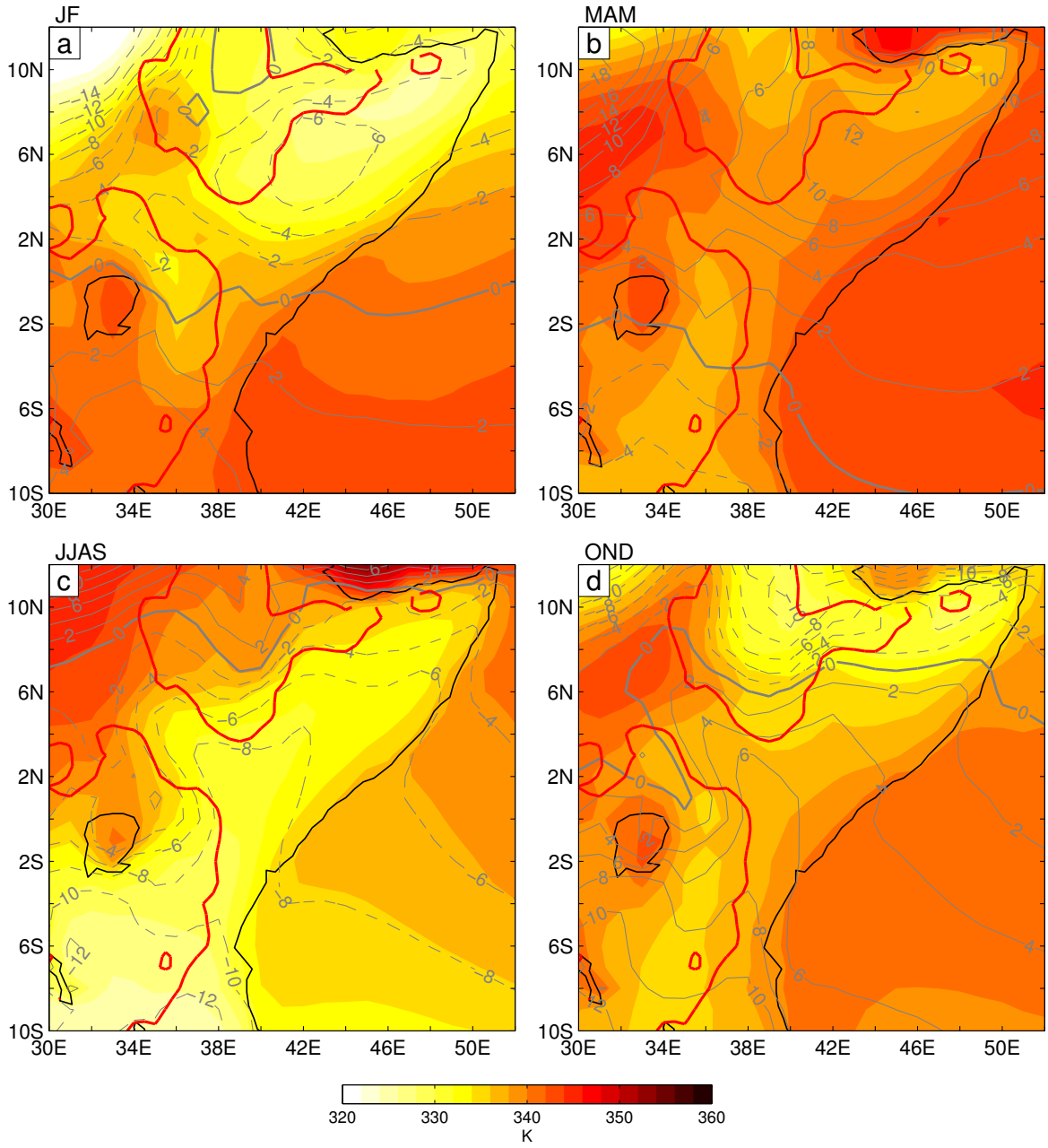

Figure 3.8: Seasonal climatologies of the surface MSE (colors) and its change from the previous season (contours) from the ERA-Interim Re-Analysis. The MSE is normalized by the heat capacity of the air at constant pressure so that it has the unit of degree Kelvin. The thick red lines are the contours of the 1000 m topographical elevation.

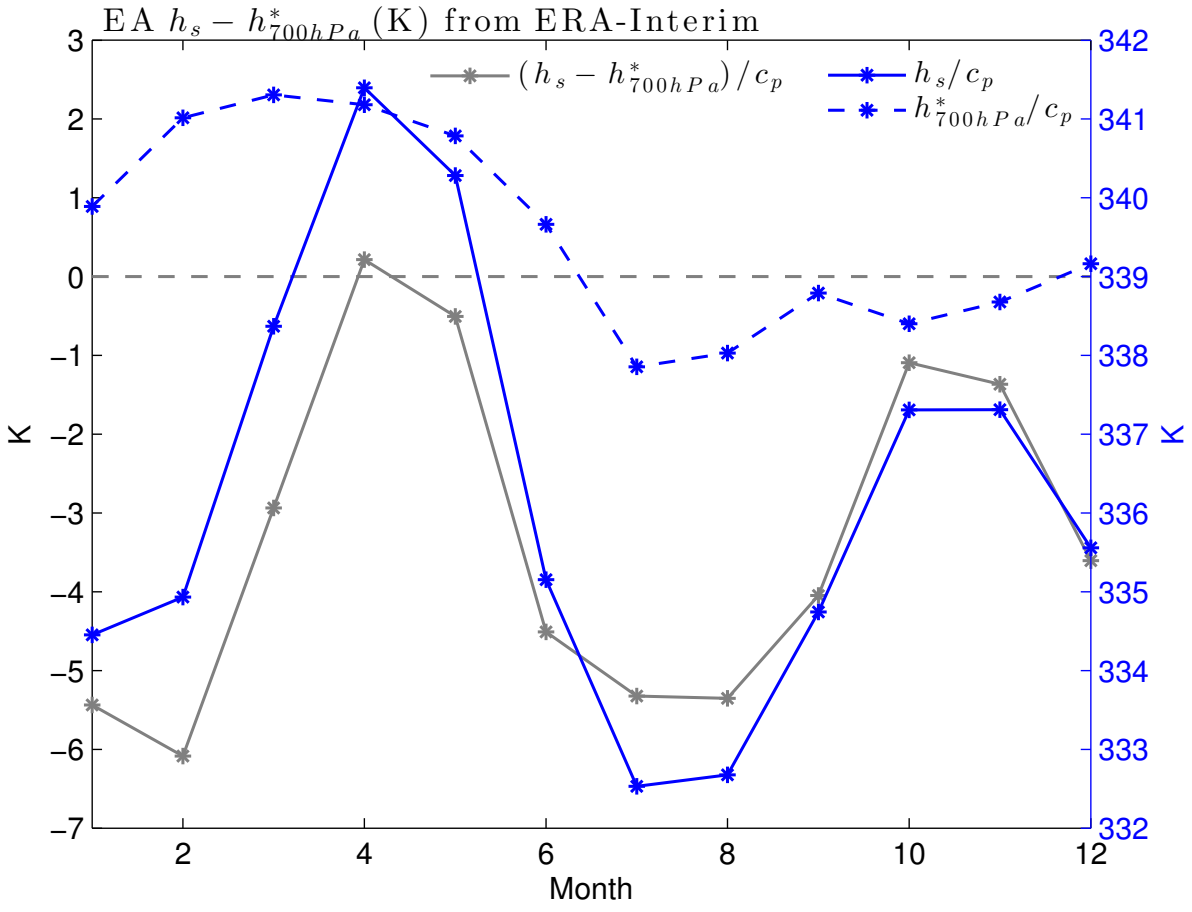

Figure 3.9: Annual cycles of surface MSE and the saturated MSE at 700 hPa pressure averaged over the shaded area shown in Fig. 3.4 .

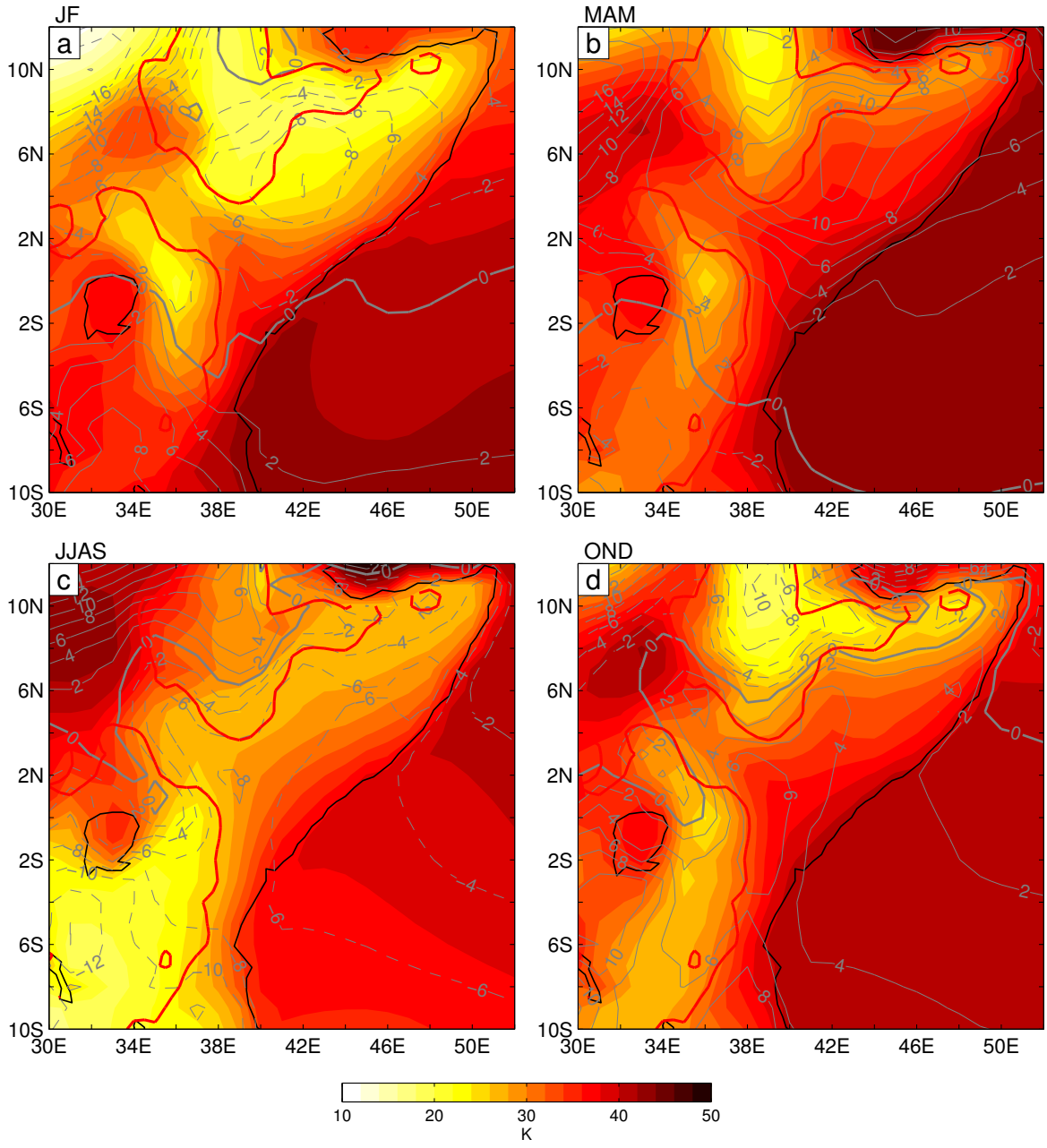

Figure 3.10: Same as Fig. 3.8 except it is only for the component of MSE associated with moisture.

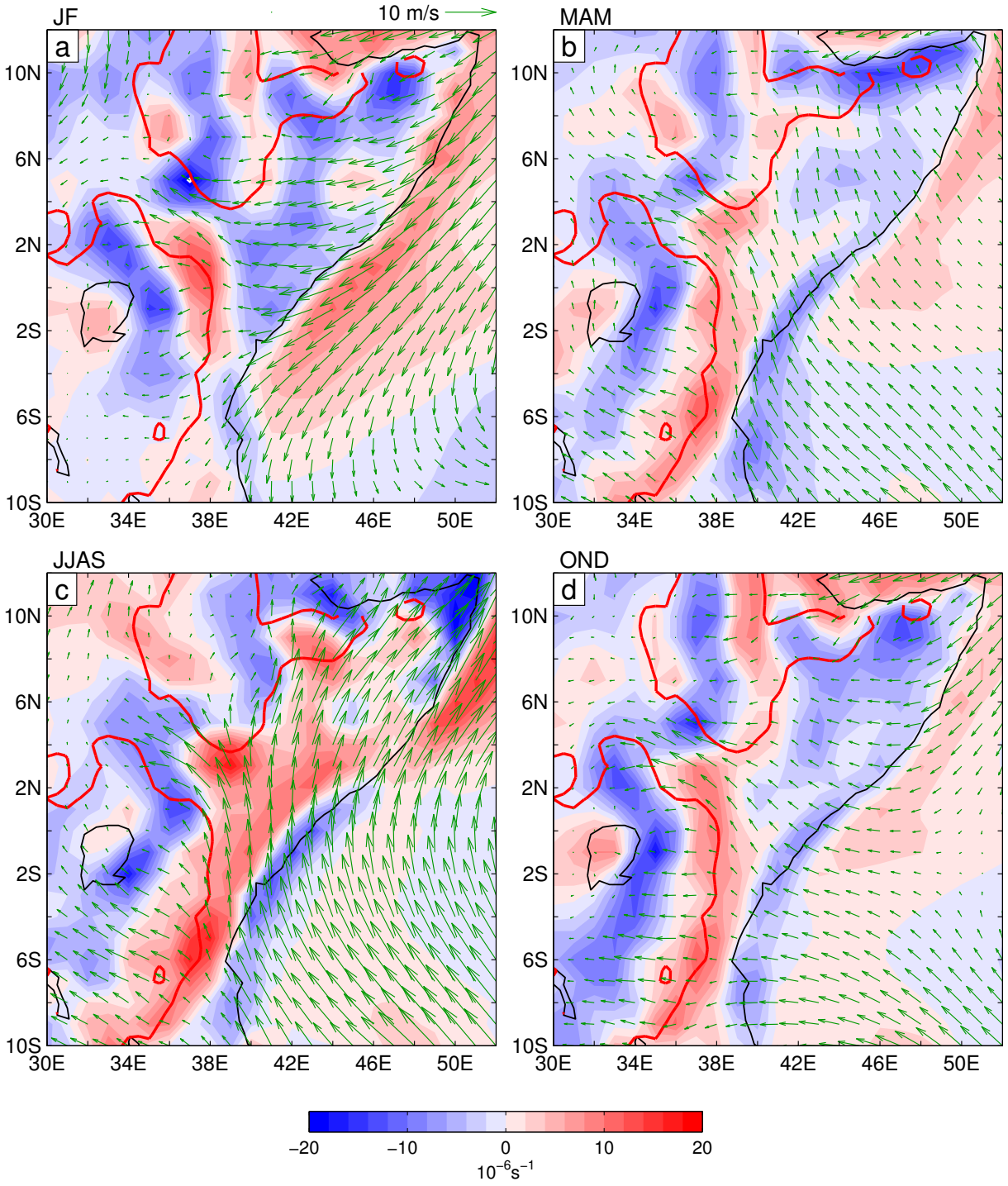

Figure 3.11: Seasonal climatologies of the 10 m wind (vectors) and its associated divergence (colors, units are 10^{-6} s^{-1}) and from ERA-Interim. The thick red lines show the smoothed 1000 m elevation contours.

become divergent near the entrance of the Turkana Channel between the northern and the southern highlands, due to the easterly acceleration when going through the entrance.

Fig. 3.11c shows the 10 m winds in JJAS. The southeasterlies intensify and turn east slightly as they travel further north, while their dynamics becomes intrinsically nonlinear (Yang et al., 2013). The low level southerlies off the equatorial East African coast, commonly known as the East African Low Level Jet (Findlater, 1969), are part of the Asian summer monsoon system. The 10 m winds accelerate as they travel across eastern land areas, resulting in divergence of the wind field. It is interesting to note that even though the along-coast component of the surface winds over eastern land areas becomes stronger in JJAS than MAM, the onshore components are comparable. However, in contrast to the long rains in MAM, land areas are extremely dry in JJAS, when SSTs off the east coast are the coldest in the annual cycle (Fig. 3.5c) and the air above is comparatively cold and dry, resulting in cool, dry and stable air advecting over East Africa.

During OND (Fig. 3.11d), the jet weakens and the magnitude of the onshore and southerly flow south of the Equator changes back to the MAM level. In general, the surface wind pattern resembles that in MAM except over the northeast, where northeasterlies or easterlies prevail in OND while southeasterlies prevail in MAM. The spatial distribution of precipitation in OND (Fig. 3.5d) is also similar to that in MAM (Fig. 3.5c) although the overall rainfall rates are slightly weaker in the short rains season (OND), possibly due to the cooler SSTs at this time.

The 850 hPa winds (Fig. 3.12) show a similar pattern to that at the surface. However, the divergence field is completely different from the surface, with year-round divergence over almost all land areas to the east of the highlands. The magnitude of the divergence of the wind field is stronger during the dry seasons of JF and JJAS and weaker during the wet seasons of MAM and OND, consistent with the precipitation annual cycle.

Fig. 3.13 shows a vertical cross-section of the annual cycle of the area-averaged divergence over East Africa. Although convergence appears near the surface, the low level atmosphere immediately above is dominated by divergence across the year, especially between 850 hPa and 700 hPa. The annual cycle also shows a bimodal distribution, with

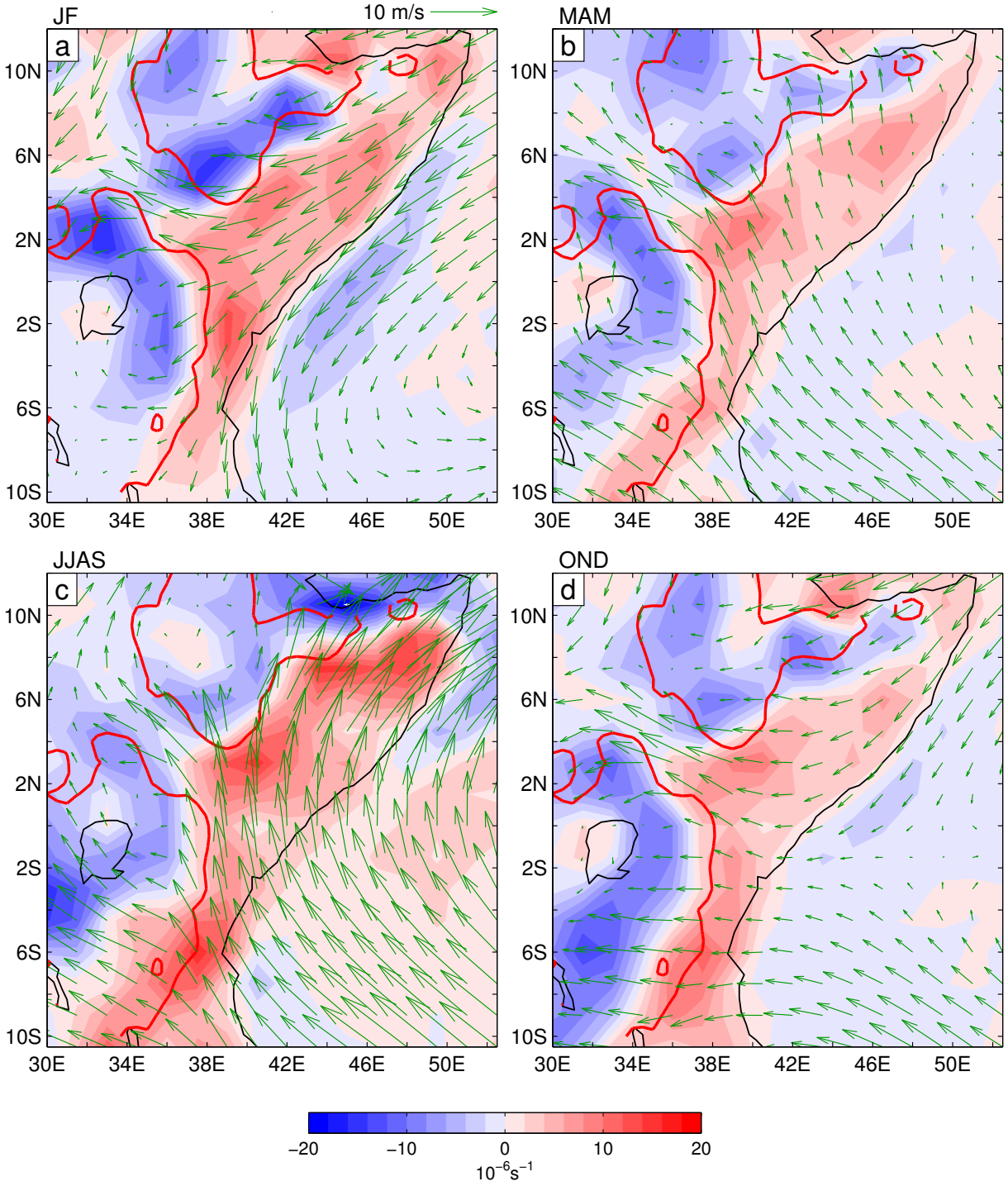

Figure 3.12: Seasonal climatologies of 850 hPa wind (vectors) and its associated divergence (colors, units are 10^{-6} s^{-1}) and from ERA-Interim. The thick red lines show the smoothed 1000 m elevation contours.

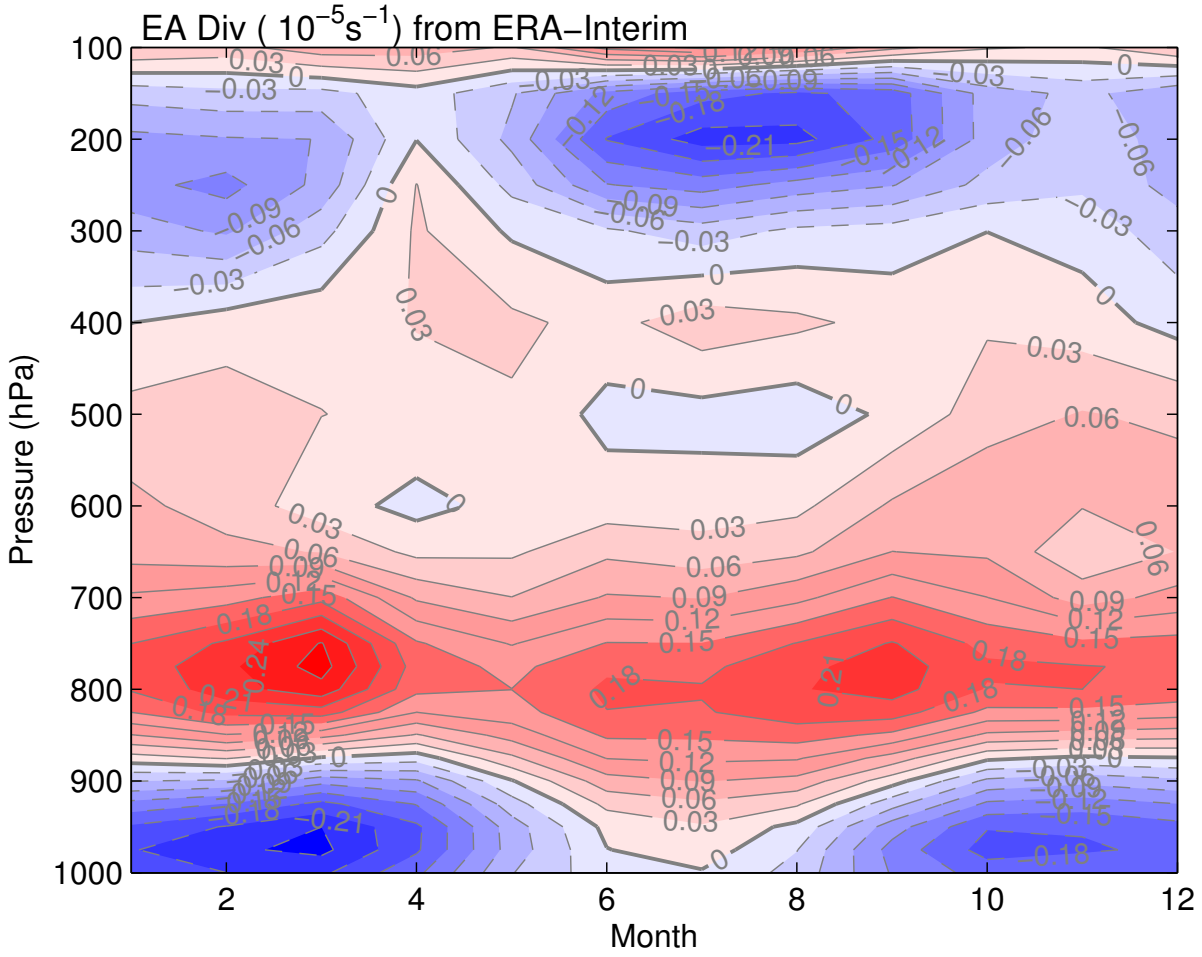

Figure 3.13: Annual cycles of wind divergence averaged over the shaded area shown in Fig. 3.4 .

maxima appearing at the beginning of the long rains and just before the short rains. Accordingly, the upper level atmosphere is dominated by convergence year-round, with maximum convergence appearing during the dry seasons and weak convergence appearing during the rainy season, in phase with the precipitation annual cycle.

Consistent with the dominance of the low level divergence and upper level convergence, the seasonal climatologies of the 500 hPa vertical pressure velocity (Fig. 3.14) are dominated by downward motions year-round, with larger values during the dry seasons and weakening during the rainy seasons. Fig. 3.15 shows the annual cycle of the area-averaged vertical pressure velocity on different pressure levels. Although the low level

atmosphere is dominated by upward motion, these do not penetrate into the middle atmosphere, where the downward motions dominate, except during the long rains season. This is consistent with the divergence shown in Fig. 3.13. The seasonal cycles of vertical motion and divergence are consistent with that of convective instability, which derives primarily from the seasonal cycle of moist static energy of low level air.

3.6 Moisture budget

The vertically integrated moisture budget was evaluated based on 6-hourly data from the ERA-Interim Reanalysis. The equation is the same as equation (13) in Seager and Henderson (2013) and is rewritten here:

$$P - E = -\frac{1}{g\rho_w}\frac{\partial}{\partial t}\int_0^{p_s} q\ dp - \frac{1}{g\rho_w}\nabla\cdot\int_0^{p_s}\vec{u}q\ dp \tag{3.1}$$

where P is precipitation rate; E is evaporation rate (here understood to include evapotranspiration); g is acceleration due to gravity; ρ_w is liquid water density; p_s is surface pressure; q is humidity; $\vec{u}$ is horizontal wind velocity. The monthly mean version of (3.1), after neglecting the local rate of change term and variations of surface pressure, is:

$$\begin{aligned}\overline{P} - \overline{E} &\approx -\frac{1}{g\rho_w}\nabla\cdot\int_0^{p_s}\overline{\vec{u}q}\ dp \\ &= -\frac{1}{g\rho_w}\nabla\cdot\int_0^{p_s}\bar{\vec{u}}\bar{q}\ dp - \frac{1}{g\rho_w}\nabla\cdot\int_0^{p_s}\overline{\vec{u}'q'}\ dp\end{aligned} \tag{3.2}$$

where the over bars and primes denote monthly mean and deviation from the monthly mean, respectively. If we compute a seasonal climatology of the above equation, the final moisture budget equation becomes:

$$\begin{aligned}\overline{\overline{P}} - \overline{\overline{E}} &\approx -\frac{1}{g\rho_w}\nabla\cdot\int_0^{p_s}\overline{\bar{\vec{u}}\bar{q}}\ dp - \frac{1}{g\rho_w}\nabla\cdot\int_0^{p_s}\overline{\overline{\vec{u}'q'}}\ dp \\ &= -\frac{1}{\rho_w}\nabla\cdot\mathrm{VIqmum} - \frac{1}{\rho_w}\nabla\cdot\mathrm{VIqpup} \\ &= -\mathrm{DVIqmum} - \mathrm{DVIqpup}\end{aligned} \tag{3.3}$$

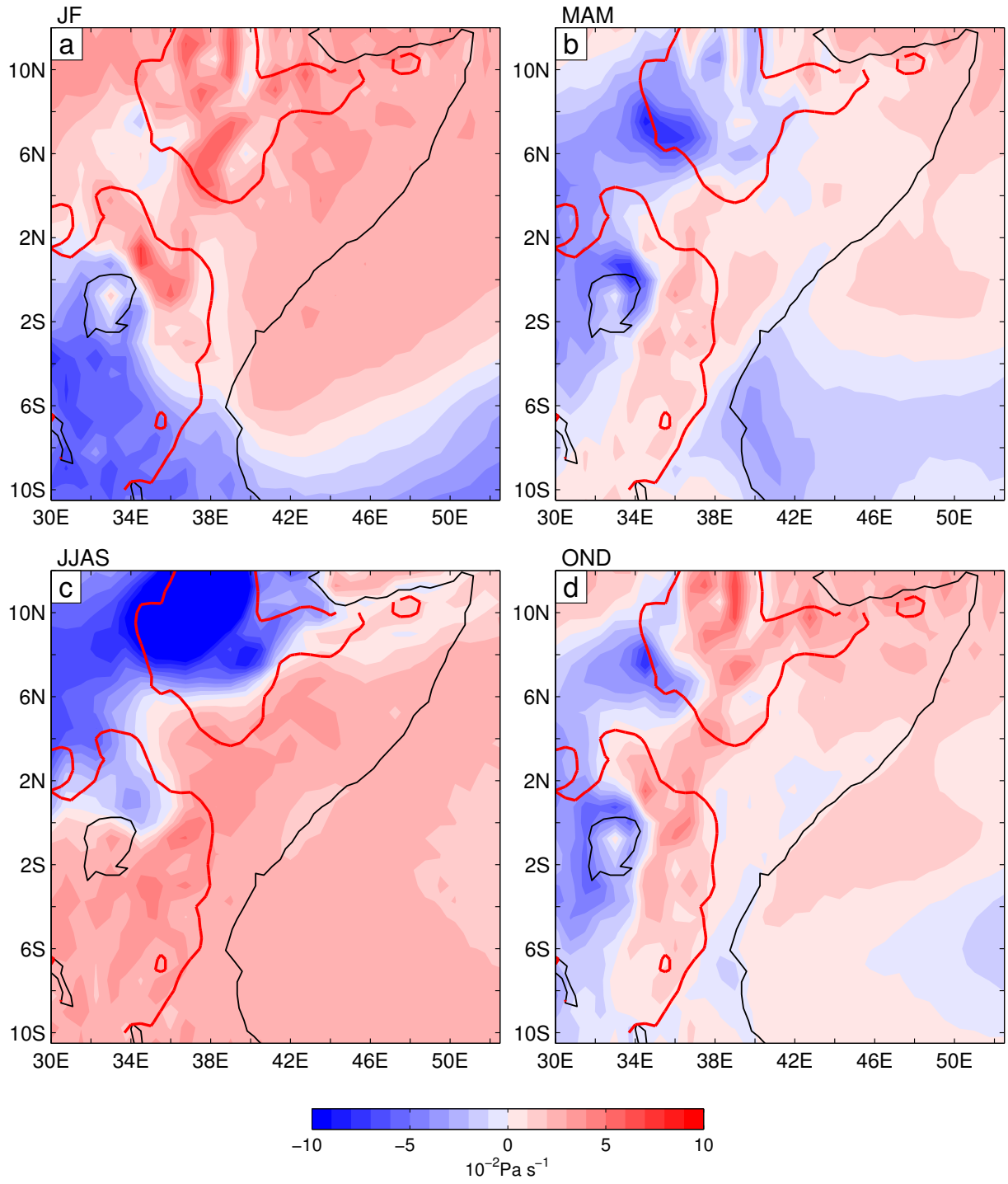

Figure 3.14: Seasonal climatologies of 500 hPa vertical pressure velocity (ω) from ERA-Interim. The thick red lines show the smoothed 1000 m elevation contours.

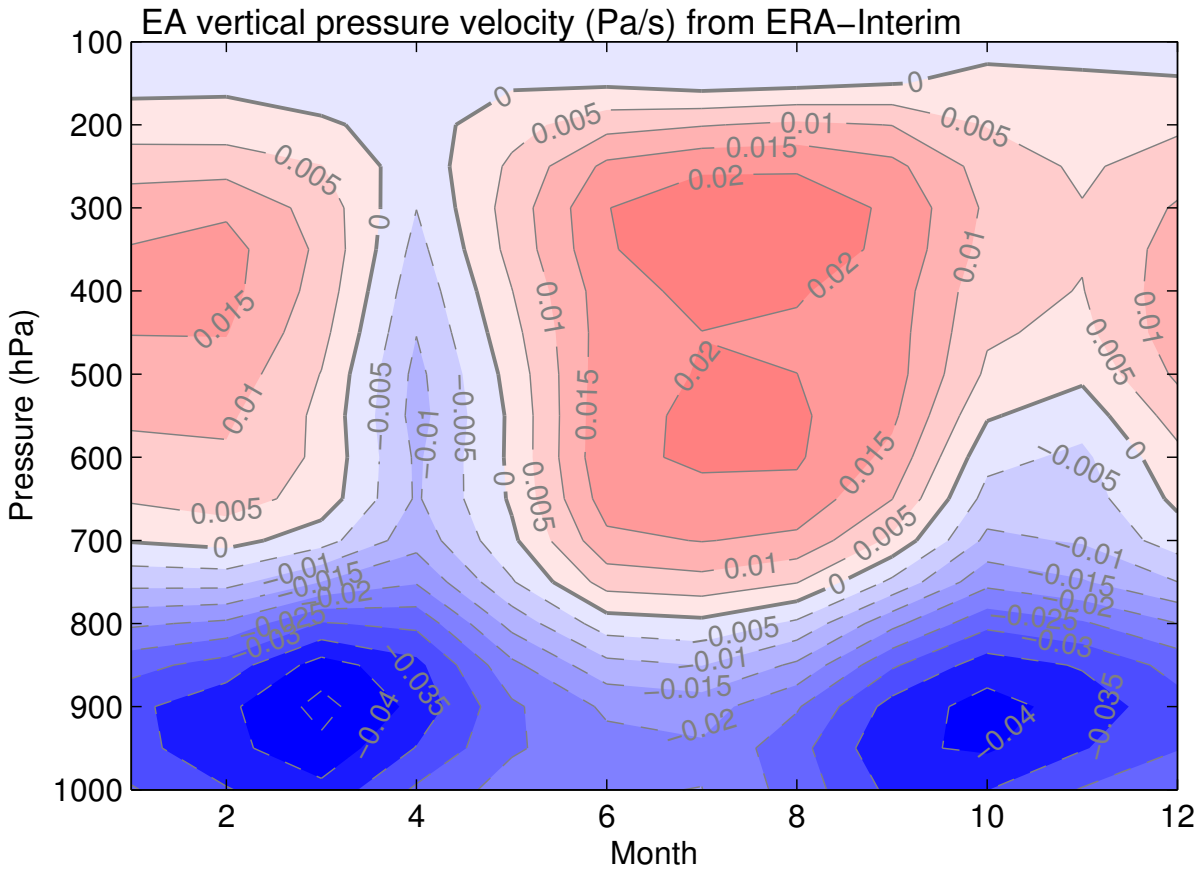

Figure 3.15: Annual cycles of vertical pressure velocity (ω) from ERA-Interim averaged over the shaded area shown in Fig. 3.4.

where

$$\begin{aligned}
\text{VIqmum} &= \frac{1}{g}\int_0^{p_s} \overline{\vec{\bar{u}}\bar{q}}\, dp \\
\text{VIqpup} &= \frac{1}{g}\int_0^{p_s} \overline{\vec{u'q'}}\, dp \\
\text{DVIqmum} &= \frac{1}{g\rho_w}\nabla\cdot\int_0^{p_s} \overline{\vec{\bar{u}}\bar{q}}\, dp \\
\text{DVIqpup} &= \frac{1}{g\rho_w}\nabla\cdot\int_0^{p_s} \overline{\vec{u'q'}}\, dp
\end{aligned}$$

and the top bar denotes seasonal climatology. Here VIqmum and VIqpup represent the seasonal climatologies of the vertically integrated moisture flux due to monthly mean circulation and sub-monthly eddies, respectively, with DVIqmum and DVIqpup the corresponding divergences. In these names, "qm" and "um" denote monthly mean specific humidity and circulation, while "qp" and "up" represent deviations from their monthly means. These terms were evaluated in the ERA-Interim Reanalysis as in Seager and Henderson (2013) and the notations and naming conventions are also briefly described in `http://kage.ldeo.columbia.edu/naomi/notation.pdf`.

Fig. 3.16 shows the seasonal climatologies of VIqmum (VIqpup has much smaller magnitude than VIqmum and its map is not shown here). These fluxes in general follow the pattern of the low level circulation (Fig. 3.12) as most of the moisture in the atmosphere is concentrated within the bottom layer. The estimated net moisture transport from the Indian Ocean through the East African coast noted in Fig. 3.16 (sum of the three terms) is much greater during the rainy seasons than the dry seasons, consistent with the precipitation annual cycle in this region. The net transport is low in JF (Fig. 3.16a) because the moisture flux is almost parallel to the coast in this season while during summer strong moisture flux out into the Indian Ocean across the northeastern coast is responsible for the lowest net moisture import into East Africa (Fig. 3.16c).

We also assess the relative importance of the circulation annual cycle and humidity annual cycle in the annual cycle of total moisture transport from the Indian Ocean into East Africa by estimating the moisture transport with four different combinations of q u, and v: 1) monthly mean q, u, and v; 2) monthly mean u and v and annual mean q

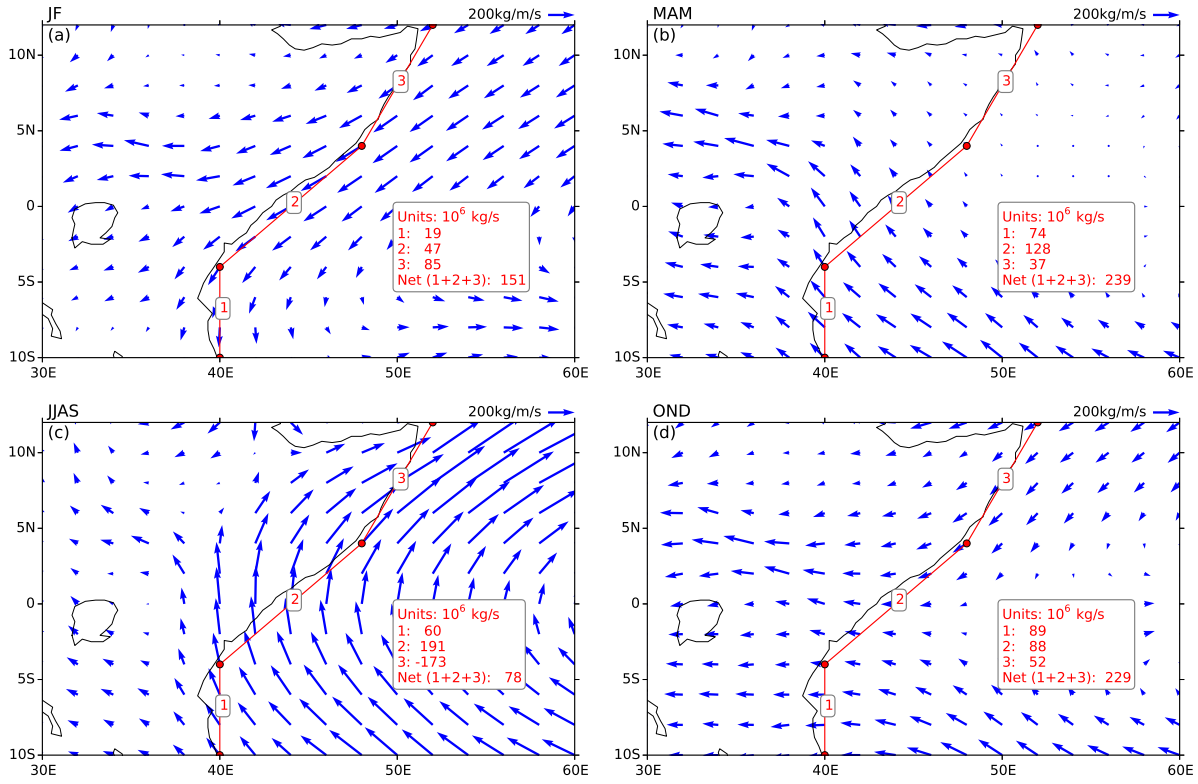

Figure 3.16: Seasonal climatologies of the vertically integrated moisture flux of the monthly circulation and humidity from ERA-Interim. The stepwise numbered red lines approximate the coast and the moisture transports (westward/eastward transports are positive/negative) through these lines are listed in the box to the right.

(to assess the importance of the circulation annual cycle); 3) monthly mean q and annual mean u and v (to estimate the importance of the humidity annual cycle); 4) annual mean q, u and v (the base component without an annual cycle). With the last combination estimated as 190 $\times 10^6$ kg s^{-1}, the results of the first three combinations, after the base component is removed, are shown in Fig. 3.17. The moisture transport estimation based on monthly mean q, u, and v (red bars) is consistent with the precipitation annual cycle over East Africa as shown before, with higher values in rainy seasons than in dry seasons. Meanwhile, both the component associated with the circulation annual cycle (green bars) and the component associated with the humidity annual cycle (blue bars) follow the total moisture transport but the magnitude of the former is at least two times larger than that of the latter. This implies that the circulation annual cycle is more important than the humidity annual cycle in the annual cycle of moisture transport from Indian Ocean into East Africa.

Fig. 3.18 shows the annual cycles of the different terms in the moisture budget equation averaged over East Africa. The precipitation from the ERA-Interim Reanalysis (the green dashed line) is able to capture the annual cycle of the GPCC data (the green solid line) although it also has the problem of overestimating the magnitude of the short rains. Evaporation has comparable magnitude to the precipitation but much weaker season-to-season variations. The divergence of the vertically integrated moisture flux can be decomposed into the component associated with the monthly mean flow and moisture (DVIqmum) and the component due to sub-monthly eddies (DVIqpup). There is mean flow moisture divergence, indicating atmospheric exportation of moisture in all months except in April and October. The eddy component, DVIqpup, is much weaker and out of phase with the mean flow component. It should be noted here that the annual mean E is much greater than the annual mean precipitation either from GPCC or from ERA-Interim, which was also found in previous studies and usually attributed to extensions of oceanic $P - E$ patterns near coasts due to models' low resolution (Dai and Trenberth, 2002). As our focus here is primarily on the annual cycle instead of the annual mean climatology, this is not a big problem. The sum of the three components (E, the mean

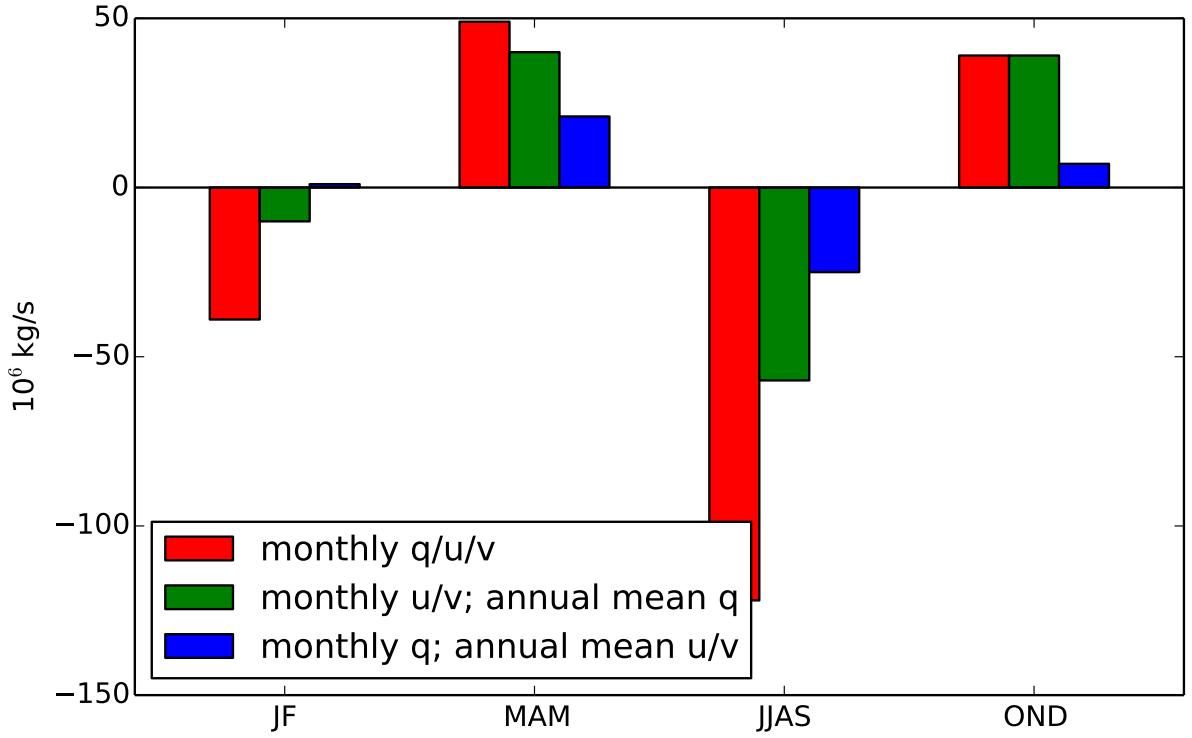

Figure 3.17: Vertically integrated moisture transports from the Indian Ocean into East Africa through the coast between 10^0S and 12^0N in the four seasons (the annual mean q, u and v component, which is estimated as 190 $\times 10^6$ kg s^{-1}, has been removed to emphasize the annual cycle). Different colors show results from different cases with red bars using monthly mean q, u and v, green bars using annual mean q and monthly mean u and v, and blue bars using annual mean u and v and monthly mean q.

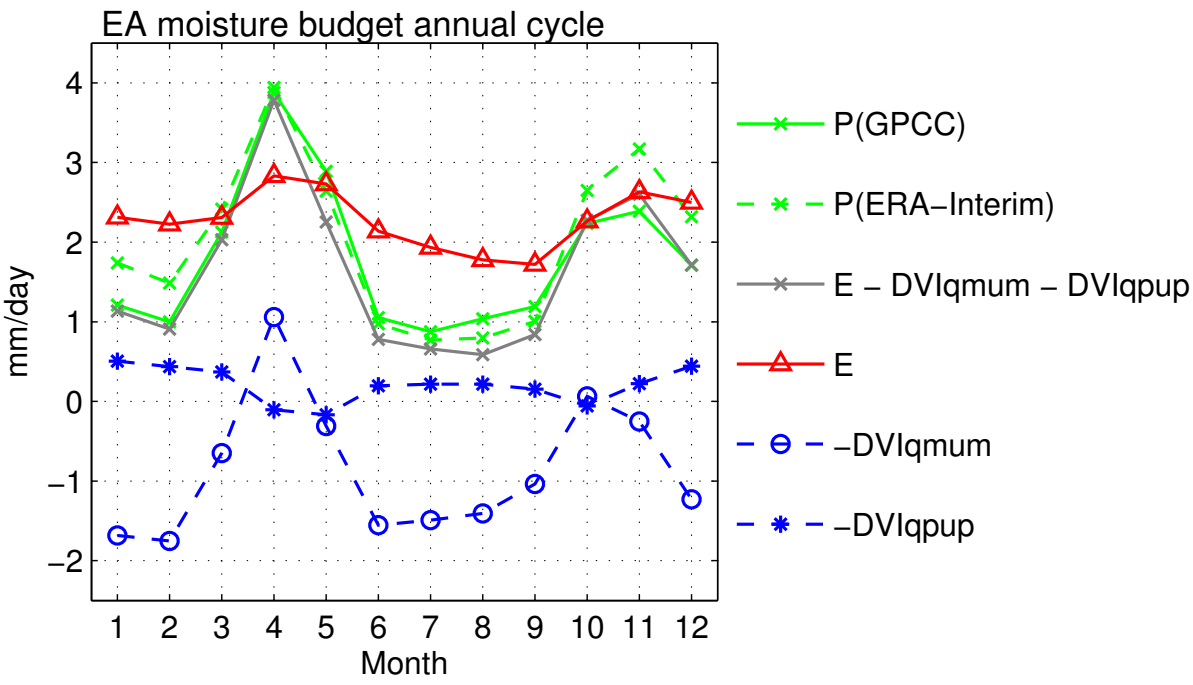

Figure 3.18: Annual cycles of the moisture budget terms averaged over the areas shown in Fig. 3.4 from ERA-Interim.

and transient flow moisture convergence, the gray line) approximates the precipitation annual cycle very well, especially for the GPCC data (correlation coefficient 0.94). These results demonstrate that the moisture budget analysis does a good job in East Africa in terms of annual cycle. Fig. 3.18 also shows that the two seasonal precipitation peaks are driven by the two periods of mean flow moisture convergence, which are themselves driven by the two peaks in low level mean flow mass convergence. The seasonal cycle of the area mean moisture convergence is in turn related to that of the moisture transport across the East Africa coast.

3.7 Conclusion and discussion

Recent studies have demonstrated that coupled models used in CMIP3/5 generally misrepresent the East African precipitation annual cycle by overestimating the short rains (rainfall in OND) (Yang et al., 2014b), which casts doubt on the reliability of projections of future East African precipitation (Waithaka et al., 2013). To understand the discrep-

ancy between the model simulations and observations in this regard, a natural first step is to better understand the observed East African precipitation annual cycle. By using ERA-Interim reanalysis data, we have analyzed the seasonal climatologies and annual cycles of atmospheric thermal condition, circulation and moisture budget, which are closely related to the East African precipitation annual cycle. The following conclusions have been reached:

- The off-coast SSTs (i.e. the western Indian Ocean SSTs) annual cycle is closely related to that for East African precipitation. These SSTs are higher during the rainy seasons than in the dry seasons and are highest during the long rains.

- The atmosphere is generally conditionally stable throughout the year but the degree of instability measured as the difference between surface MSE and the saturated MSE at 700 hPa follows the precipitation annual cycle, i.e. less stable during the rainy seasons and more stable during the dry seasons and least stable during the long rains season.

- The annual cycle of the atmospheric stability is dominated by the surface MSE, and, in particular, by the annual cycle of surface humidity.

- Although convergence prevails very near the surface, divergence in the low level troposphere and convergence in the upper level troposphere dominate year-round.

- Consistent with the divergence field, the vertical velocity is predominantly downward in the middle troposphere and the magnitude is stronger in dry seasons than in rainy seasons.

- The vertically integrated moisture flux is dominated by the monthly mean component with the sub-monthly eddy component much weaker. The total cross-coast moisture transport from the Indian Ocean into East Africa follows the precipitation annual cycle in this region. The annual cycle of this transport is primarily due to the circulation annual cycle and the role of the humidity annual cycle is secondary but modifying .

- The area-averaged mean flow moisture convergence follows the East African precipitation annual cycle and, when combined with the transient eddy convergence and evaporation (E), approximates the observed East African precipitation annual cycle very well.

The region of East Africa, while in the deep tropics and surrounded by the world's major monsoons (the south Asian monsoon, the west African monsoon and the Australian monsoon), does not exhibit either a wet climate in terms of annual mean precipitation or a monsoonal climate in terms of precipitation annual cycle. Instead, East Africa is dominated by a semi-arid/arid climate with a bimodal annual cycle of precipitation. Traditionally, the aridity was considered to be associated with the dominant low level divergence (Trewartha, 1961), which in turn was assumed to be caused by a wind stress contrast between land and ocean (Nicholson, 1996). However, the wind stress mechanism would be greatest near the surface and along immediate coastal areas. Our results (Fig. 3.11) show that the surface winds are mostly convergent along the east coast while the 850 hPa winds are predominantly divergent over much of the region to the east of the highlands (Fig. 3.12). This is in contrast to the wind stress mechanism.

So what mechanism might be responsible for the semi-arid/arid climate in East Africa? Unlike extra-tropical precipitation, which is mainly driven by synoptic scale baroclinic eddies (Lee and Held, 1993; Pierrehumbert and Swanson, 1995; Chang et al., 2002; Yang et al., 2007), tropical rainfall mostly arises from moist convection, in which the subcloud MSE plays a key role in the framework of quasi-equilibrium (QE, Emanuel et al. (1994)). The QE framework has been applied to study the mechanisms that limit the poleward extent of summer monsoons (Chou and Neelin, 2001, 2003), the location of monsoons (Privé and Plumb, 2007a,b), and the role of orography in monsoons (Boos and Kuang, 2010). An important and relevant idea from these studies is that ventilation (which was defined as the import of low MSE air by advection from cooler oceans) depresses local convection and precipitation by decreasing the subcloud MSE. It should be noted that the ventilation mechanism in these studies is generally applied only in the subtropical margins of convection zones because of drier and cooler air to the poleward side. However, in the

case of East Africa, there are strong low-level cross-equatorial monsoonal winds during the dry seasons, especially in summer, which can bring much lower MSE air from the winter hemisphere into East Africa and stabilize the atmosphere. The north-south orientated highlands act to block the import of high MSE air from the west as well as leading to the formation of the East African low-level jet (Findlater, 1969). Indeed, numerical experiments without topography (Fig. 1a in Chou and Neelin (2003)) demonstrated that East Africa is much wetter during the boreal summer season due to the fact that the low-level jet in observations is now replaced by westerlies in the simulation, which bring high MSE air from the interior of Africa to the west. Furthermore, SSTs near the coast are generally cool compared to values further offshore (Fig. 3.5) and a cool west-warm east SST gradient off the coast exists year-round. Therefore, even in the rainy seasons when the air is imported from the western tropical Indian Ocean by the weak onshore winds, it is still difficult for East Africa to develop as high subcloud MSE as in regions with high coastal SSTs. Since the saturated MSE above the boundary layer is near uniform across the tropics (Sobel et al., 2001), and influenced by the warmest of tropical regions, low subcloud MSE in East Africa ensures overwhelming stable conditions to moist convection.

The bimodal annual cycle is therefore proposed to be the result of the annual cycle of monsoonal winds combining with the annual cycle of the Indian Ocean SST. During boreal winter precipitation over East Africa is suppressed due to advection of low-MSE air from the cold northern Indian Ocean. During boreal summer the precipitation is suppressed due to even stronger advection from the cool Indian Ocean with the cool Indian Ocean resulting from both winds coming from the winter hemisphere and the coastal upwelling associated with the Somali Jet. During the two rainy seasons, the low-level winds are much weaker and thus have less impact on the surface air MSE over East Africa. Moreover, the SSTs off the coast are higher during the two rainy seasons and are the highest of the year during the long rains season. These are the reasons, we propose, why there is more precipitation during the two rainy seasons and the long rains are stronger than the short rains. For all seasons, the off-coast SSTs are still lower than that of the eastern interior of the Indian Ocean, i.e. there is a west-east SST gradient over the Indian Ocean within

the East African latitudes. The cooler SSTs off the East African coast, when combined with the year-round onshore winds, prevent land areas over East Africa from developing high subcloud MSE and therefore suppress the overall precipitation in this region. This would explain the largely semi-arid/arid climate over East Africa.

Recent studies demonstrated that simulations from coupled climate models tend to have a west-east SST gradient that is too weak, i.e. simulated SST over the western Indian Ocean (including the SST nearby the East African coast) is higher than observed while the eastern Indian Ocean SST is close to or lower than observed. This is especially so during the boreal late autumn/early winter months (Conway et al., 2007; Han et al., 2012; Liu et al., 2013; Cai and Cowan, 2013). This might be one of the reasons why coupled models generally have a tendency to overestimate the short rains. We will next look at SSTs as well as circulation patterns in those CMIP coupled models that are crucial in the East African subcloud MSE development and moisture flux in order to better understand the overestimation of the short rains in coupled models and the consequent misrepresentation of the East African annual cycle of precipitation. This understanding should lead to improvements in the model representation which could further lead to greater confidence in model projections of future East African climate.

CHAPTER 4

East African Rainfall Annual Cycle Bias Induced by Coupled CMIP5 Models *

4.1 Introduction

East Africa has been undergoing increased frequency and intensity of droughts in recent decades, raising the question of whether the drying trend will continue in a warmer future climate as forced by anthropogenic emissions of greenhouse gases (GHGs). Although some studies proposed that the recent drying trend can be attributed to SST anomalies over the Indian Ocean induced by anthropogenic forcing (Funk et al., 2008; Williams and Funk, 2011), and therefore suggested the potential extension of the current drying trend into the near future, there is a strong consensus in model projections from the Intergovernmental Panel on Climate Change (IPCC) Fourth Assessment Report (AR4) and the more recent Coupled Model Intercomparison Project Phase 5 (CMIP5, Taylor et al. (2012)) that precipitation over East Africa will increase (Shongwe et al., 2011; Otieno and Anyah, 2013), implying that the current dry conditions will be, at least partly, ameliorated in the near future.

The reliability of these optimistic projections on East African hydroclimate and their suitability to serve as the foundation for the development community, however, depend on the performance of the models in reproducing the East African precipitation in the past. By examining the performance of both SST-forced (AMIP-style) models and the coupled models used in the CMIP5 historical experiment (CMIP-style) in simulating the East African long rains, Yang et al. (2014b) showed that, while some of the SST-forced models are able to capture the observed decadal variability of the long rains, the coupled models, which are used for the 21st century climate projections, generally fail to capture the correct long rains-SST relationship. Moreover, the coupled models misrepresent the East African

* The work of this chapter is currently in preparation for submission in the near future.

precipitation annual cycle by overestimating rainfall during October–December (OND) and overestimating the rainfall during March–May (MAM), which has been also reported for the CMIP3 coupled models (Anyah and Qiu, 2012). The cause of the precipitation annual cycle bias from the CMIP5 coupled models and its implications for the projections from these coupled models are still not clear.

Previous studies have revealed that there are some global scale or tropical scale biases in the coupled models of CMIP3 and CMIP5 (Cai and Cowan, 2013; Li and Xie, 2014; Wang et al., 2014), including the excessive equatorial Pacific cold tongue and double Intertropical Convergence Zone (ITCZ) (Li and Xie, 2014), weak Atlantic Meridional Overturning Circulation (AMOC) (Wang et al., 2014), and an unrealistic mean thermocline slope tilting upward toward the eastern Indian Ocean (Cai and Cowan, 2013). These larger scale biases in the coupled models might potentially affect the precipitation simulations over East Africa and the linkage between the two needs to be explored. In explaining the East African rainfall annual cycle, Yang et al. (2014a) proposed that the annual cycle is modulated by the near surface moist static energy (MSE), which in turn is controlled by the off-coast sea surface temperature (SSTs) as well as the low level atmospheric circulation. Here we examine whether the MSE explanation framework can be applied to understand the rainfall bias over East Africa from the CMIP5 coupled models.

In this study, we will analyze the coupled model induced bias of the East African rainfall annual cycle by comparing the historical run and AMIP run for each model, with particular emphasis on the MRI-CGCM3 model, which best simulates the annual cycle in AMIP run but has a coupled model bias typical of the miltimodel mean. Section 4.2 describes the data and models used in the study as well as some special treatment of calculations; Section 4.3 show the historical minus AMIP bias from multimodel statistics and individual models; detailed analysis of the MRI-CGCM3 is in Sections 4.4; the main conclusions of the paper and associated discussion are provided in Section 4.5.

4.2 Data, models and methods

For observed precipitation, we use: version 6 of Global Precipitation Climatology Centre (GPCC) monthly precipitation (Rudolf et al., 2010), which is a gauge-based, 0.5^0 longitude $\times$ 0.5^0 latitude gridded global land surface dataset for the period 1901–2010; version TS 3.1 of monthly precipitation over global land areas from the Climatic Research Unit at the University of East Anglia (CRU hereafter, Mitchell and Jones 2005) covering from 1979 to 2009; version 2.2 of the Global Precipitation Climatology Project (GPCP) monthly precipitation dataset from 1979 to 2010 (Huffman et al., 2009), which combines gauge observations and satellite data into $2.5^0 \times 2.5^0$ global grids; Climate Prediction Center (CPC) Merged Analysis of Precipitation (CMAP) (Xie and Arkin, 1997), which is also monthly satellite and gauge data and covering from 1979 to 2011; version 7 of Tropical Rainfall Measuring Mission (TRMM) daily precipitation (Huffman et al., 2007) covering from 1998 to 2014; precipitation from the European Centre for Medium-Range Weather Forecasts (ECMWF) Interim Re-Analysis (ERA-Interim) (Dee et al., 2011), which covers the post-1979 period and is the latest of the ECMWF reanalyses

In this study, twenty one of the CMIP5 models that have precipitation available for both historical and AMIP runs are used. Their names are listed in Fig. 4.3 and Fig. 4.4. Only one run is chosen for each model to calculate the multimodel mean and other statistics across these models. As most models cover only the period before 2005 for the historical runs, the base period we choose to calculate climatology for both observations and models is 1979–2005 except that for the TRMM daily precipitation data 1998–2005 is used instead. In this study, we focus on the land areas of East Africa that show a bimodal rainfall annual cycle and an arid/semi-arid annual mean climatology by applying the following criteria: 1) precipitation rate in March–May greater than January–Feburay and June–September; 2) annual mean precipitation rate less than 2 mm day^{-1}. The resulting areas over East Africa are shown as gray grids in the mini panel of Fig. 4.1. Area average over East Africa in this study is only applied to these grids unless otherwise stated.

4.3 CMIP5 multimodel statistics

Fig. 4.1 shows the East African rainfall annual cycles from different datasets of observations, the ERA-Interim Re-Analysis and AMIP runs of the 21 CMIP5 models. The observed annual cycles are close to each other, no matter whether the observation is based on gauge (GPCC and CRU) or satellite (TRMM) or their combination (CMAP and GPCP), establishing a solid reliability for the observed rainfall annual cycle over East Africa. The characteristic bimodal annual cycle is apparent from the observations, with the major rainy season during March–May (MAM) and the second rainy season during October–December (OND). Precipitation from the ERA-Interim Re-Analysis generally follows the observed annual cycle except for OND where the reanalysis can be 0.5 mm day^{-1} greater than the observed. This is probably due to the fact that a reanalysis dataset is influenced by both the assimilated observations and by the model. As a result, reanalysis can potentially share some similar bias to GCMs especially for precipitation. Rainfall annual cycles from the AMIP runs show some degree of spread among different models but the multimodel mean (the blue line) or their median (red horizontal lines in the boxes) does reproduce the bimodal feature. However, the multimodel mean generally overestimates the rainfall in all months except April and May, particularly in the second rainy season (OND) such that rainfall in this season exceeds that in the major rainy season (MAM). This type of bias in AMIP runs might arise from the AGCM's excess response of precipitation to the SST gradient over the western Indian Ocean as found in previous work (Bollasina and Ming, 2013) and will not be addressed here. Instead, we will focus on the bias induced by the atmosphere-ocean coupling by comparing CMIP5 historical runs to the AMIP runs.

Fig. 4.2 shows the change of East African rainfall annual cycles for historical minus AMIP from the 21 CMIP5 models. The historical minus AMIP rainfalls are largely negative from January to May. Moreover, the historical run is drier than the AMIP run for all models during Feburary–April, with the largest multimodel mean discrepancy (>1 mm day^{-1}) occurring in April. During the summer season of June–September (JJAS), the historical minus AMIP rainfalls spread around zero and only the September multimodel

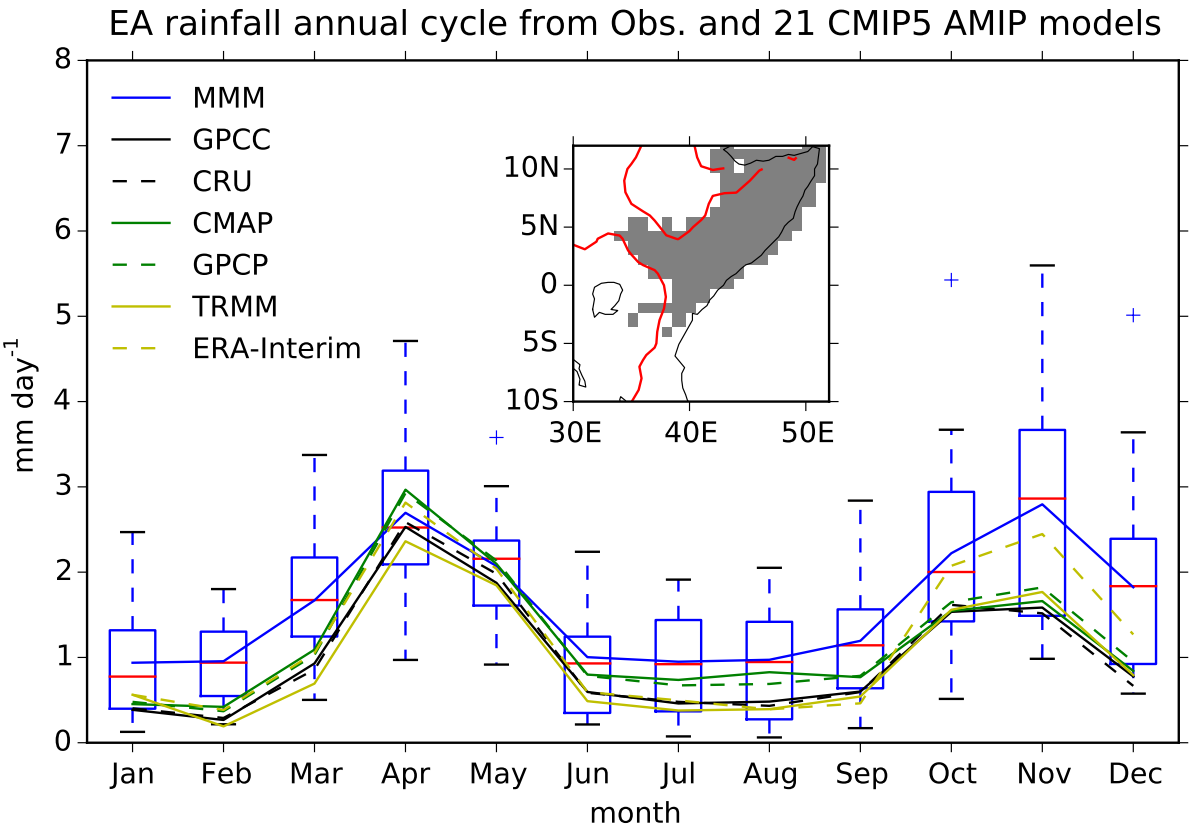

Figure 4.1: East African rainfall annual cycles from observations, the ERA-Interim Re-Analysis and AMIP runs of 21 CMIP5 models, averaged over the gray shaded grids as shown in the mini panel, where the red lines are the 1 km elevation contours. Box plots show the statistics across the 21 models and the blue line is the multimodel mean (MMM).

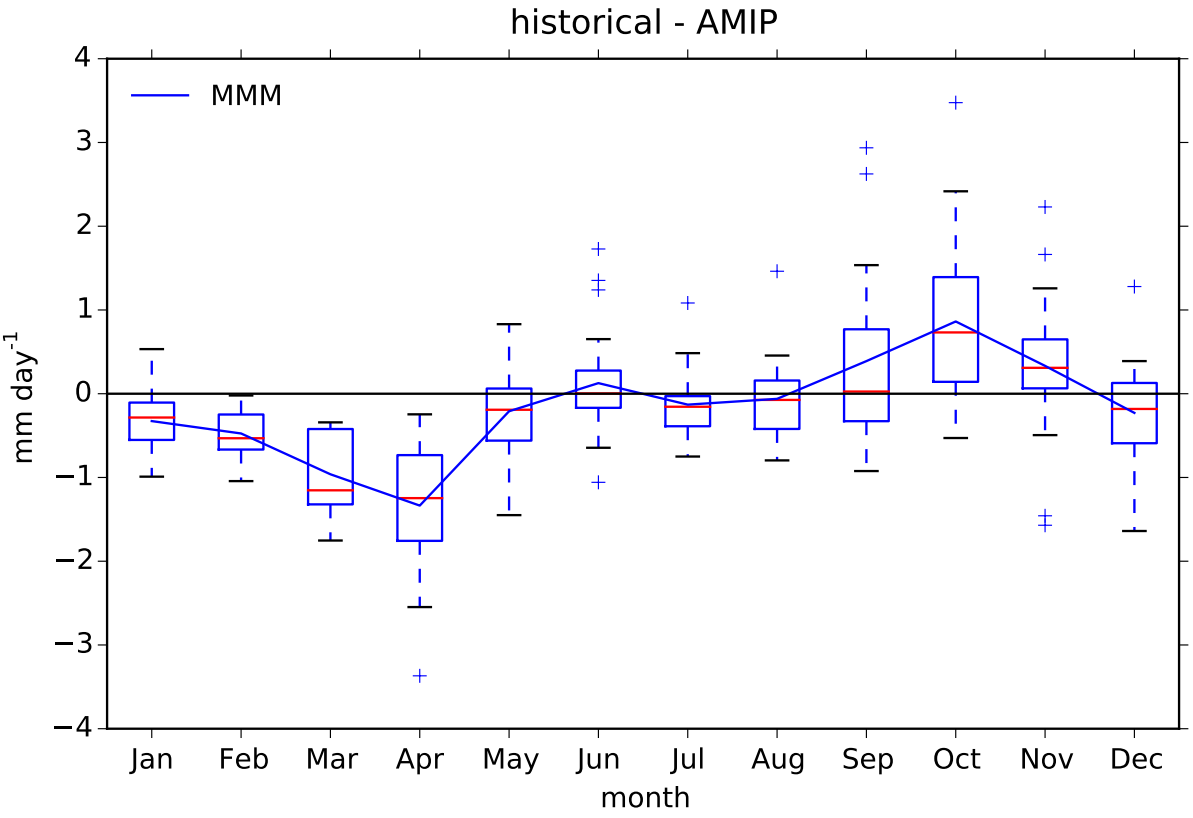

Figure 4.2: East African historical-minus-AMIP rainfall annual cycles from the CMIP5 21 models (box plots). The blue line is the multimodel mean (MMM).

mean is greater than 0.5 mm day^{-1}. The multimodel mean of historical minus AMIP rainfalls peaks at around 1 mm day^{-1} in the first month of the second rainy season (October), reduces during the following two months and falls to a slight negative value in December. Overall, the historical runs are wetter than the AMIP runs during the second rainy season (OND), an opposite sign to that during the major rainy season (MAM).

Fig. 4.3 shows the East African rainfall annual cycles of CMIP5 individual models for the AMIP and historical runs as compared to the GPCC result. For the AMIP runs (blue lines), some models are highly correlated with the GPCC (e.g. MRI-CGCM3, IPSL-CM5A-LR, FGOALS-g2 and CSIRO-Mk3-6-0) while some models are not (e.g. inmcm4, BNU-ESM and NorESM1-M). The correlation coefficients with the GPCC, as well as the root mean squared errors compared to the GPCC, of all the CMIP5 model AMIP

runs are shown in the scatter plot of Fig. 4.4. For most models, the historical runs are wetter than the AMIP runs for the overall OND while they are drier for the overall MAM especially for April. Of all these 21 models, MRI-CGCM3 is of particular interest in that its AMIP run reproduces the GPCC annual cycle very well but when coupled, it dramatically overestimates the OND rainfall and underestimates the MAM rainfall, similar to the coupled multimodel mean bias. Therefore, MRI-CGCM3 serves as an ideal model to study the bias induced by turning from SST-forced GCMs into atmosphere-ocean coupled GCMs.

4.4 Results from MRI-CGCM3

Fig. 4.5 shows the historical minus AMIP monthly climatology rainfall of MRI-CGCM3 over East Africa and surrounding areas. It is largely negative over East Africa from January to May and the absolute value is greatest in April, consistent with the multimodel mean result in Fig. 4.2. It is noted that the January–May dry anomalies over East Africa are accompanied by a large scale north-south dry-wet pattern over the Indian Ocean, suggesting that the dry anomalies might be associated with some large scale dynamics. Starting from June, a strong wet anomaly develops over the western Indian Ocean, abruptly shifting the anomalies over the Indian Ocean into a new west-east wet-dry pattern and keeping this new pattern until the end of the year. This large scale shift of the historical minus AMIP anomaly has important impact over East Africa, turning the previous negative anomalies into positive values from June to November. The positive anomalies over East Africa peak in September and October and turn slightly negative in December, also consistent with the multimodel mean result in Fig. 4.2.

4.4.1 Convective instatility and MSE

In order to understand the historical minus AMIP monthly climatology rainfall change of MRI-CGCM3, we calculate the convective instability (CI) as measured by near surface moist static energy minus 700 hPa saturated moist static energy (i.e. $h_s - h^*_{700hPa}$). The historical minus AMIP monthly climatology CIs of the model are shown in Fig. 4.6. The CI anomalies generally agree well with rainfall in Fig. 4.5. There is also a large scale

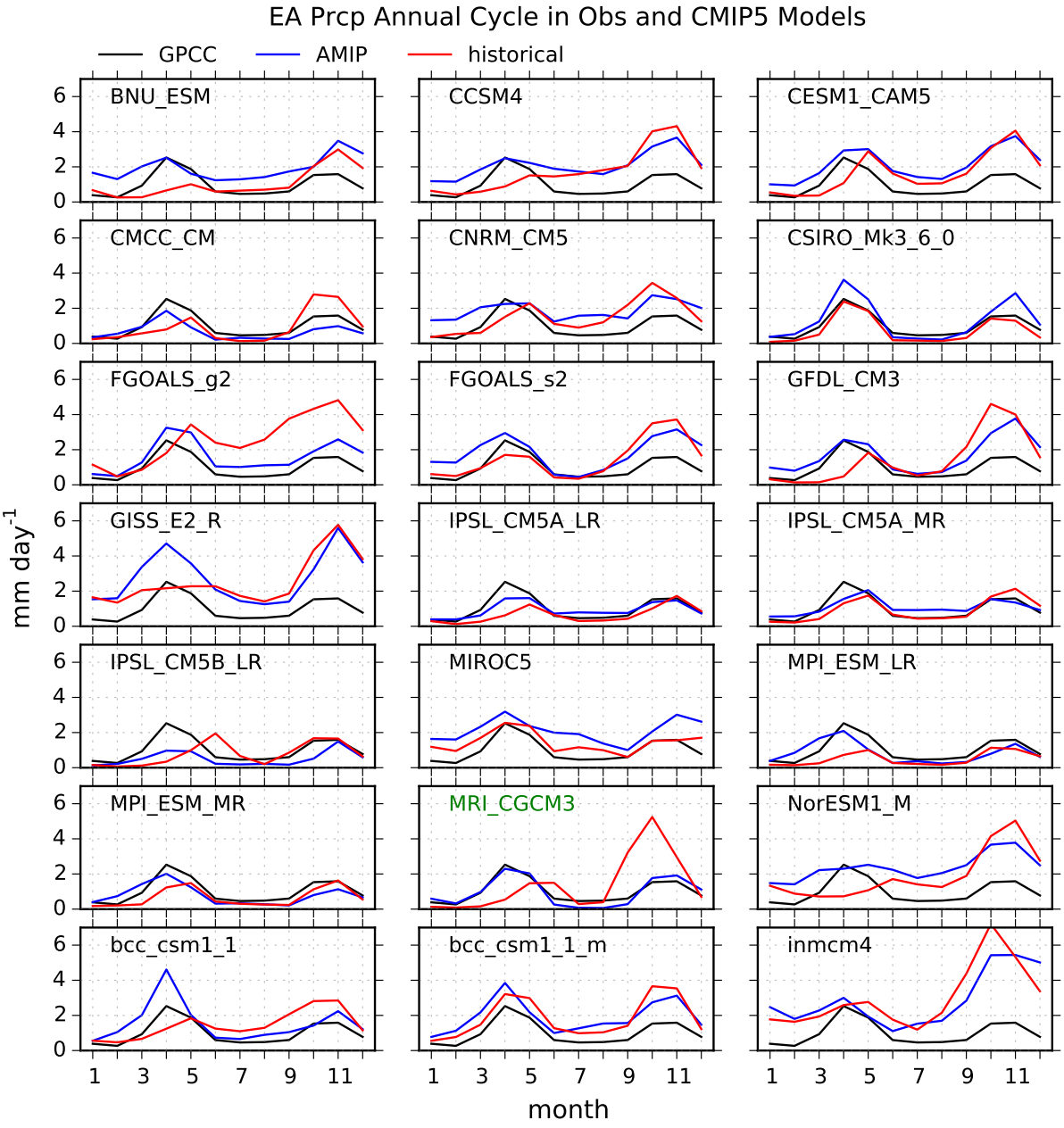

Figure 4.3: East African rainfall annual cycles in GPCC and CMIP5 individual models for the AMIP and historical runs.

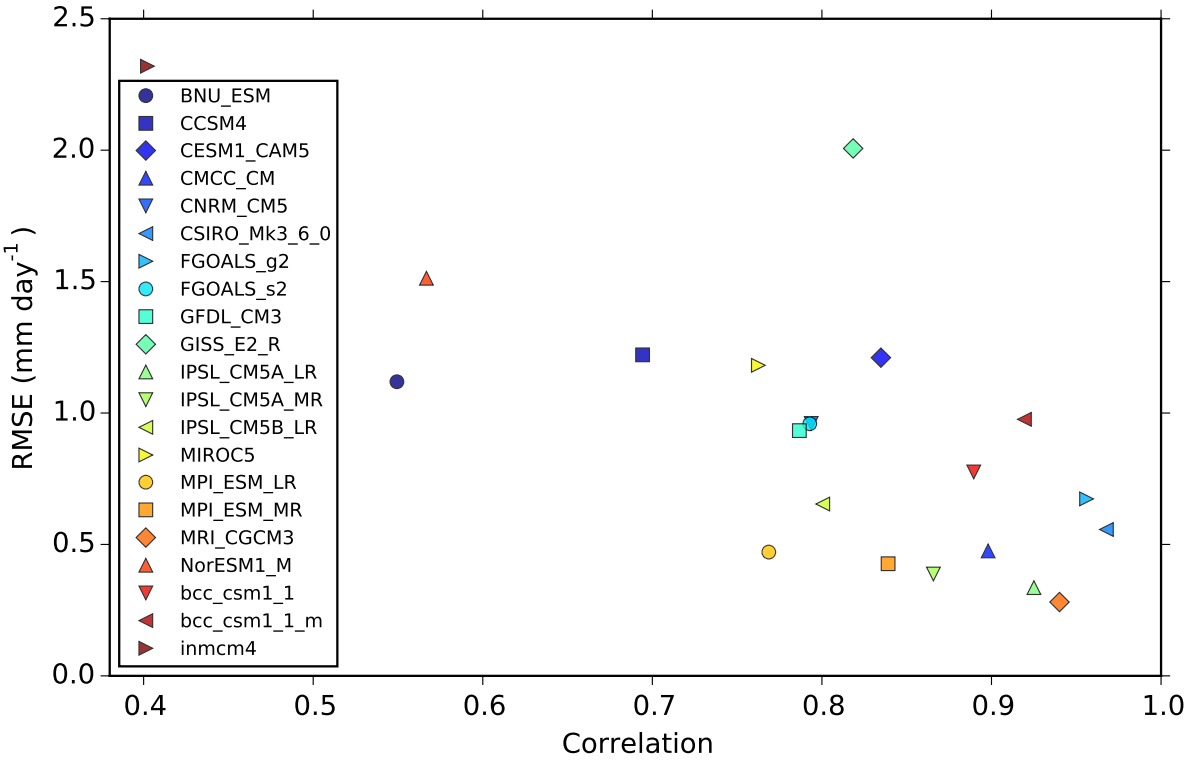

Figure 4.4: Scatter plot of correlation coefficient with the GPCC annual cycle precipitation versus the root mean squared error compared to the GPCC for the CMIP5 model AMIP runs.

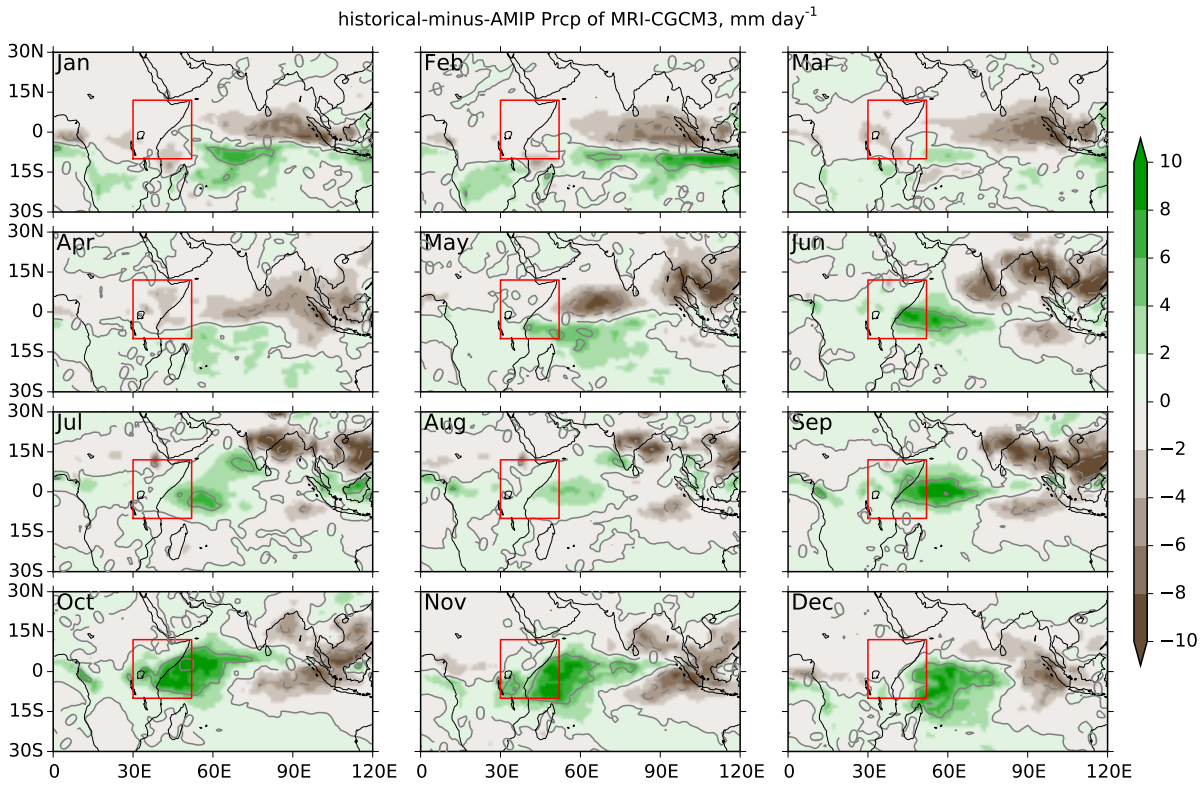

Figure 4.5: Historical-minus-AMIP monthly climatology rainfall of MRI-CGCM3 (both colors and contours). Contours intervals are -10, 5, 0, 5, 10 and units are mm day^{-1}. Red box is the region of 30^{0}E–52^{0}E and 10^{0}S–12^{0}N.

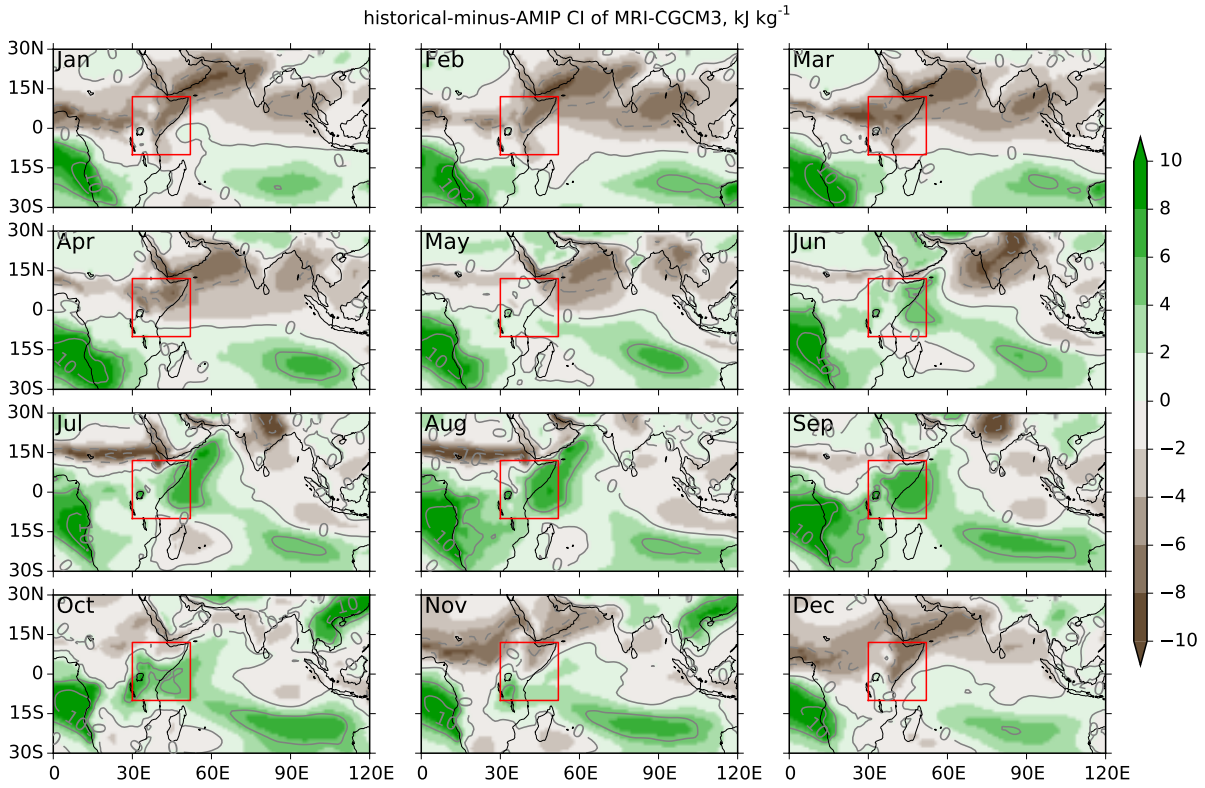

Figure 4.6: Same as Fig. 4.5 except for convective instability (CI) measured by near surface moist static energy minus 700 hPa saturated moist static energy, i.e. $h_s - h^*_{700hPa}$.

north-south contrast from January to May over the Indian Ocean. The northern ocean and East Africa have negative CI anomalies, implying that the atmosphere over these regions is more stable and precipitation is suppressed in the historical run than in the AMIP run, which explains the dry bias over these regions in Fig. 4.5. The CI also develops positive historical minus AMIP bias over the tropical western Indian Ocean starting from June, destabilizing the atmosphere in the historical run, and enhancing precipitation there and over East Africa. It should be noted that the evolutions of the CI and rainfall anomalies are not synchronous over East Africa after June and the CI seems to lead rainfall by one month. For example, CI anomaly over East Africa peaks in August and September while rainfall anomaly peaks in September and October. Also, CI anomaly turns negative over much of East Africa in November while the rainfall anomaly is still slightly positive and becomes negative in December.

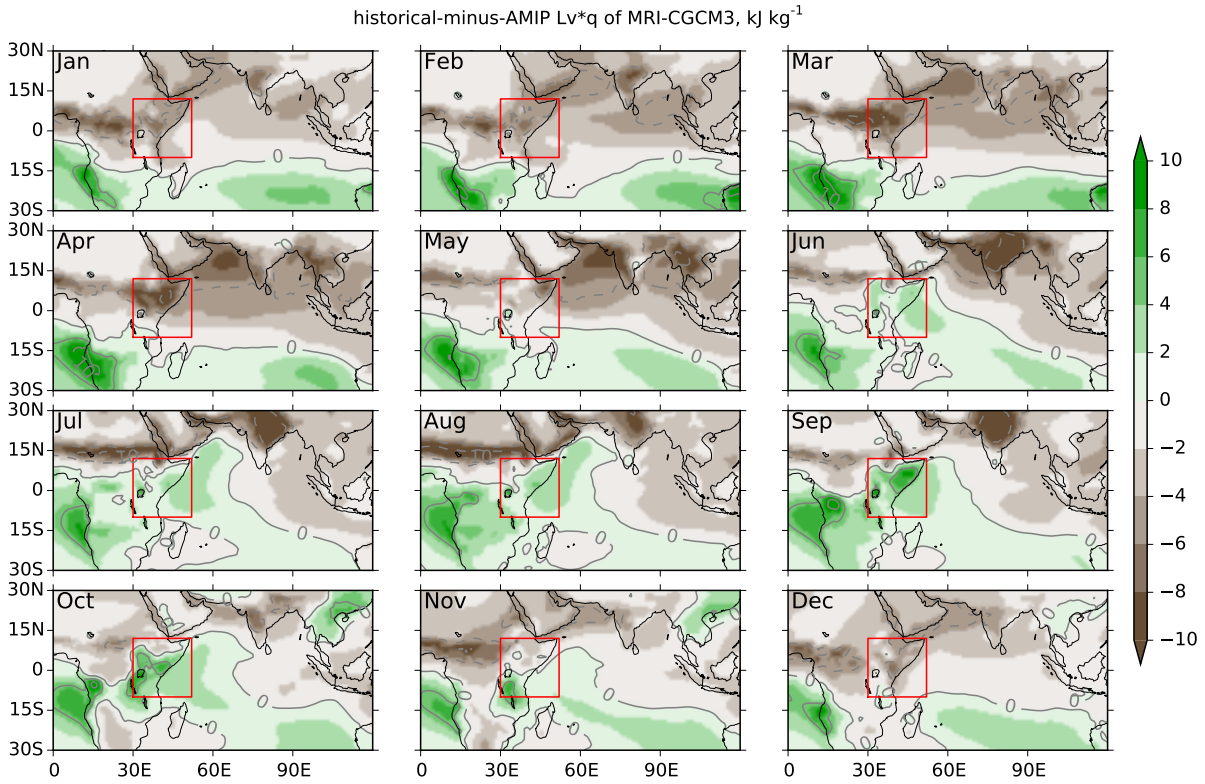

Figure 4.7: Same as Fig. 4.5 except for the moisture component of the near surface moist static energy, i.e. $L_v q$.

We decompose the CI into its components of near surface moist static energy and 700 hPa saturated moist static energy and find the former is the dominant term and the later is secondary and has a slightly destabilizing effect over East Africa (not shown here). The dominant component of the near surface moist static energy is then further decomposed in to components associated with near surface temperature, moisture and geopotential and it is found that the temperature and geopotential components (not shown here) are much smaller in magnitude than the moisture component, which is shown in Fig. 4.7, very similar to the spatial pattern of CI in Fig. 4.6. Hence the change in CI is dominated by the change in low level specific humidity.

Fig. 4.8 summarizes the relationship between rainfall anomalies of historical minus AMIP and CI as well as its different components for MRI-CGCM3. The rainfall anomaly annual cycle (black solid line) is very similar to the multimodel mean (blue solid line

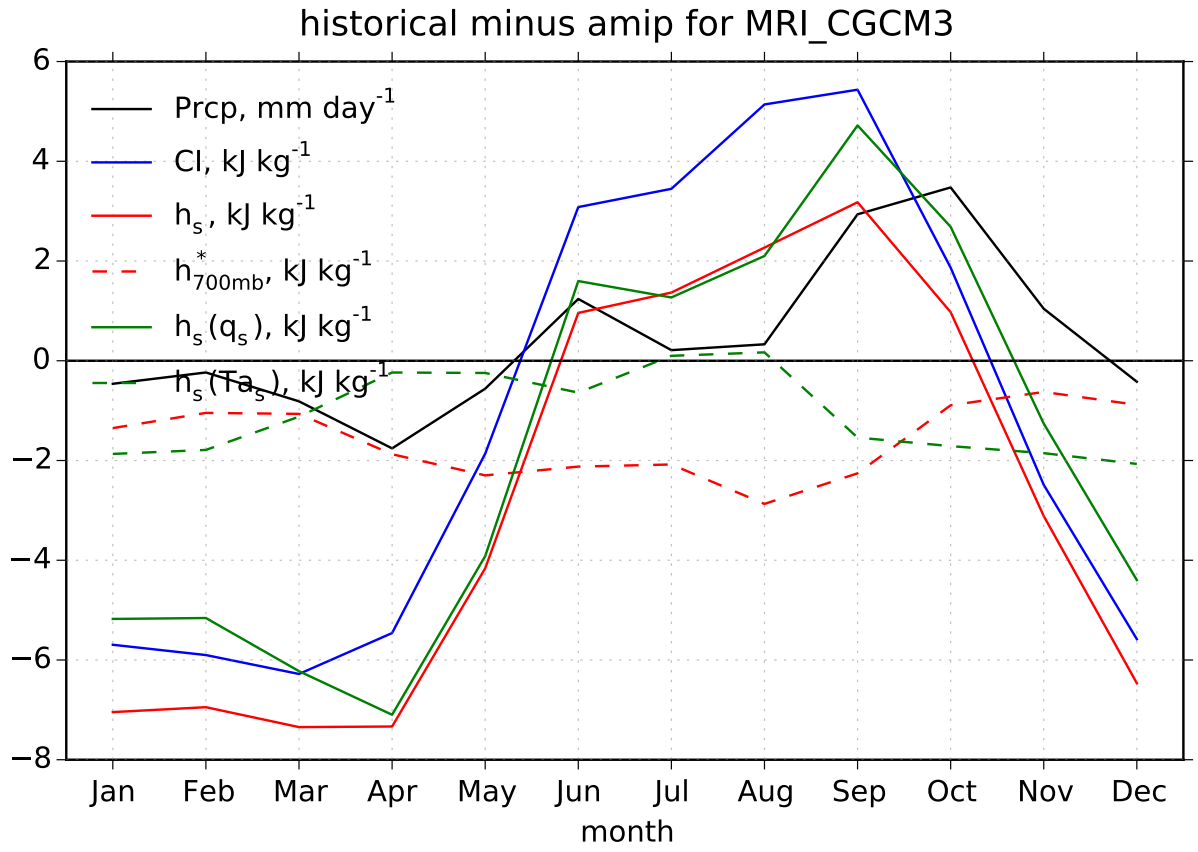

Figure 4.8: Rainfall and CI (as well as its different components) of historical minus AMIP for MRI-CGCM3 averaged over East Africa (the gray shaded grids shown in the mini panel of Fig. 4.1).

in Fig. 4.2) and characterized by overall positive values in the OND rainy season but negative values in the MAM rainy season. The rainfall anomaly can be explained by the CI anomaly and the latter in general leads by one month. Decomposition of the CI shows that the moisture component of the near surface moist static energy emerges as the dominant component.

4.4.2 Surface temperature and heat flux

The fact that the CI anomaly, or equivalently the moist static energy anomaly, of historical minus AMIP agrees well with the rainfall anomaly raises the question of what controls the near surface moist static energy anomaly. Yang et al. (2014a) proposed that SSTs

over the western Indian Ocean play an important role in modulating the East African rainfall annual cycle via controlling the near surface moist static energy. We are therefore wondering if this mechanism can be applied to explain the rainfall difference between the historical run and the AMIP run. Fig. 4.9 shows the historical minus AMIP monthly climatology surface temperature (which is SST over the ocean) for the MRI-CGCM3. This very similar to the spatial patterns of CI in Fig. 4.6 or the moisture component of near surface moist static energy in Fig. 4.7 over the Indian Ocean. The SST bias has a pattern of cold north and warm south from January to May, with the coldest anomaly over the Arabian Sea. A pattern of warm west and cold east develops after May and maintains until October. This new pattern starts to decay from November and restores to the January–May pattern in December. Therefore, the SST difference between the historical and AMIP run can largely explain the CI and the consequent rainfall anomalies over East Africa.

In order to understand whether the SST annual cycle difference between the historical and AMIP run arises from surface heat flux or ocean dynamics, we need to calculate the heat budget of the mixed layer of the ocean. The historical-minus-AMIP form of the ocean mixed layer heat budget can be written as:

$$\rho c_p h \frac{\partial T'}{\partial t} = R'_s + R'_l + LH' + SH' + D'_o \tag{4.1}$$

where ρ, c_p, h and T are the sea water density, specific heat, mixed layer depth and mixed layer average temperature, respectively; heat budget terms $\rho c_p h \partial T/\partial t$, R_s, R_l, LH,SH and D_o are the heat storage tendency, short wave radiation, long wave radiation, latent flux, sensible heat flux and the three-dimensional advection and diffusion by ocean dynamics, respectively. Primes denote the perturbed state in the coupled models from that in the SST-forced models, i.e. historical minus AMIP.

All the surface flux terms are archived for the CMIP5 and thus can be estimated directly. The ocean dynamics term can be estimated as a residual in equation (4.1), i.e.

$$D'_o = \rho c_p h \frac{\partial T'}{\partial t} - (R'_s + R'_l + LH' + SH') \tag{4.2}$$

Fig. 4.10 shows the heat budget annual cycle for MRI-CGCM3 averaged over the

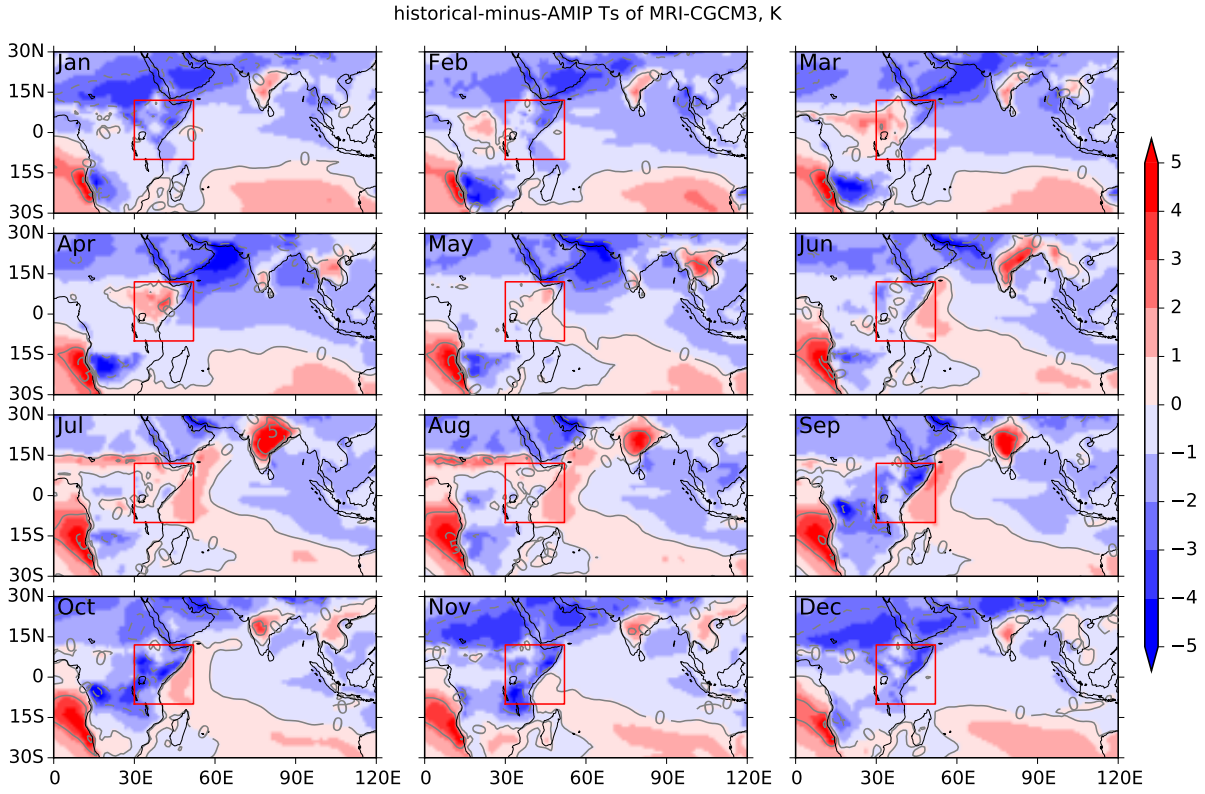

Figure 4.9: Same as Fig. 4.5 except for surface temperature Ts and the contours are -5, -2.5, 0, 2.5, 5.

ocean grids of 30^0E–60^0 and 10^0S–10^0N as well as the corresponding historical-minus-AMIP SST annual cycle. The mixed layer average temperature is approximated by SST when we estimate its tendency. Based on estimates of previous studies (Schneider, 1996; de Boyer Montegut et al., 2004), a $25m$ depth of the mixed layer is selected to estimate the heat storage change in the heat budget in this region. It can be seen from Fig. 4.10 that the sensible heat flux and the long wave radiation are much smaller in amplitude compared to other terms and the heat budget is balanced among heat storage tendency, latent heat flux, short wave radiation and ocean dynamics.

The SST annual cycle (red solid line) is characterized by warm biases during June–October and cold biases during the other months, and dramatic transitions between the two phases. The latter is reflected by the historical-minus-AMIP heat storage tendency ($\rho c_p h dT'/dt$) annual cycle (black solid line). During the cold-to-warm transition from April to June, the heat storage tendency is dominated by insufficient latent flux, and insufficient ocean dynamical cooling. The latent heat flux is larger in magnitude than the ocean dynamical term in April but smaller in June. In May, the magnitudes of these two terms are comparable. The ocean dynamical term keeps positive after June to maintain the warm SST bias until October when it decays close to zero. The second SST transition, from warm to cold, peaks in October and November and the short wave radiation (R'_s, blue solid line) dominates the negative heat storage tendency, probably due to excess precipitation and clouds. The dominant term eventually shifts to the excess latent heat flux (LH', green solid line) in January and February, perhaps arising from stronger northeasterlies of the Asian winter monsoon over the Indian Ocean. Therefore, insufficient ocean dynamical cooling and latent flux both are responsible for the development of the warm SST bias, while insufficient long wave radiation and excess latent heat flux mainly contribute to the cold SST bias.

4.5 Conclusions and discussion

In this study, we investigate the coupled model induced bias of the East African rainfall annual cycle common in CMIP3/5 that overestimates the OND rainfall and underesti-

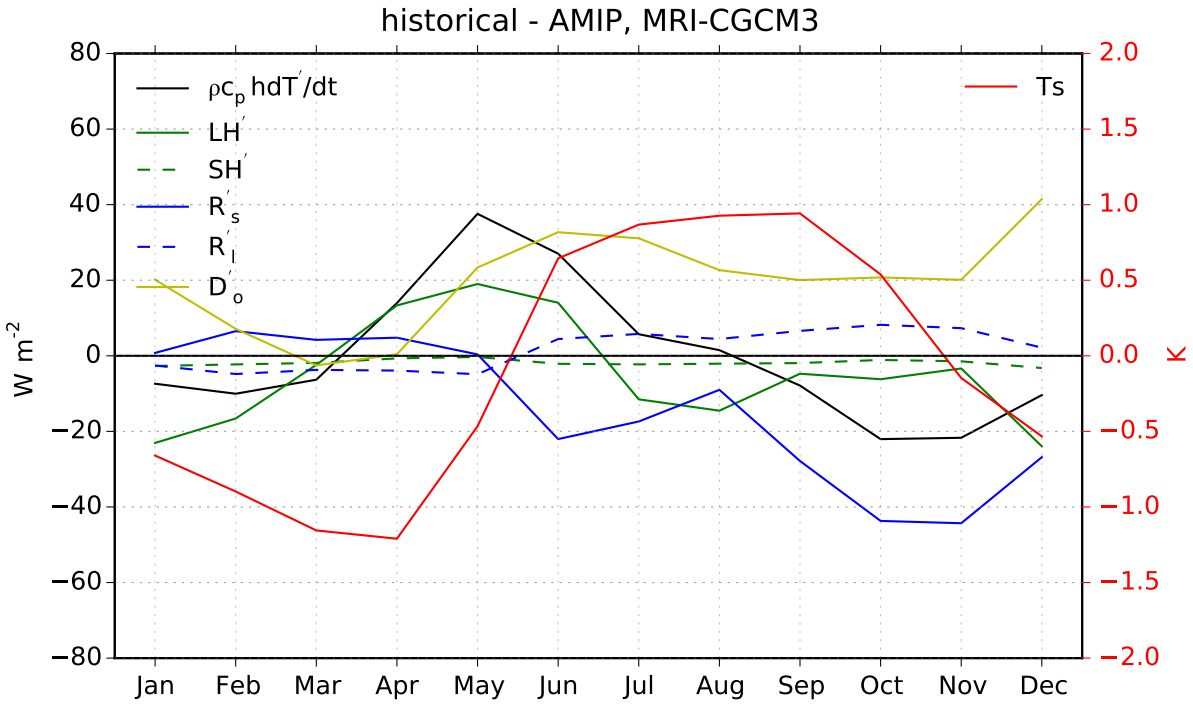

Figure 4.10: Historical-minus-AMIP SST and the ocean mixed layer heat budget in equation (4.1) for MRI-CGCM3, averaged over the ocean grids of 30^0E–60^0 and 10^0S–10^0N.

mates the MAM rainfall, by comparing the historical run (CMIP-style) and the AMIP run (AMIP-style) for each model, with particular emphasis on the MRI-CGCM3. The framework of convective instability (CI) and moiste static energy (MSE) are shown to be able to link this bias to other tropical or global scale biases that have been found in previous studies (Cai and Cowan, 2013; Wang et al., 2014). The following conclusions have been reached:

- East Africa is wetter in CMIP5 historical runs than AMIP runs during the OND short rains season and drier in the MAM long rains season.
- The AMIP run of MRI-CGCM3 reproduces the observed rainfall annual cycle over East Africa very well while its coupled historical run has a similar and stronger bias as the coupled multimodel mean. Therefore, MRI-CGCM3 serves as an exemplary model to study the coupled model induced rainfall bias over East Africa.
- The historical minus AMIP monthly climatology rainfall bias can be explained by the bias in CI, which, itself is dominated by the bias in near surface MSE. The moisture component is the dominant term in the near surface MSE while the temperature component is secondary.
- The near surface MSE bias of historical minus AMIP is modulated by SST bias over the western Indian Ocean.
- Insufficient ocean dynamical cooling and latent flux both are responsible for the development of the warm SST bias of historical minus AMIP in MRI-CGCM3, while insufficient long wave radiation and excess latent heat flux mainly contribute to the cold SST bias.

Wang et al. (2014) have shown that there is a global scale northern hemisphere cooling–southern hemisphere warming bias common to the CMIP5 coupled models, which has been proposed to be linked to the weakening of the AMOC. The cold north and warm south SST bias over the Indian Ocean dominant during December–May found in our study seems to be a local manifestation of this global scale bias and can explain the drier

MAM rainy season over East Africa in coupled models. However, during June–November, the north-south asymmetry over the Indian Ocean is replaced by a west-east contrast: warmer–than–AMIP SSTs in the west and colder–than–AMIP SSTs in the east. This SST bias in the MRI-CGCM3 coupled model greatly increases rainfall over East Africa and can explain the wet bias during the OND rainy season. The mechanism behind the warm west and cold east asymmetry might be linked to the unrealistic mean thermocline slope tilting upward toward the eastern Indian Ocean as pointed out in Cai and Cowan (2013), where they used it to explain the larger amplitude of the Indian Ocean Dipole (IOD) in CMIP3/5 models. However, what ultimately causes the thermocline bias and the detailed processes that develop the bias are less clear and will be explored in the future.

We also notice that the coupling-induced biases of East African precipitation and the Indian Ocean SSTs in the model MRI-CGCM3 (Fig. 4.5 and Fig. 4.9) are accompanied by dry biases of the Indian summer monsoon. Recent studies have shown that SST biases over the Indian Ocean (Prodhomme et al., 2014), including the cold bias of the Arabian Sea (Levine et al., 2013), could contribute to the dry Indian summer monsoon in coupled models relative to observations or their corresponding SST-forced simulations. However, how the dry Indian summer monsoon could impact the Indian Ocean SSTs and East African precipitation is not clear. One potential feedback from the drier Indian summer monsoon is through change of the surface winds over the Indian Ocean. Drier summer India often implies a weakening of the monsoon circulation, especially the low level winds around the Somali jet region. This could lead to reduced evaporation and weakened coastal upwelling over the western Indian Ocean off the coast of East Africa, and both of these two effects could warm the SSTs there. This warm coastal SST bias resulting from the potential feedback of the weakened Indian summer monsoon is consistent with the SST biases found in the coupled models. Further work is needed to quantify this feedback, or examine whether it is a primary cause of the Indian SST biases rather than a passive feedback.

The warm bias in the west and cold bias in the east over the equatorial Indian Ocean are actually weakening the zonal asymmetry of the observed SST and this weakening is not unique over the Indian Ocean but can also be seen over the Pacific and Atlantic Oceans (Fig. 4.11a). The annual mean SST zonal asymmetry bias is weak over the Indian Ocean due to pronounced seasonality, but very strong over the Pacific and Atlantic Oceans due to dramatic warming over the tropical eastern basins especially nearby the western coasts of South America and Africa. The warm biases over the tropical eastern Pacific and Atlantic in coupled climate models have also been reported in previous studies and explained by excess heat flux into the ocean due to insufficient low-level clouds (Mechoso et al., 1995; Huang et al., 2007), and insufficient cooling by ocean dynamical processes (Colas et al., 2012). The general weakening of the zonal SST asymmetry over all the tropical ocean basins in coupled climate models suggests that these coupled models generally have difficulty in capturing the correct ocean processes that are important in determining the SSTs over the coastal upwelling regions. In other words, these coupled models tend to underestimate the thermostat mechanism as proposed by Clement et al. (1996). Fig. 4.11b shows the change of multimodel mean annual mean SST from the 1979–2005 historical runs to the 2070–2099 RCP8.5 runs in CMIP5 (colors, the 30^0S–30^0N tropical mean has been removed to emphasize the non-uniform component), which also implies a weakening of the zonal SST asymmetry near the equator over all the ocean basins. The much faster warming SST projection off the coast of East Africa than that over the equatorial eastern Indian Ocean might partly explain the wetting projection in East Africa. However, if the response of the SSTs to the anthropogenic forcings in coupled models is greatly influenced by their performance in simulating the tropical zonal SST asymmetry then the reliability of these SST projections and the associated precipitation projections will be in question. Further examination is needed to reveal if these two are related.

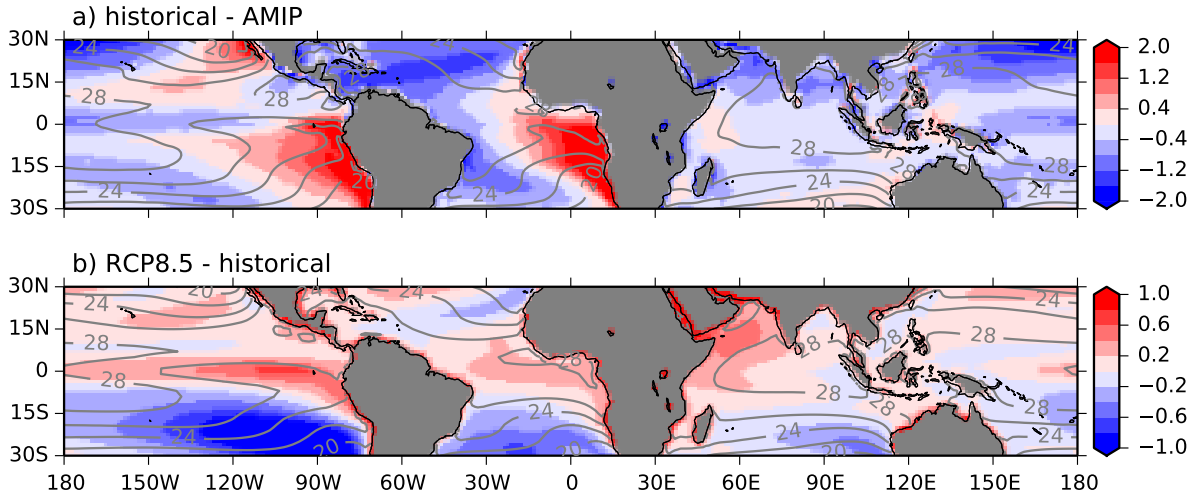

Figure 4.11: a) Annual mean SST climatology of the CMIP5 AMIP runs (contours) and its change from the AMIP to the multimodel mean of the historical runs (colors); b) Multimodel mean annual mean SST climatology of the CMIP5 historical runs (contours) and its change from the historical to RCP8.5 runs (colors, the 30^0S–30^0N tropical mean change has been removed to emphasize the spatial pattern of the non-uniform component). The models used to calculate the multimodel mean are the 38 models from the CMIP5 that have surface temperature available in both the historical and RCP8.5 runs as described in `http://kage.ldeo.columbia.edu:81/expert/SOURCES/.LDEO/.ClimateGroup/.PROJECTS/.IPCC/.CMIP5/.MultiModelMeans/.MMM-v2/.dataset_documentation.html`. The climatology is estimated based on the period of 1979–2005 for the AMIP and historical runs and 2070–2099 for the RCP8.5 runs.

CHAPTER 5

Zonal Momentum Balance in the Tropical Atmospheric Circulation during the Global Monsoon Mature Months *

5.1 Introduction

Since its introduction by Matsuno (1966), the equatorial beta-plane linear model has been serving as a simple dynamical framework for simulating the tropical circulation (Gill, 1980; Davey and Gill, 1987; Seager, 1991). Most of these works assume that the total troposphere can be approximated by the single, first baroclinic mode in the vertical such that the shallow water equations can be used to represent the dynamics driven by middle troposphere heating. Lindzen and Nigam (1987) used a different approach that only considers the dynamics of the atmospheric boundary layer (ABL) driven by the pressure gradients due to sea surface temperature gradients but this too yielded a set of shallow water equations with dynamics equivalent to that of the first baroclinic mode method (Neelin, 1989). Later works combined these two ideas to construct a new model structure with an ABL at the bottom plus a first baroclinic mode of the free troposphere above (Wang and Li, 1993; Fu and Wang, 1999).

Despite the success in simulating the general features of the tropical circulation, this type of simple tropical atmospheric circulation model has been challenged because the nonlinear advection terms have been totally ignored and large Rayleigh friction coefficients have to be applied in order to obtain realistic simulations. Diagnostics of the observed circulation confirmed the suitability of a linear approximation of the surface wind momentum dynamics (Zebiak, 1990; Deser, 1993), although the Rayleigh friction coefficients were demonstrated to be latitude-dependent and have different magnitudes

* The work of this chapter has been published as: Yang, W., R. Seager, and M. A. Cane, 2013: Zonal momentum balance in the tropical atmospheric circulation during the global monsoon mature months. *J. Atmos. Sci.*, **70 (2)**, 583–599, doi: 10.1175/JAS-D-12-0140.1.

for zonal and meridional winds (Deser, 1993; Chiang and Zebiak, 2000). Recent studies (Lin et al., 2008) revealed the potential sources of the strong Rayleigh friction over different regions within the Walker circulation: in the deep convection region (the western branch of the Walker circulation), both nonlinear advection and convective momentum transfer (CMT) contribute in the upper troposphere as well as in the lower troposphere; in the shallow convection region (the eastern branch of the Walker circulation), the nonlinear advection contributes in the upper troposphere while the CMT only contributes in the lower troposphere. However, Lin et al. (2008) focused on the zonal momentum balance in the longitude-pressure cross section near the equator instead of the whole tropics and only the annual mean circulation was investigated.

Another issue relevant to the zonal momentum budget is how the equatorial upper troposphere zonal winds are maintained. In their explanation of why the climatological zonal winds are dominated by easterlies in the equatorial upper troposphere, Lee (1999) challenged the idea that the easterlies are maintained by the momentum flux divergence of the midlatitude-generated synoptic eddies (Suarez and Duffy, 1992) and proposed that they are maintained by the transient zonal mean meridional circulation associated with the seasonal cycle of the Hadley circulation and decelerated by tropical transient eddies with intraseasonal, intraannual and interannual time scales. GCM studies also showed that the easterlies in the equatorial upper troposphere are driven by the cross-equatorial mean meridional circulation while the tropical eddies tend to decelerate them (Kraucunas and Hartmann, 2005). Dima et al. (2005) conducted a systematic investigation on the tropical zonal mean zonal momentum balance based on the NCEP/NCAR reanalysis dataset and confirmed the ideas in Lee (1999) and Kraucunas and Hartmann (2005). However, only the global zonal mean circulations have been examined in these studies and the zonal asymmetry has not been considered. This is important because tropical upper troposphere easterlies are not uniformly distributed in the zonal direction and westerlies can dominate under some conditions (e.g. over the east Pacific during boreal winter). It is interesting to examine if the easterly maintenance mechanism for the global zonal mean flow can be extended to local longitudes and, in contrast, what mechanism is

responsible for the maintenance of local westerlies at other longitudes.

In this study we will examine the zonal momentum balances of the tropical atmospheric circulation in January (which represents the peak of the southern hemisphere monsoon) and July (which represents the peak of the northern hemisphere monsoon) in three dimensions based on the ERA-Interim reanalysis. We will extend the study of annual mean momentum balance near the equator by Lin et al. (2008) to the momentum balance in particular months (January and July) and throughout the tropics. Our study also goes beyond the work of Lee (1999), Dima et al. (2005) and Kraucunas and Hartmann (2005) by considering the longitudinal asymmetry, i.e. the zonal distribution of zonal momentum. The key questions to be answered include: what are the dominant terms in the tropical zonal momentum balance? How good is the linear dynamics approximation for the zonal momentum equation in the widely used simple tropical atmospheric models? Which mechanism is responsible for the maintenance of the dominant easterlies in the equatorial upper troposphere in the regions where they exist? What are the differences in the zonal momentum budget between January and July? The chapter is organized as follows: data and methods are described in Section 5.2. Section 5.3 analyzes the zonal momentum balance on 925hPa (which represents the atmospheric boundary layer) and 200hPa (which represents the upper troposphere). Section 5.4 investigates the zonal momentum balance near the equator, where the Coriolis force approaches zero. Both the zonal mean and local longitudinal mean momentum balances are examined in Section 5.5. Section 5.6 estimates the equivalent Rayleigh friction both in the atmospheric boundary layer and the upper free troposphere. The conclusions and discussion are given in Section 5.7.

5.2 Data and methods

The daily versions of ERA-Interim reanalysis data (Dee et al., 2011) in January and July are used in the zonal momentum balance analysis. The spatial resolution is 1.5^0 longitude by 1.5^0 latitude. The period of data used in our paper range from the year of 1979 to 2010.

The zonal momentum equation in pressure coordinates can be can be obtained by applying the multiple year monthly mean to equation (2) of Lin et al. (2008)'s daily version of zonal momentum equation:

$$\frac{\partial \overline{u}}{\partial t} = -(\overline{u}\frac{\partial \overline{u}}{\partial x} + \overline{v}\frac{\partial \overline{u}}{\partial y} + \overline{\omega}\frac{\partial \overline{u}}{\partial p}) - \frac{\partial \overline{\phi}}{\partial x} + f\overline{v} - (\frac{\partial \overline{u'u'}}{\partial x} + \frac{\partial \overline{u'v'}}{\partial y} + \frac{\partial \overline{u'\omega'}}{\partial p}) + X \qquad (5.1)$$

where u, v, ϕ, f are the zonal velocity, meridional velocity, geopotential, and Coriolis parameter, respectively; the bar denotes the multiple year mean of the daily data in a specific month (in the case of this paper, January or July) and the prime denotes the daily deviation from the multiple year monthly mean. In the multiple year monthly mean momentum balance equation (5.1), the term on the left hand side can be neglected; the term $-(\overline{u}\partial\overline{u}/\partial x + \overline{v}\partial\overline{u}/\partial y + \overline{\omega}\partial\overline{u}/\partial p)$ is the nonlinear advection by the stationary flow and the term $-(\partial\overline{u'u'}/\partial x + \partial\overline{u'v'}/\partial y + \partial\overline{u'\omega'}/\partial p)$ is the nonlinear transient eddy force; $-\partial\overline{\phi}/\partial x$ is the pressure gradient force and $f\overline{v}$ is the Coriolis force; X represents all the forces from the unresolved sub-grid scale and possibly errors involved in the estimation process and data themselves.

In the ABL, X is expected to be dominated by friction induced by turbulence and can be parameterized reasonably well by Rayleigh friction (Zebiak, 1990; Deser, 1993). The scatter plots of X vs. $\overline{u}$ at all grid points at 925hPa in Fig. 5.1 show that there is a negative correlation between the residual term and the zonal velocity. The correlation coefficients have little difference between January and July but are larger over the oceans than over land. Also, the Rayleigh friction coefficients (the negative of the regression coefficients) are three to four times larger over land than over oceans, indicating much stronger friction over land due to the rougher surface. Fig. 5.2 and 5.3 show the Rayleigh friction estimate of X with the zonal velocity $\overline{u}$ at 925hPa, using different regression coefficients for the oceans and land, as shown in Fig. 5.1. The regressions account for the majority of X over the oceans in both January and July. Over land, however, the regression does not perform as well, reflecting the inhomogeneity of surface roughness making it difficult to use a uniform Rayleigh friction coefficient.

In the free troposphere over the open ocean, Carr and Bretherton (2001) and Lin et al.

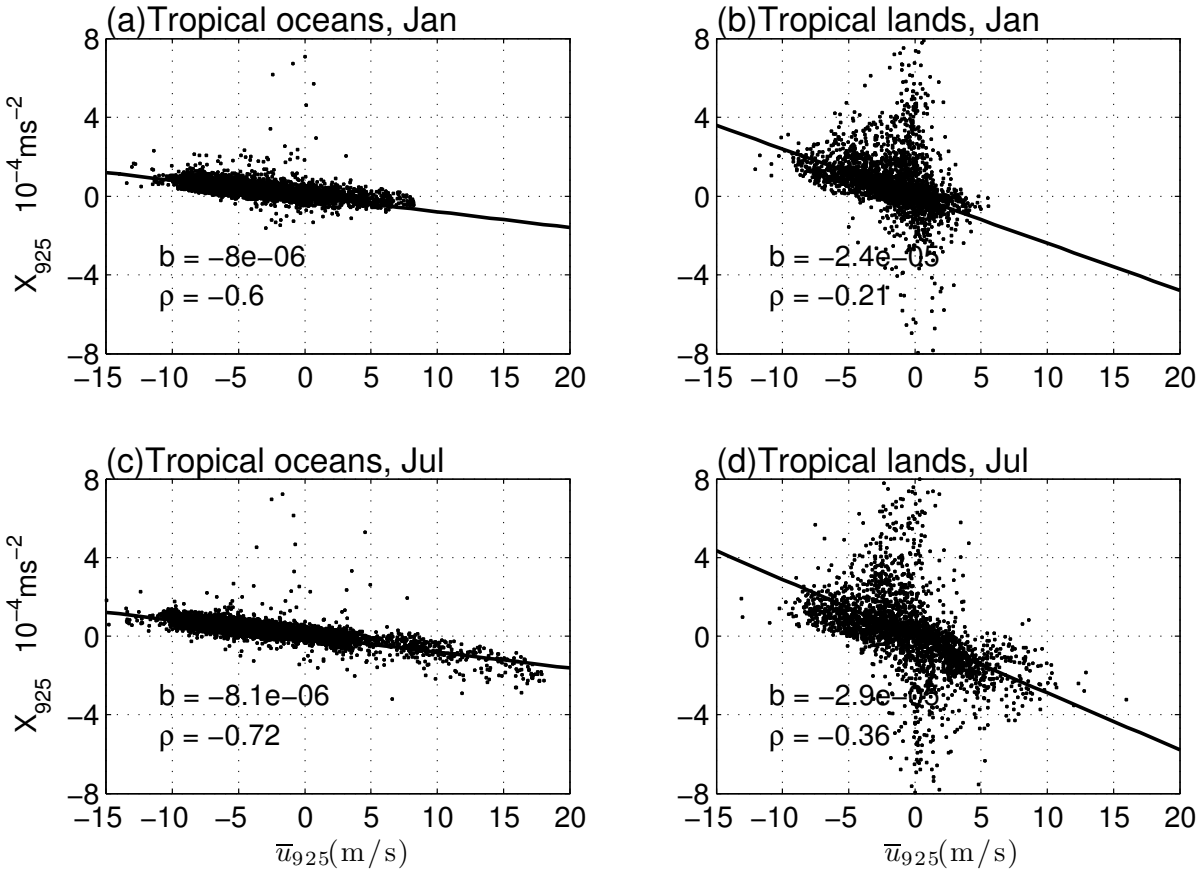

Figure 5.1: Scatter plot of X vs. $\overline{u}$ at 925hPa over tropical oceans and tropical lands (between 30^0N and 30^0S) in January and July. Each point in the scatter plot is corresponding to a grid point at the 925hPa pressure level. ρ and b indicate the correlation coefficient and the regression coefficient (based on regression model $\hat{X} = b \cdot \overline{u}$), respectively.

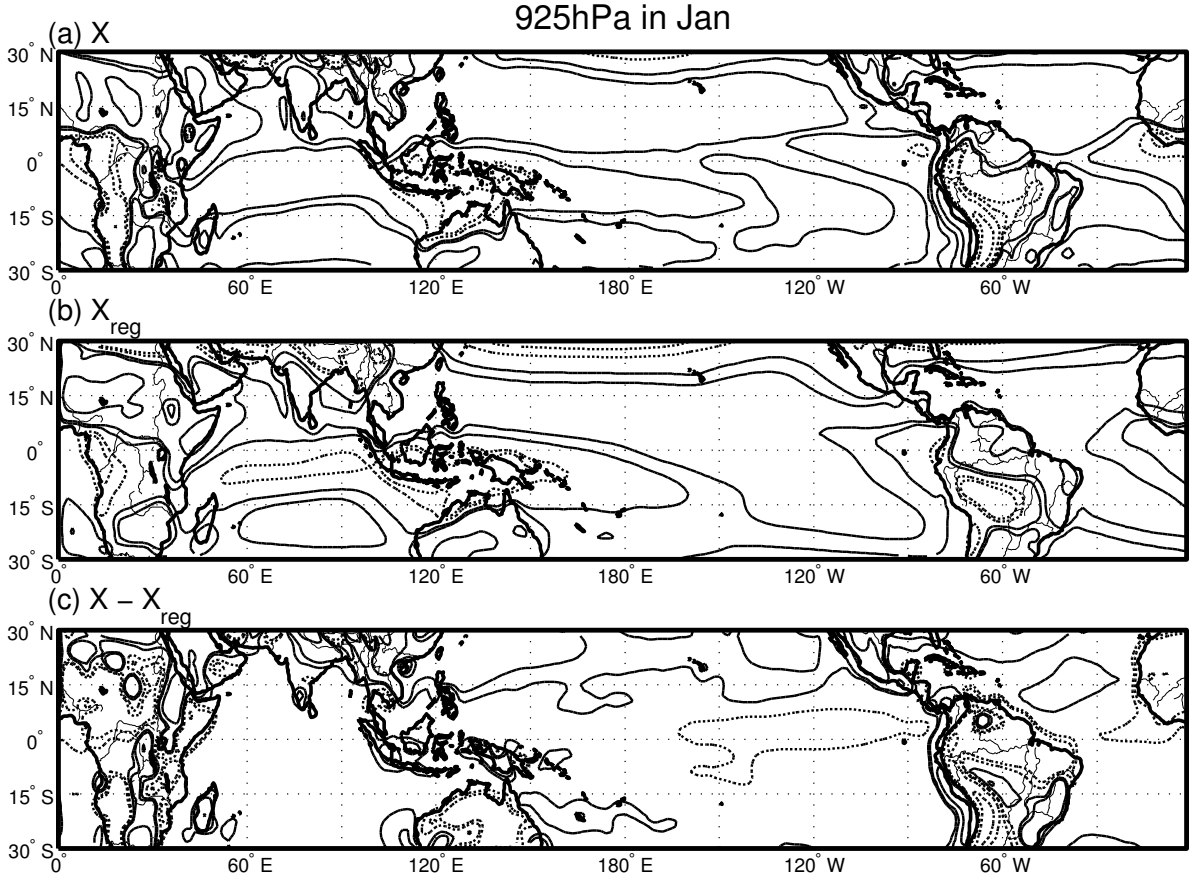

Figure 5.2: Regression of X by $\overline{u}$ at 925hPa in Jan. (a) The residual term (X). (b) The regression of X. (c) The difference between X and its regression. The contour values are [-6.4 -1.6 -0.4 -0.2 0.2 0.4 1.6 6.4]$\times 10^{-4} m\, s^{-2}$. Solid and dashed lines represent positive and negative values, respectively. In order to focus on large scale features, the traditional 1-2-1 low pass filter is applied twice in both dimensions for each contour field.

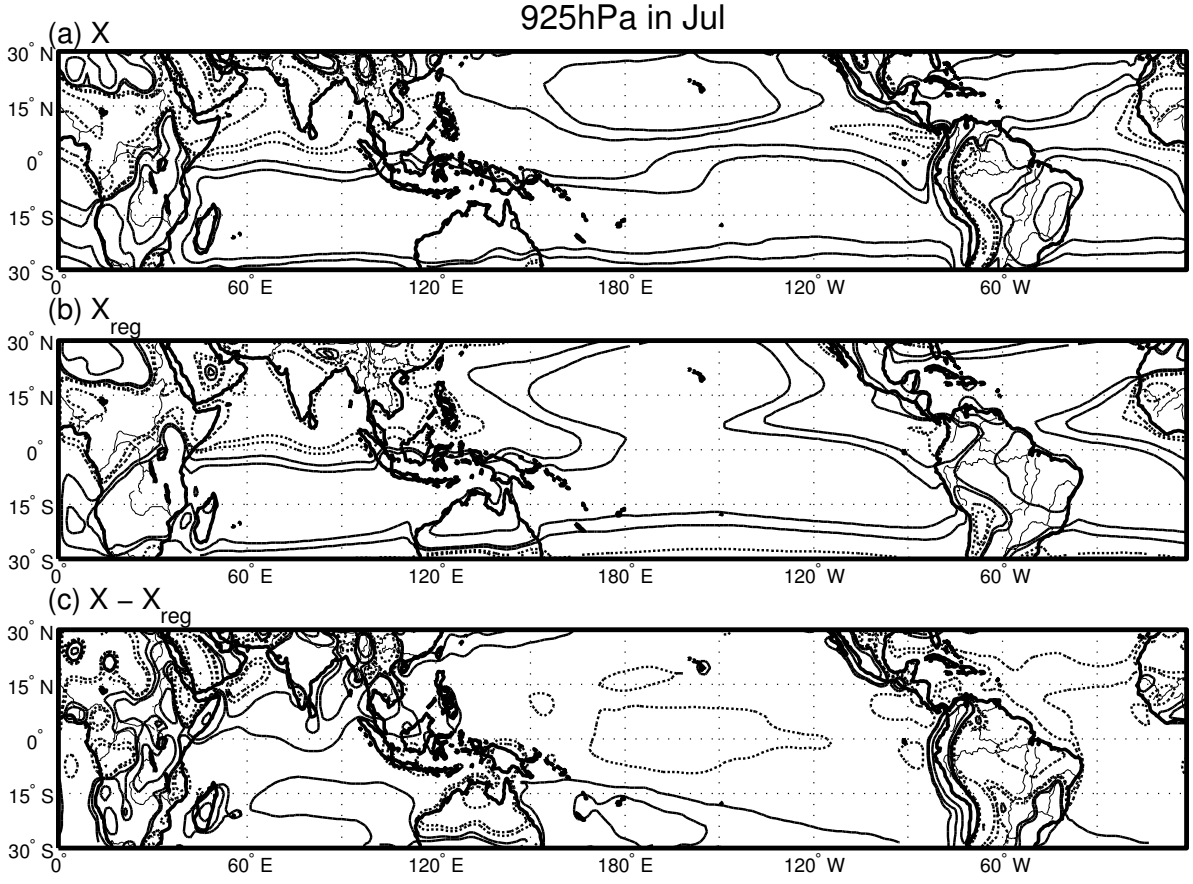

Figure 5.3: Same as Fig. 5.2 except for July.

(2008) demonstrated that X is dominated by the CMT. As argued in Lin et al. (2008), CMT can be approximated by

$$\text{CMT} \approx \delta_c(u_b - u) \tag{5.2}$$

where δ_c is the cloud detrainment rate, u_b is the zonal wind at cloud base and u is the zonal wind in the free troposphere. By assuming δ_c is proportional to precipitation rate and choosing the cloud base approximately at 925hPa, the CMT can be expressed as:

$$\text{CMT} \approx b \times P \times (u_{925} - u) \tag{5.3}$$

where P is the precipitation rate and b is the coefficient relating δ_c and P. Fig. 5.4 shows the relation between X (as shown in colors) and prcp $*$ $(\overline{u}_{925} - \overline{u}_{200})$ (as shown in contours) at 200hPa. The total precipitation in the ERA-Interim reanalysis dataset is used here. The precipitation from the version 2.2 of the NASA Global Precipitation Climatology Project (GPCP) (Adler et al., 2003; Huffman et al., 2009) was also used for this calculation but the results are not shown here as they are not significantly different from those using the ERA-Interim precipitation. In both January and July, these two terms have a qualitative spatial relationship with each other, indicating that at least part of the residual term X can indeed be explained by CMT in the free troposphere. To quantify the relationship between these two terms, scatter plots and regression analysis are performed on the grid points over the oceans (Fig. 5.4 (c) and (e)) and over the lands (Fig. 5.4 (d) and (f)) separately. It is found that the spatial correlation between X and the estimated CMT behaves differently between oceans and land. While the correlation coefficients over the oceans have higher values (0.37 in January and 0.19 in July), they are weak and even negative over lands. This is consistent with Carr and Bretherton (2001) and Lin et al. (2008) who showed that CMT dominates the residual of the momentum budget only over open oceans in the free troposphere. It should also be mentioned here that the estimated CMT is quantitatively only able to account for less than half of the whole residual term X even over the oceans, reflecting either the crudeness of the representation of the cloud detrainment rate by the precipitation rate or the contamination of X by

other sources (e.g. gravity waves, data errors).

The longitudinal mean (i.e. average between two specific longitudes) version of the momentum balance equation above can be written as:

$$\begin{aligned}
\frac{\partial[\overline{u}]}{\partial t} &= -\{[\overline{u}\frac{\partial \overline{u}}{\partial x} + \overline{v}\frac{\partial \overline{u}}{\partial y} + \overline{\omega}\frac{\partial \overline{u}}{\partial p}]\} - \frac{\partial[\overline{\phi}]}{\partial x} + f[\overline{v}] - [\frac{\partial \overline{u'u'}}{\partial x} + \frac{\partial \overline{u'v'}}{\partial y} + \frac{\partial \overline{u'\omega'}}{\partial p}] + [X] \\
&= -([\overline{u}]\frac{\partial[\overline{u}]}{\partial x} + [\overline{v}]\frac{\partial[\overline{u}]}{\partial y} + [\overline{\omega}]\frac{\partial[\overline{u}]}{\partial p}) - \{[\overline{u}^*\frac{\partial \overline{u}^*}{\partial x} + \overline{v}^*\frac{\partial \overline{u}^*}{\partial y} + \overline{\omega}^*\frac{\partial \overline{u}^*}{\partial p}]\} \\
&\quad -\frac{\partial[\overline{\phi}]}{\partial x} + f[\overline{v}] - [\frac{\partial \overline{u'u'}}{\partial x} + \frac{\partial \overline{u'v'}}{\partial y} + \frac{\partial \overline{u'\omega'}}{\partial p}] + [X] \qquad (5.4)
\end{aligned}$$

where the square brackets denote the longitudinal mean and the stars denote the deviation from the longitudinal mean. The first term in braces represents the forcing from the longitudinal mean stationary flow while the second term in braces represents the forcing from the stationary eddies. If the longitudinal mean is taken over all longitudes, the traditional zonal mean version of the momentum balance equation can be simplified as:

$$\begin{aligned}
\frac{\partial[\overline{u}]}{\partial t} &= -[\overline{v}\frac{\partial \overline{u}}{\partial y} + \overline{\omega}\frac{\partial \overline{u}}{\partial p}] + f[\overline{v}] - [\frac{\partial \overline{u'v'}}{\partial y} + \frac{\partial \overline{u'\omega'}}{\partial p}] + [X] \qquad (5.5) \\
&= -([\overline{v}]\frac{\partial[\overline{u}]}{\partial y} + [\overline{\omega}]\frac{\partial[\overline{u}]}{\partial p}) - [\overline{v}^*\frac{\partial \overline{u}^*}{\partial y} + \overline{\omega}^*\frac{\partial \overline{u}^*}{\partial p}] \\
&\quad +f[\overline{v}] - [\frac{\partial \overline{u'v'}}{\partial y} + \frac{\partial \overline{u'\omega'}}{\partial p}] + [X] \qquad (5.6)
\end{aligned}$$

In many simple tropical dynamics models, the momentum equations are approximated by linear dynamics; i.e. retain the pressure gradient force and Coriolis force on the right hand side of equation (5.1) and parameterize the total effect of all the other terms on the right hand side of equation (5.1) with Rayleigh friction. Then the linear version of the zonal momentum equation (5.1) becomes

$$\frac{\partial \overline{u}}{\partial t} = -\frac{\partial \overline{\phi}}{\partial x} + f\overline{v} - \epsilon\overline{u} \qquad (5.7)$$

where ϵ is the friction coefficient. Using the monthly means of the pressure gradients, zonal winds and meridional winds over multiple years from the reanalysis data, we can estimate the equivalent Rayleigh friction coefficient on each grid point by linear regression.

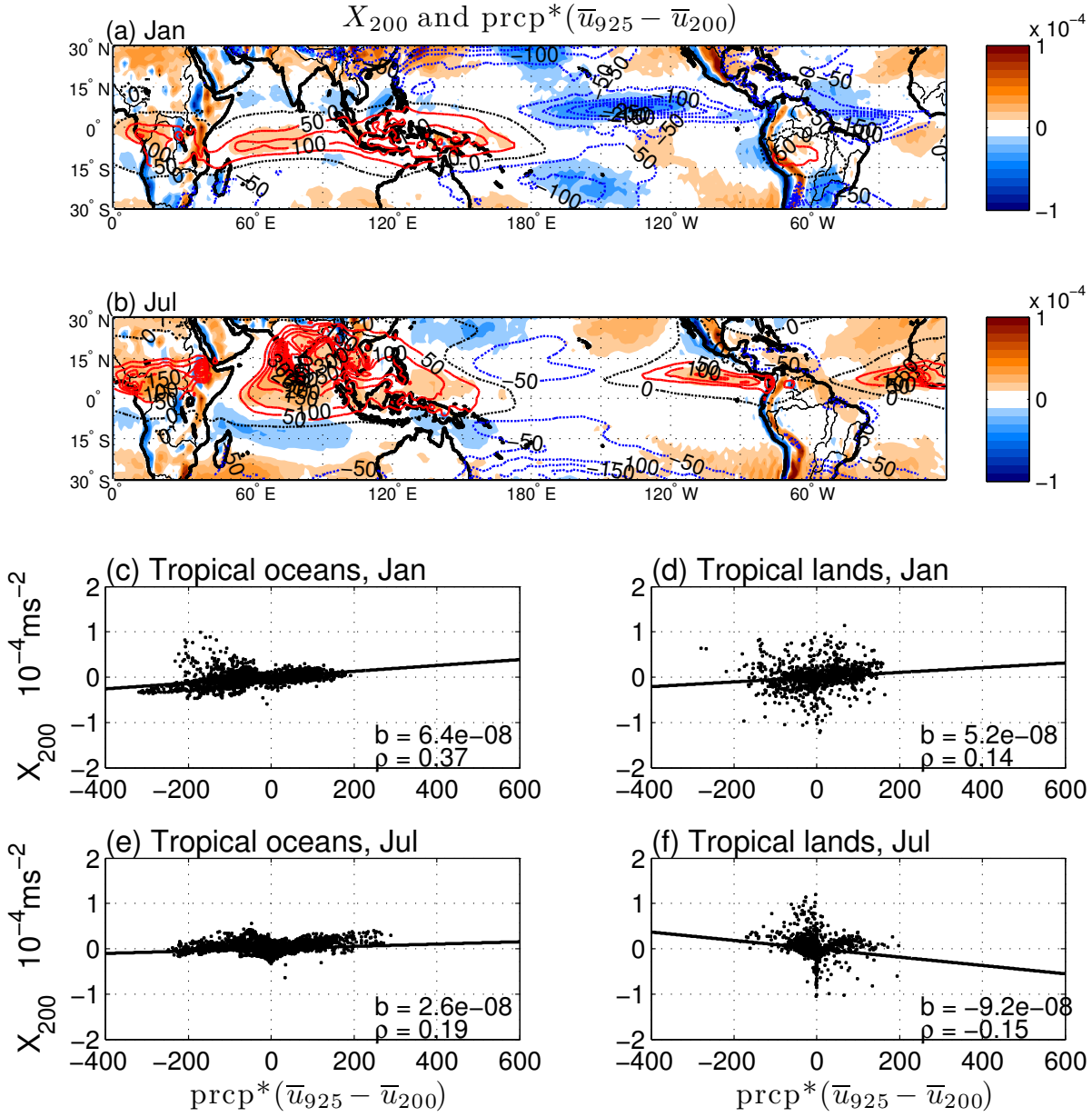

Figure 5.4: The residual term X (colors) and prcp*$(\overline{u}_{925} - \overline{u}_{200})$ (contours) at 200hPa in January (a) and July (b). The unit for X is ms^{-2} and for prcp*$(\overline{u}_{925} - \overline{u}_{200})$ is $mm\,day^{-1}\,m\,s^{-1}$. (c), (d), (e) and (f) are the scatter plots of X vs. prcp*$(\overline{u}_{925} - \overline{u}_{200})$ over tropical oceans in January, tropical lands in January, tropical oceans in July and tropical lands in July, respectively. Only grid points with precipitation rate greater than 2 mm day^{-1} are used. ρ is the correlation coefficient between X and prcp*$(\overline{u}_{925} - \overline{u}_{200})$ and b is the regression coefficient when the regression model $\hat{X}$ = b*prcp*$(\overline{u}_{925} - \overline{u}_{200})$ is used.

5.3 Zonal momentum balance on pressure levels

Fig. 5.5 shows the right hand side terms in the zonal momentum equation (5.1) in January on the 925hPa pressure level. It can be seen from Fig. 5.5 that the zonal momentum balance in the atmospheric boundary layer (ABL) is among three dominant terms: the pressure gradient force (Fig. 5.5(a)), the Coriolis force (Fig. 5.5(b)) and the residual term X, which is here primarily surface friction(Fig. 5.5(e)). One measure of the overall magnitude of each term over the two dimensional grids is the root mean squared (RMS) value. The calculations show that the RMS values for the pressure gradient force and the Coriolis force are both $1.1\times10^{-4}m\,s^{-2}$ and the value of the residual force is $9.8\times10^{-5}m\,s^{-2}$, indicating that the magnitudes of the three dominant terms are of the same order. The RMS value of the nonlinear advection term is only $1.4\times10^{-5}m\,s^{-2}$ and the eddy forcing is even smaller, with an RMS value of $6.5\times10^{-6}m\,s^{-2}$.

In July, the zonal momentum balance on the 925hPa level (Fig. 5.6) shares similar features with that in January. In general, the dominant terms are still the same: the pressure gradient force (Fig. 5.6(a)), the Coriolis force (Fig. 5.6(b)) and the friction (Fig. 5.6(e)), with RMS values of $1.3\times10^{-4}m\,s^{-2}$, $1.2\times10^{-4}m\,s^{-2}$ and $1.1\times10^{-4}m\,s^{-2}$, respectively. The magnitude of the transient eddy force (Fig. 5.6(d)) is again one order weaker than the those of the dominant terms. The nonlinear advection term (Fig. 5.6(c)) is in general much weaker than the dominant terms, indicated by the much smaller RMS value of $2.1\times10^{-5}m\,s^{-2}$. However, the nonlinear advection by the stationary flow has comparable magnitudes with the dominant terms in the Asian monsoon regions, especially near the Somali Jet. This implies that the large scale Asian summer monsoon circulation is nonlinear even in the ABL.

Fig. 5.7 shows the zonal momentum balance of the multiple year mean January flow on the 200hPa pressure level. Similar to the ABL case, the pressure gradient force (Fig. 5.7(a))and the Coriolis force (Fig. 5.7(b)) are the dominant terms in the zonal momentum balance, with RMS values of $1.5\times10^{-4}m\,s^{-2}$ and $2.2\times10^{-4}m\,s^{-2}$ respectively. However, unlike the boundary layer cases, the residual force is no longer among the dominant forces everywhere with an RMS value of only $1.4\times10^{-5}m\,s^{-2}$, almost one order smaller than

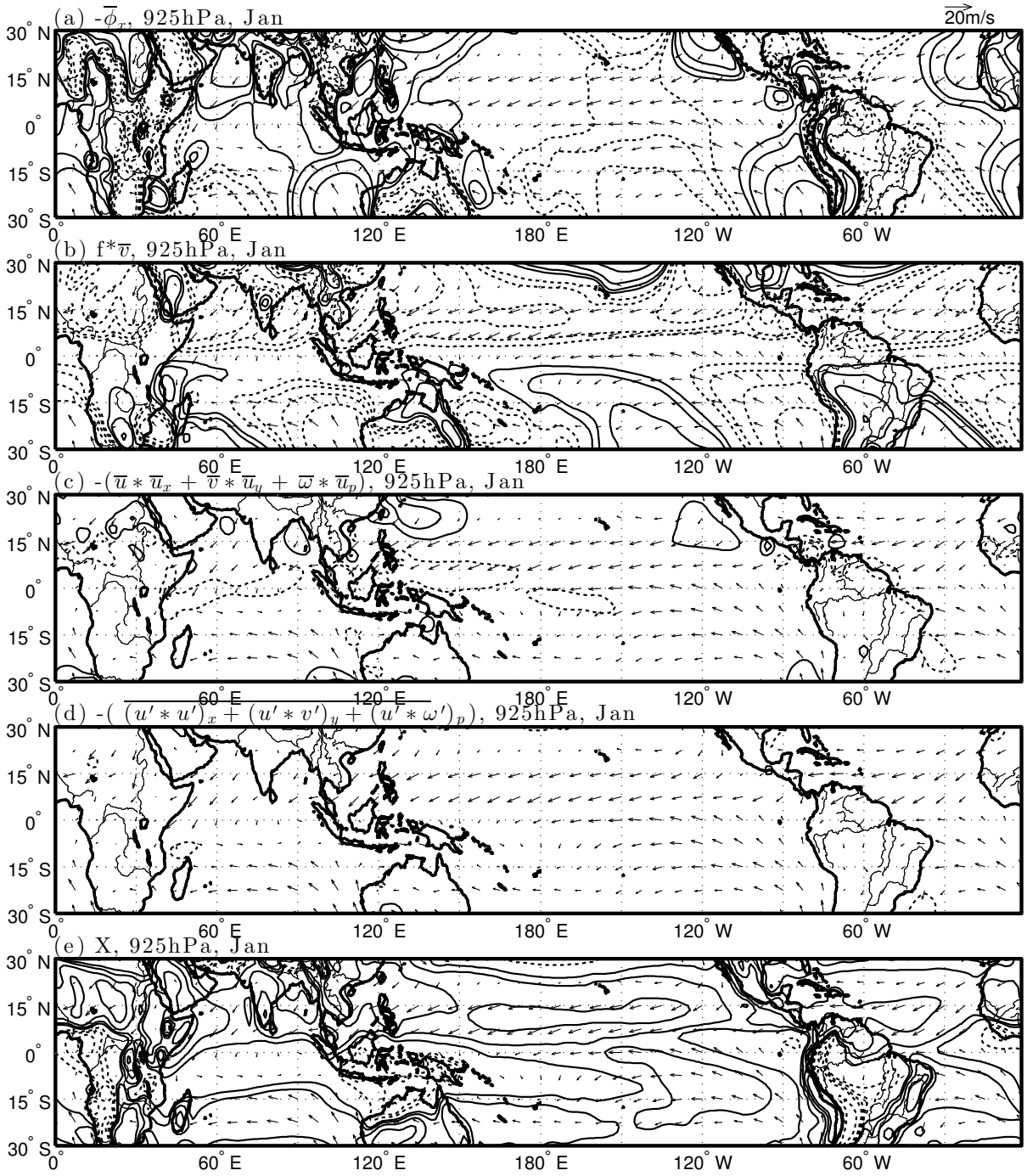

Figure 5.5: Multiple year mean January zonal momentum budget on the 925hPa pressure level (contours). The contour values are [-6.4 -1.6 -0.8 -0.4 -0.2 0.2 0.4 0.8 1.6 6.4]$\times 10^{-4} m\, s^{-2}$. Solid and dashed lines represent positive and negative values, respectively. Vectors denote winds on the pressure level. In order to focus on large scale features, the traditional 1-2-1 low pass filter is applied twice in both dimensions for each contour field.

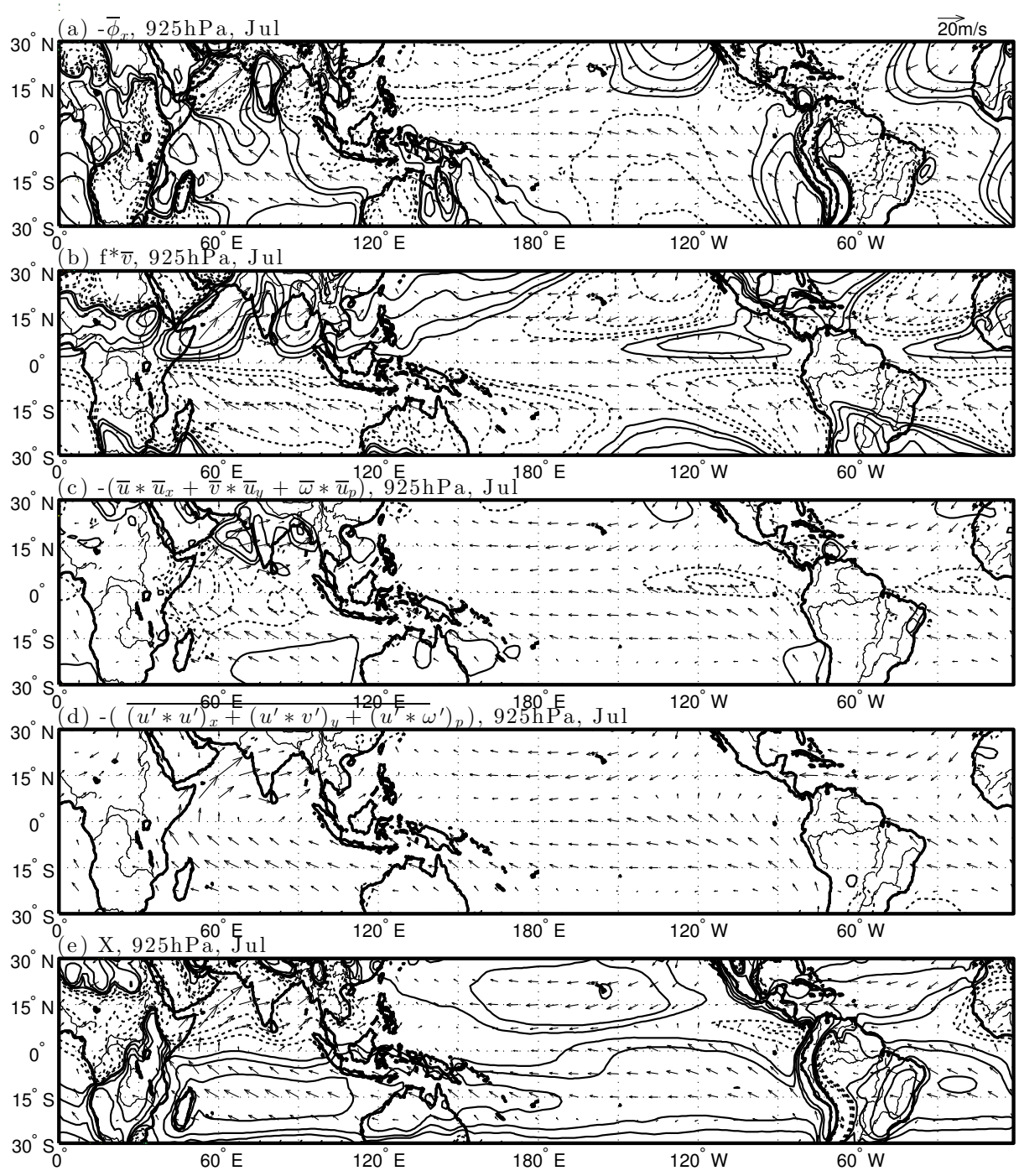

Figure 5.6: Same as Fig. 5.5 except for July.

those of the dominant terms. Instead, the nonlinear advection term joins the dominant terms group, with an RMS value of $1.1 \times 10^{-4} m\,s^{-2}$. The transient eddy force is as weak as the residual force in magnitude. In July, the boundary between the dominant terms and the minor terms is not as clear as in January. The top two forces in terms of magnitude are the Coriolis force (Fig. 5.8(b)) and the pressure gradient forces (Fig. 5.8(a)), with RMS values of $1.3 \times 10^{-4} m\,s^{-2}$ and $9.6 \times 10^{-5} m\,s^{-2}$ respectively. The bottom two forces in magnitude are the transient eddy force (Fig. 5.8(d)) and the residual force (Fig. 5.8(e)), with RMS values of $2.2 \times 10^{-5} m\,s^{-2}$ and $1.4 \times 10^{-5} m\,s^{-2}$, respectively. The nonlinear advection term (Fig. 5.8(c)) lies just between the two extremes, with an RMS value of $7.0 \times 10^{-5} m\,s^{-2}$. So the approximate zonal momentum balance at 200hPa in July is among the pressure gradient force, the Coriolis force and the nonlinear advection term. The transient eddy force and the residual force can in general be neglected.

5.4 Zonal momentum balance near the equator

The results in the above section show that, in both the atmospheric boundary layer and the upper level troposphere, the Coriolis force is among the dominant terms in the zonal momentum balance. However, the Coriolis force will almost disappear near the equator no matter how strong the meridional flow is. Therefore the zonal momentum balance regime near the equator must be different from that elsewhere in the tropics.

Fig. 5.9 shows the January zonal momentum balance in the longitude-height cross section, with each term averaged between 5^0S and 5^0N. In the upper free troposphere, the nonlinear advection term is important at most longitudes to balance the pressure gradient force while the influences of the other two forces are constrained within specific longitude intervals. For example, the transient eddy force contributes to the deceleration of westerlies around 180^0 and 130^0W while the residual force (dominated by CMT) contributes to the deceleration of the easterlies to the west of 160^0E (the west upper branch of the Walker Circulation). Within the ABL, the friction balances the pressure gradient force over all longitudes while the transient eddy force can be neglected. The nonlinear advection term has large values between 30^0E and 120^0E , indicating its influence can not

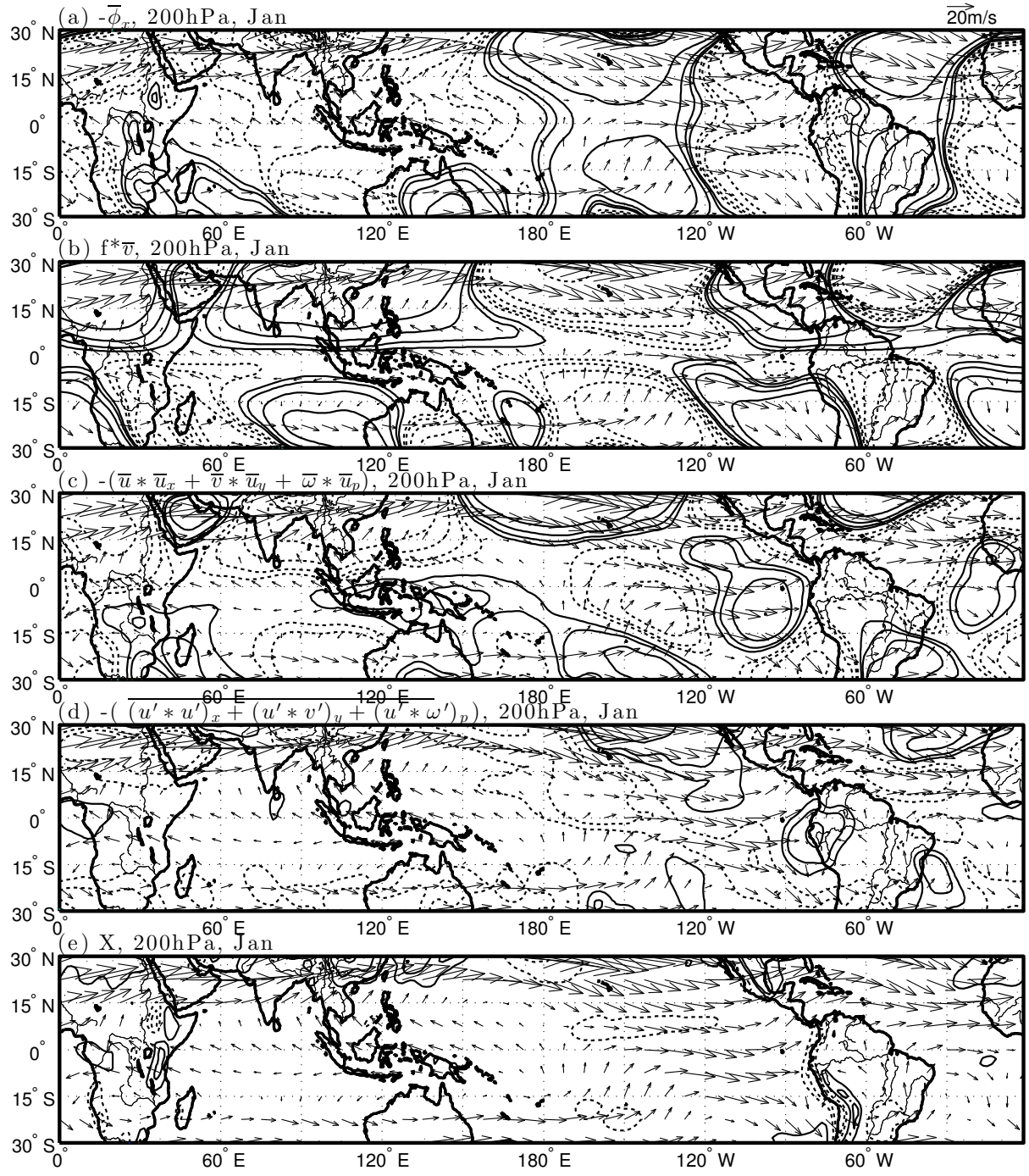

Figure 5.7: Same as Fig. 5.5 except on the 200hPa pressure level.

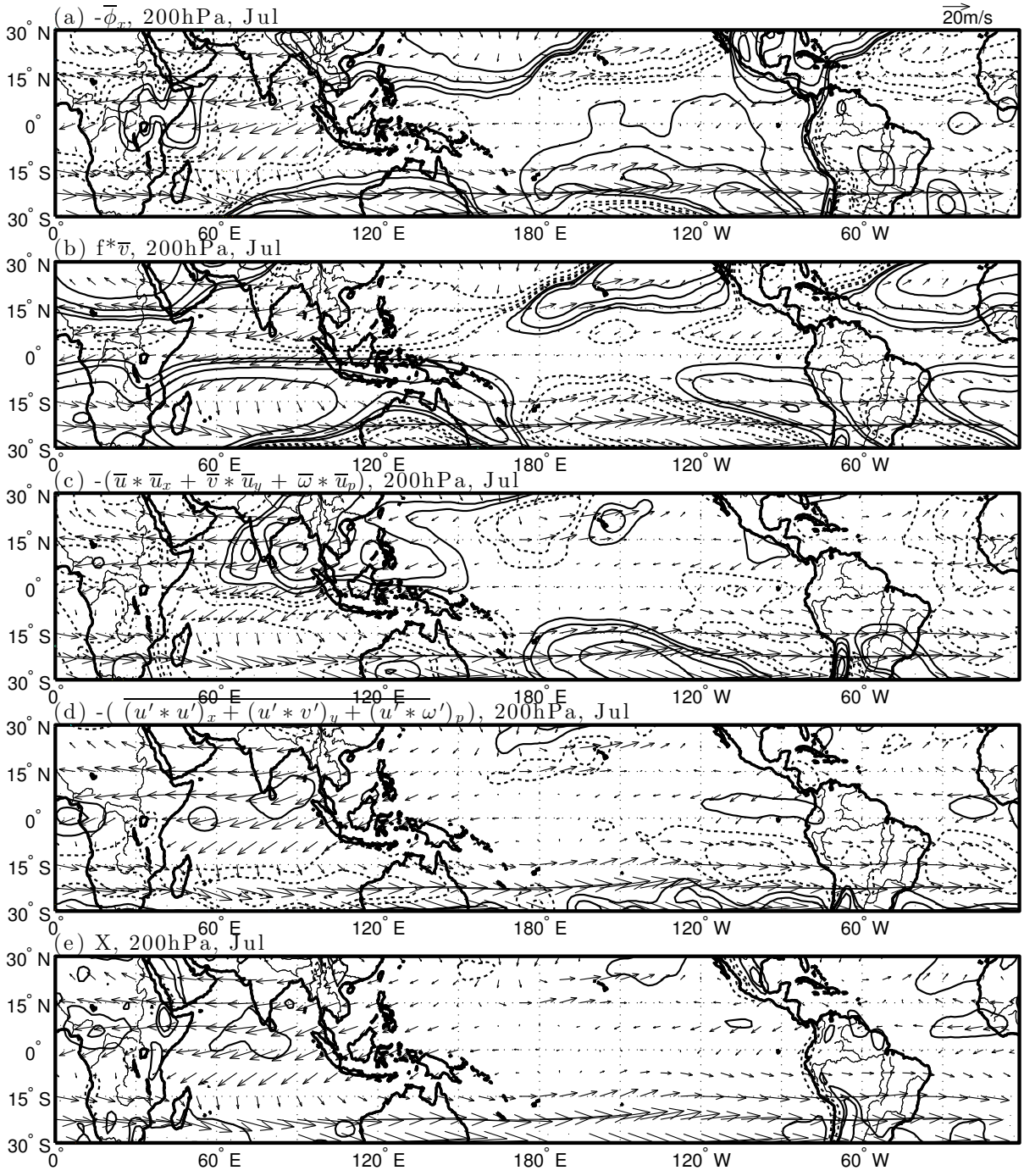

Figure 5.8: Same as Fig. 5.5 except on the 200hPa pressure level and for July.

be ignored in these regions.

The July zonal momentum balance in the longitude-height cross section (Fig. 5.10) shares similar features to that in January, but with two major differences. First, the nonlinear advection term becomes much stronger near 50^0E in the ABL, associated with the Somali Jet . Second, the transient eddy force becomes weak almost everywhere and there are no regions of large values as in the January case. This can be explained, at least partly, by the fact that the easterlies are prevalent at all longitudes in July and prevent the propagation of middle latitude eddies into the equatorial regions.

5.5 Zonal mean zonal momentum balance

Another case that must differ from the general zonal momentum balance is the zonal mean zonal momentum balance, for which the pressure gradient force becomes zero and the Coriolis force must be balanced by other terms in the zonal momentum equation.

5.5.1 The global zonal momentum balance

One of the most prominent features of the tropical circulation is that the upper level zonal mean flows are often dominated by easterlies. Based on the analysis of the zonal mean zonal momentum balance in the latitude-height cross section in January and July, the zonal mean zonal momentum balance in the tropics is among the Coriolis force ($[f\overline{v}]$), the meridional advection ($-[\overline{v}\overline{u}_y]$) and the residual force ([X]). The transient eddy force is weak in the tropics and is anyway positive in the equatorial upper troposphere (Fig. 5.11(a) and (d)), meaning it decelerates the easterlies and so can not be responsible for maintaining the easterlies in the equatorial upper troposphere. The residual force is important within the ABL and also has positive values around the equatorial upper troposphere easterlies (Fig. 5.11(b) and (e)), which means the residual force is also not responsible for the maintenance of the equatorial upper troposphere easterlies. Combining the Coriolis force and the meridional advection terms gives a term proportional to the advection of the absolute angular momentum shown in Fig. 5.11(c) and (f). Although not as strong in the tropical upper troposphere as in the ABL, its negative maximum lies in the middle of the upper troposphere easterly band, indicating the easterlies are

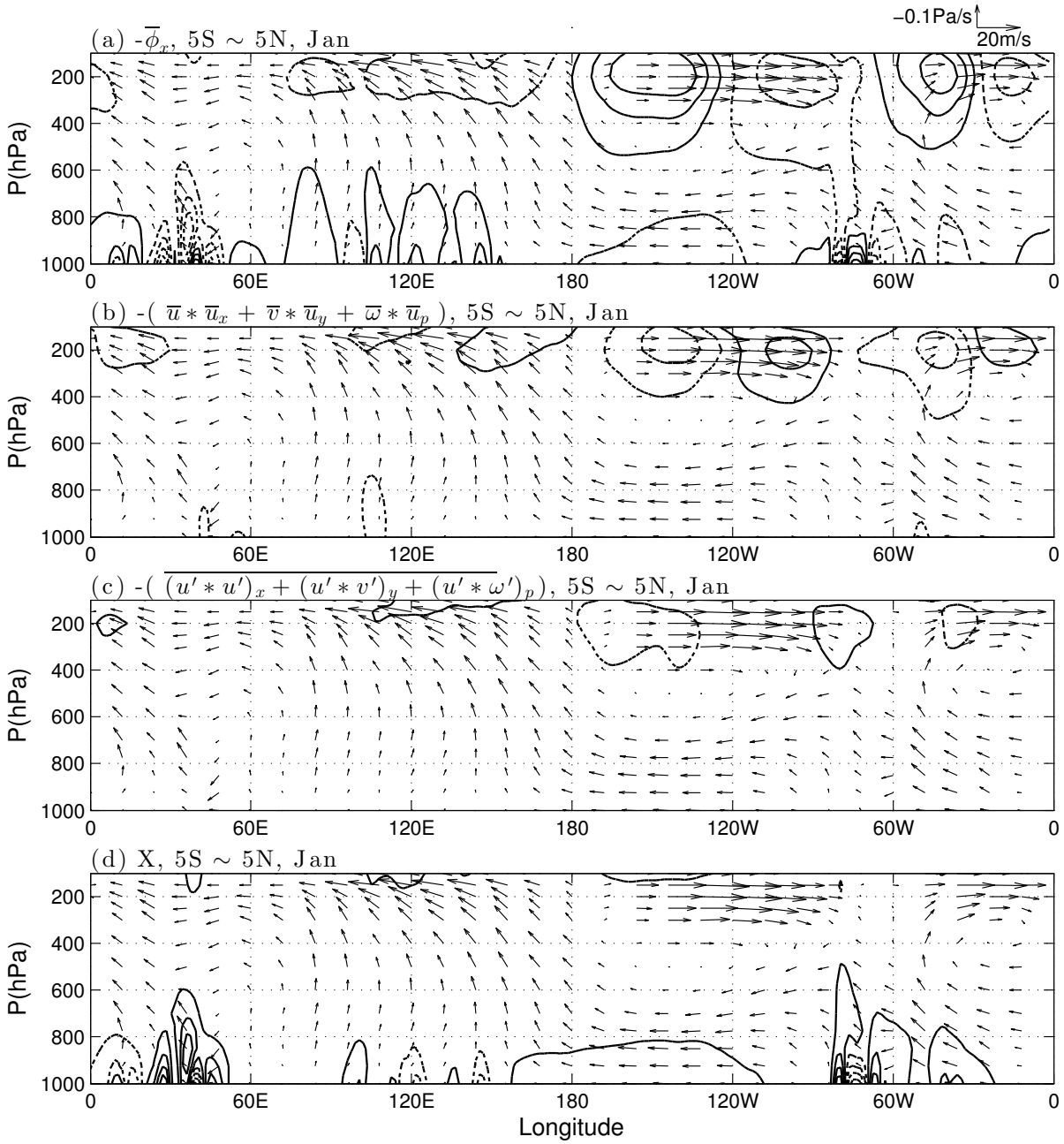

Figure 5.9: Multiple year mean January zonal momentum budget on the longitude-pressure cross section averaged between 5^0S to 5^0N (contours). Solid and dashed lines represent positive and negative values, respectively. The smallest positive contour value is $2 \times 10^{-5} m\, s^{-2}$ and the contour interval is $4 \times 10^{-5} m\, s^{-2}$. Vectors denote circulation on the longitude-pressure cross section. In order to focus on large scale features, the traditional 1-2-1 low pass filter is applied twice in both dimensions for each contour field.

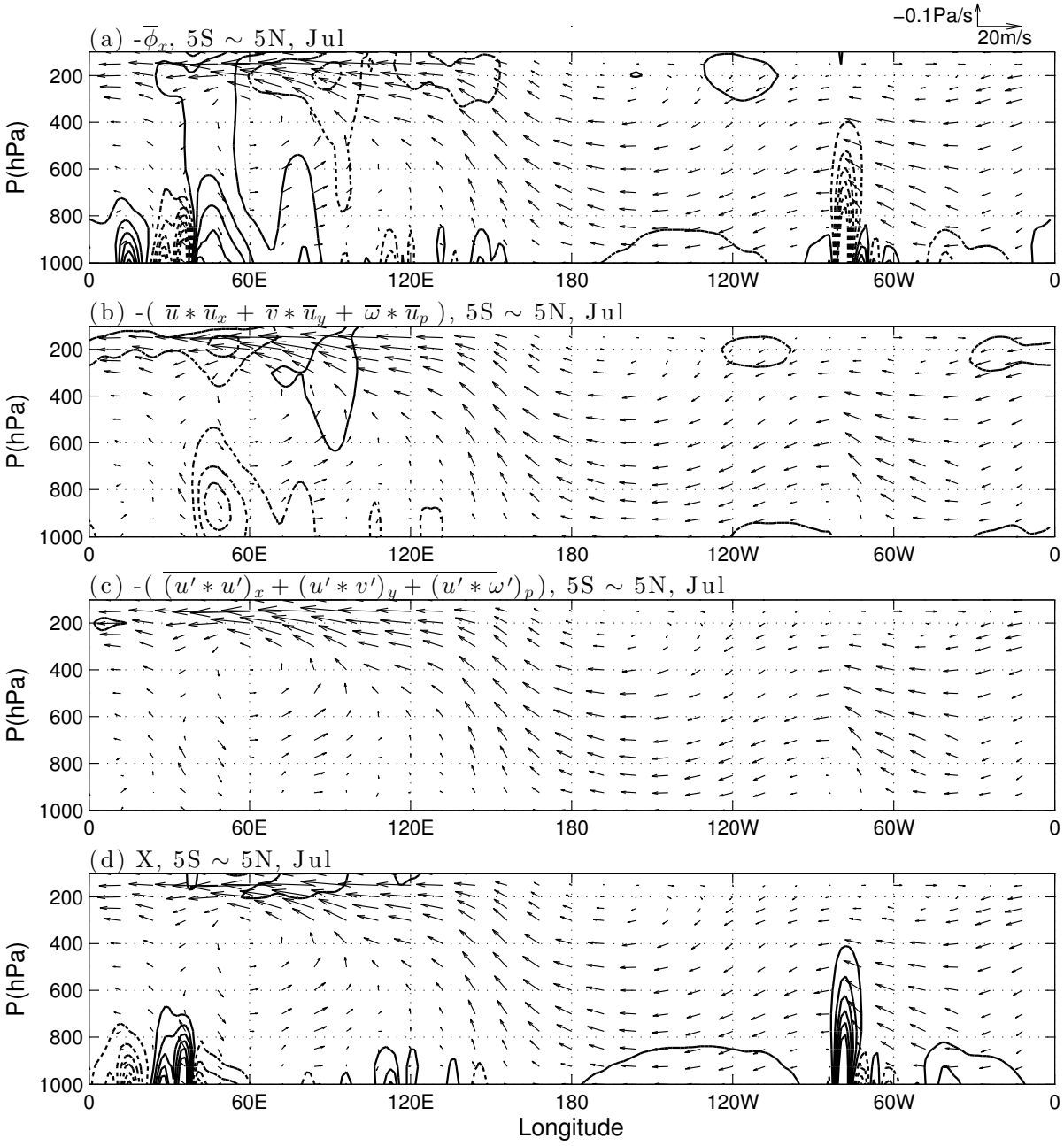

Figure 5.10: Same as Fig. 5.9 except for July.

maintained by absolute angular momentum advection.

There are two major differences between January and July. First, the equatorial upper troposphere easterlies in July are much stronger than those in January. Second, and consistently, the easterly acceleration by the absolute angular momentum advection is also stronger in July than in January. This co-variability between the strength of the easterlies and the absolute angular momentum advection acceleration is consistent with the idea that the advection of absolute angular momentum is responsible for the maintenance of the equatorial upper troposphere easterlies. It should also be pointed out that the absolute angular momentum advection terms as shown in Fig. 5.11(c) and (f) are nonlinear and the zonal averages cover the contributions from both the zonal-mean flow ($[\overline{v}](f - [\overline{u}]_y)$) and the stationary eddies ($-[\overline{v}^*\overline{u}^*_y]$). Further analysis reveals that the absolute angular momentum advection is dominated by the zonal-mean part and the stationary eddy influence is secondary and is actually decelerating the easterlies (not shown here). Therefore, it is the advection of the absolute angular momentum associated with the cross-equatorial zonal mean Hadley circulation that is responsible for the maintenance of the equatorial upper troposphere easterlies.

5.5.2 Momentum balance over the Asian monsoon longitudes

Because the absolute angular momentum advection in the tropical upper troposphere is proportional to the meridional flow, or the cross-equatorial Hadley circulation, and the strength of the Hadley circulation in July mainly comes from the Asian monsoon contribution, we examine the zonal momentum balance averaged over the Asian monsoon longitudes alone. Unlike the global zonal mean case, the pressure gradient force becomes important and joins the absolute angular momentum advection as the major accelerating force for the easterlies over the Asian monsoon region. Fig. 5.12(a), (b), (c) and (d) show these two accelerating forces in January and July zonally averaged over the longitudes between 60^0E and 150^0E, which cover the Asian monsoon longitudes. In January, the acceleration by the absolute angular momentum advection is too weak to maintain the equatorial upper troposphere easterlies. Instead, the acceleration by the pressure gradient force is much stronger and contributes to the maintenance of the easterlies. In July, the

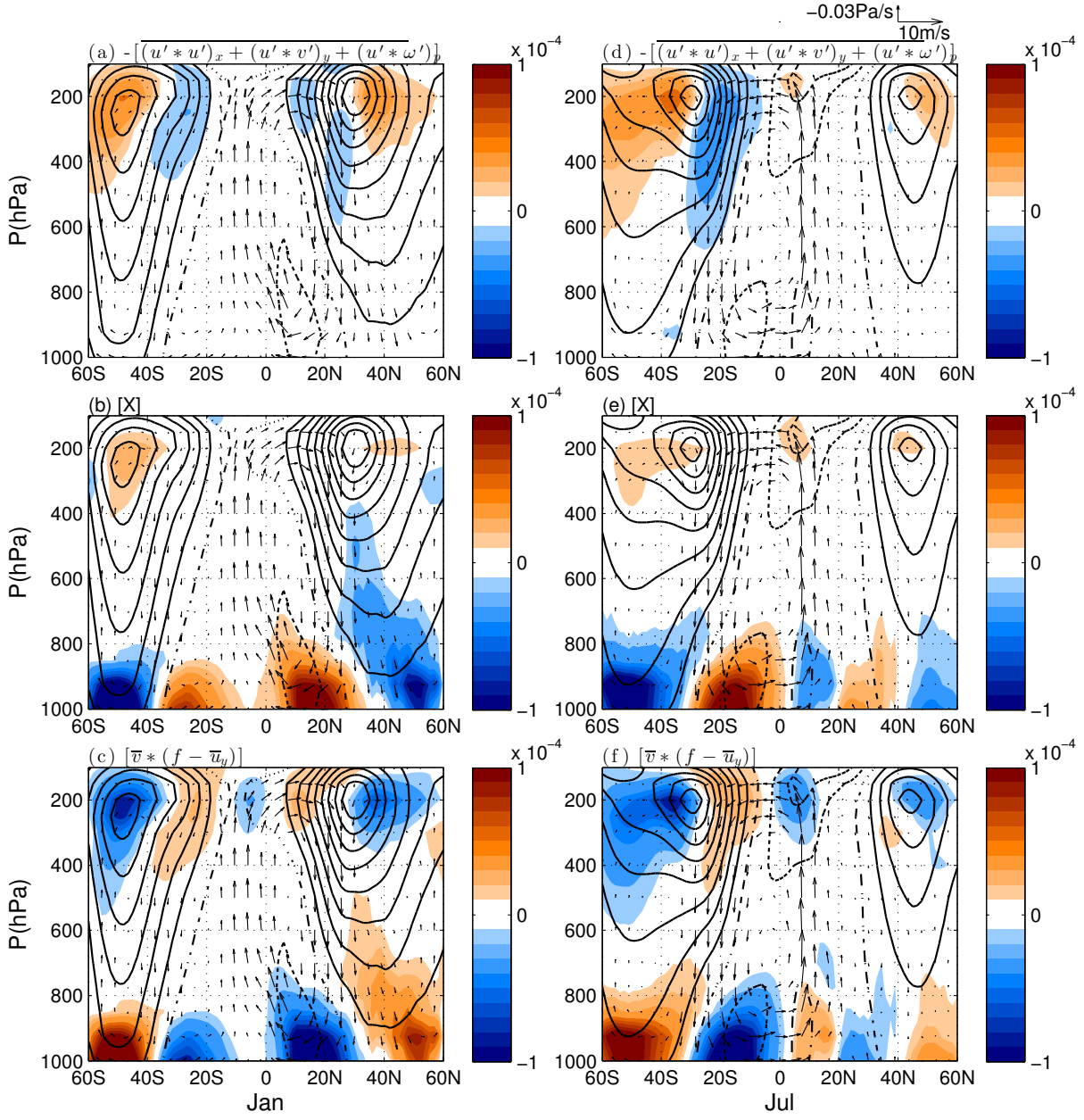

Figure 5.11: Multiple year mean zonal momentum budget on the latitude-pressure cross section zonally averaged over all longitudes (colors). (a) (b) and (c) are for January and (d) (e) and (f) are for July. Vectors denote the zonally averaged circulation on the latitude-pressure cross section. Contours represent the zonal mean zonal flow and the interval is $5m\,s^{-1}$. Solid, dotted and dashed lines correspond to positive, zero and negative values, respectively.

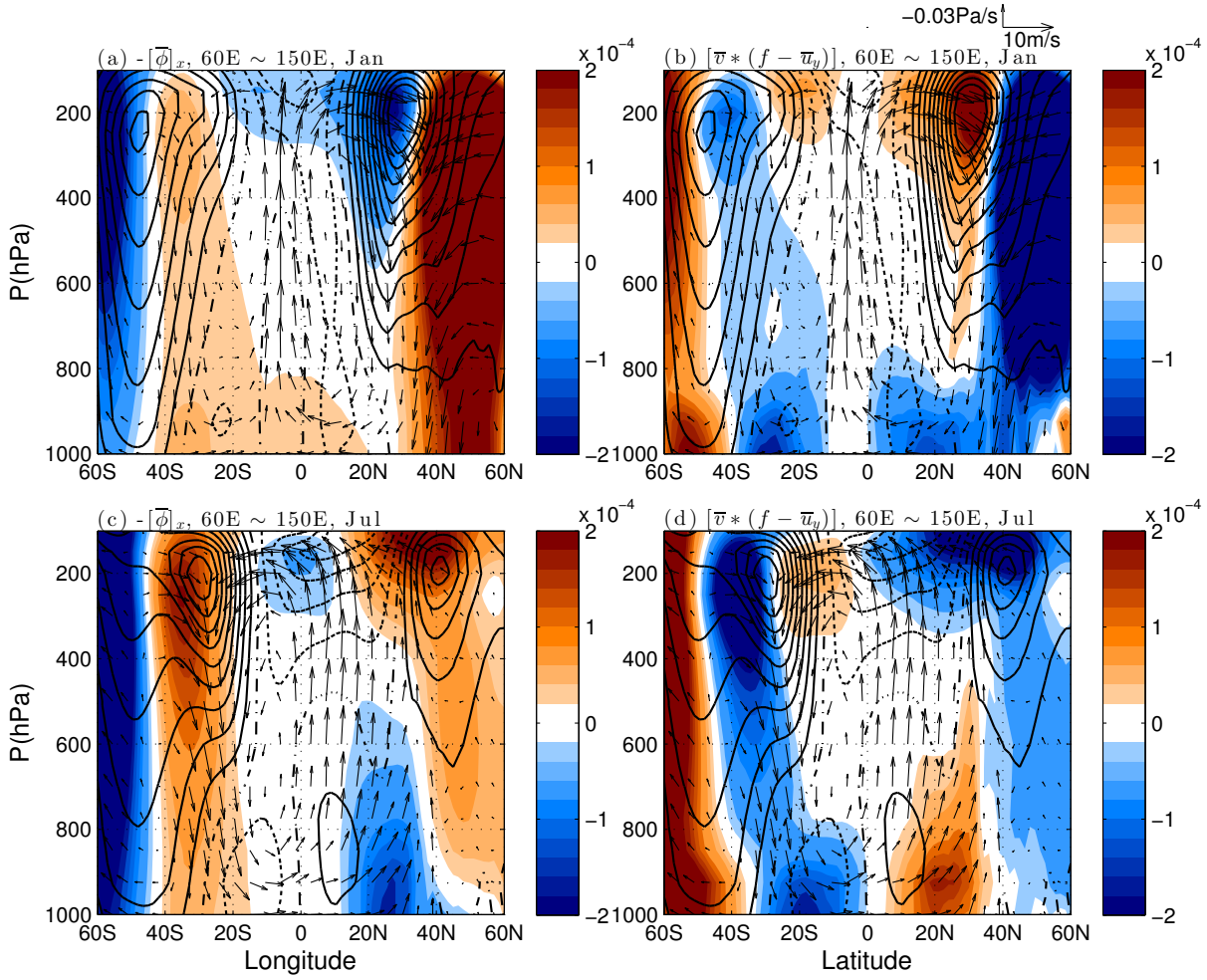

Figure 5.12: Similar to Fig. 5.11 except that the zonal momentum budget terms are averaged over the Asian monsoon region instead of the whole longitudes.

magnitude of the acceleration by the pressure gradient force does not change much from that in January. However, the easterlies become significantly stronger than those in January because the absolute angular momentum advection contributes strongly to the easterly acceleration. Hence the seasonal variability of the equatorial upper troposphere easterlies over the Asian monsoon region can be explained by the seasonal variability of the absolute angular momentum advection.

5.5.3 Momentum balance over the east Pacific longitudes

Another longitude range of particular interest is the east Pacific between 130^0W and 80^0W, where the tropical upper troposphere winds change from easterlies in July to westerlies in January. In July, the absolute angular momentum advection maintains the tropical upper troposphere easterlies (Fig. 5.13(d)) while the pressure gradient force actually decelerates the easterlies (not shown). In January, the pressure gradient force still decelerates tropical upper troposphere flows, although the flows become westerlies instead of easterlies. At the same time, however, the absolute angular momentum advection becomes extremely weak in the tropical upper troposphere (Fig. 5.13(b)) so it can not maintain the westerlies. So which force is now responsible for maintaining the westerlies in the tropical upper troposphere over the east Pacific? Fig. 5.13(a) shows that it is the zonal momentum advection by the zonal flow, or the zonal inertial force. This is also confirmed by the the 200hPa momentum budget (Fig. 5.7(c)), which shows the force of the zonal momentum advection by the zonal flow is positive over the east Pacific.

5.6 Equivalent Rayleigh friction

In previous sections, it has been shown that the nonlinear advection term is often important in the upper free troposphere and even in some regions within the ABL (e.g. in the Asian summer monsoon region). This poses a challenge to using linear dynamics in the widely-used simple tropical atmospheric models. There is, however, the possibility that linear models with Rayleigh friction are still viable if the nonlinear advection term and all other terms not included in the linear dynamics behave collectively in a way that can be approximated by the equivalent Rayleigh friction form. As described in equation (5.7), the equivalent Rayleigh friction coefficients can be estimated at each grid point and the correlation coefficient can be used to assess the appropriateness of the Rayleigh friction approximation (Lin et al., 2008).

Fig. 5.14 shows the equivalent Rayleigh friction coefficients at each grid point on the 925hPa and 200hPa pressure levels in January and July. Fig. 5.14(a) and (b) show that the Rayleigh friction coefficients on the 925hPa pressure level are not uniform over the

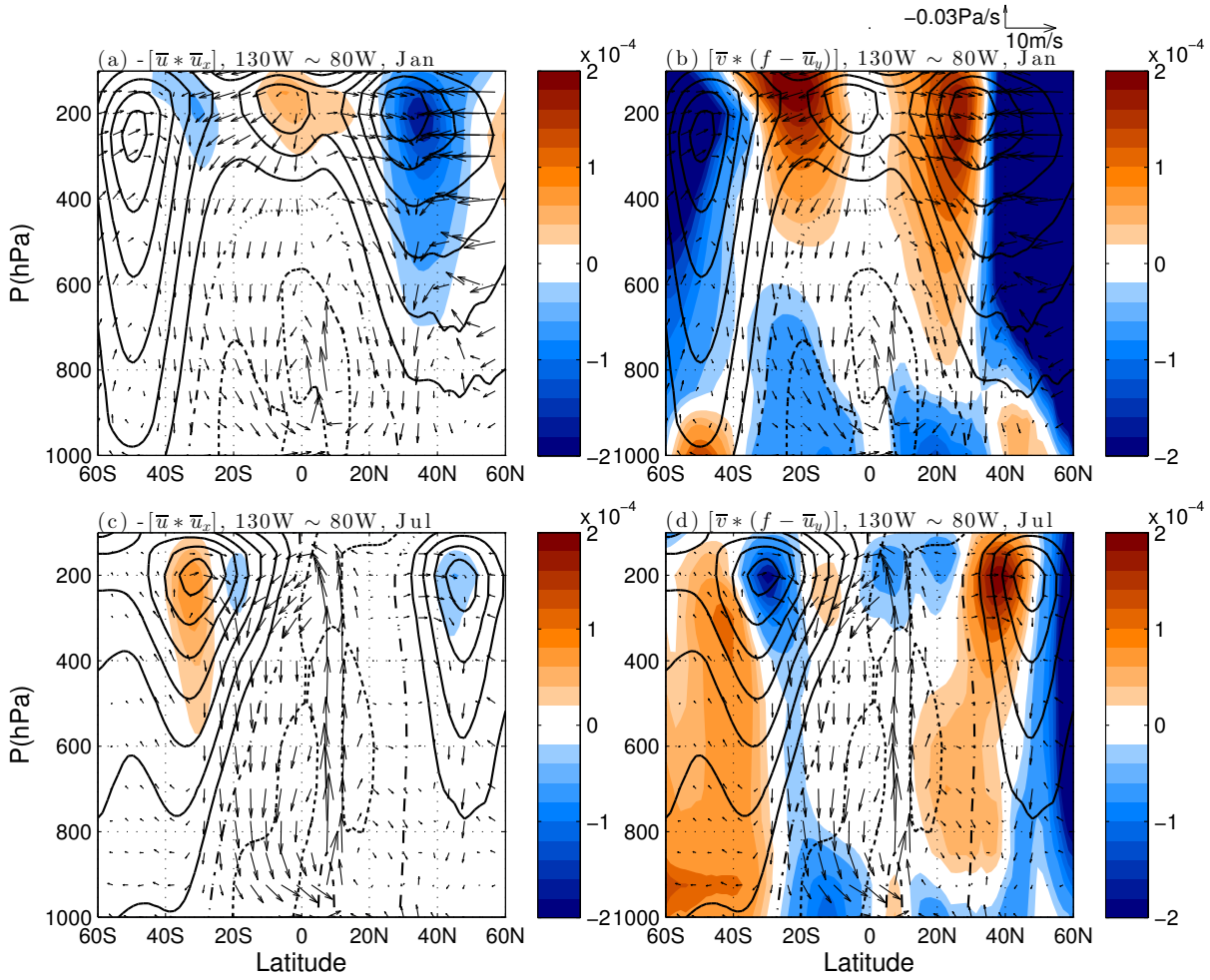

Figure 5.13: Similar to Fig. 5.11 except that the zonal momentum budget terms are averaged over the east Pacific region instead of all longitudes.

tropics. The coefficient is much larger over land than over the ocean. Regressing the monthly Rayleigh friction on the zonal flow for all the grid points over all the multiple years yields a single Rayleigh friction coefficient and a corresponding friction time scale in January (July), which is around 1.2 (1.1) days. For comparison, the Rayleigh friction time scale for the land as a whole and for ocean as a whole in January (July) is 0.5 (0.4) days and 1.5 (1.5) days, respectively; i.e. the average friction coefficient is three times stronger over land.

Although the linear equivalent Rayleigh friction model does an excellent job in the ABL, it does not perform as well in the tropical upper troposphere. Fig. 5.14(c) and (d) show the Rayleigh friction coefficients on the 200hPa pressure level in January and July. The Rayleigh friction coefficients show more inhomogeneity than those on the 925hPa pressure level and significant areas over the east Pacific and the east Atlantic in January even show negative friction coefficients and Rayleigh friction would not be expected a priori to be a good approximation of its effects. There are locations where the zonal inertial acceleration is important as discussed in section 5.5. Away from these areas, however, the linear equivalent Rayleigh friction model seems to work better (e.g. the Walker circulation to the west of $120W$ in January). Another example is the Asian monsoon circulation, in which the linear equivalent Rayleigh friction model seems to work well and the friction coefficients are in general positive.

Why does the equivalent Rayleigh friction work well in some specific regions but fail in other regions in the upper troposphere? As discussed in previous sections, the nonlinear advection terms are the dominant terms to balance the pressure gradient force and the Coriolis force in the upper troposphere. In order to make the equivalent Rayleigh friction work, the nonlinear advection terms should decelerate the local flow in the zonal direction, which is equivalent to saying that the flow, along its stream line, should increase in absolute zonal velocity. There are two types of regions in the upper troposphere satisfying this condition: 1) flows nearby the divergent outflow regions of the Asian monsoon and the North American monsoon in July and of the Walker Circulation in January ; 2) cross-equator flows after turning their zonal direction (e.g. the Asian monsoon flows to the south

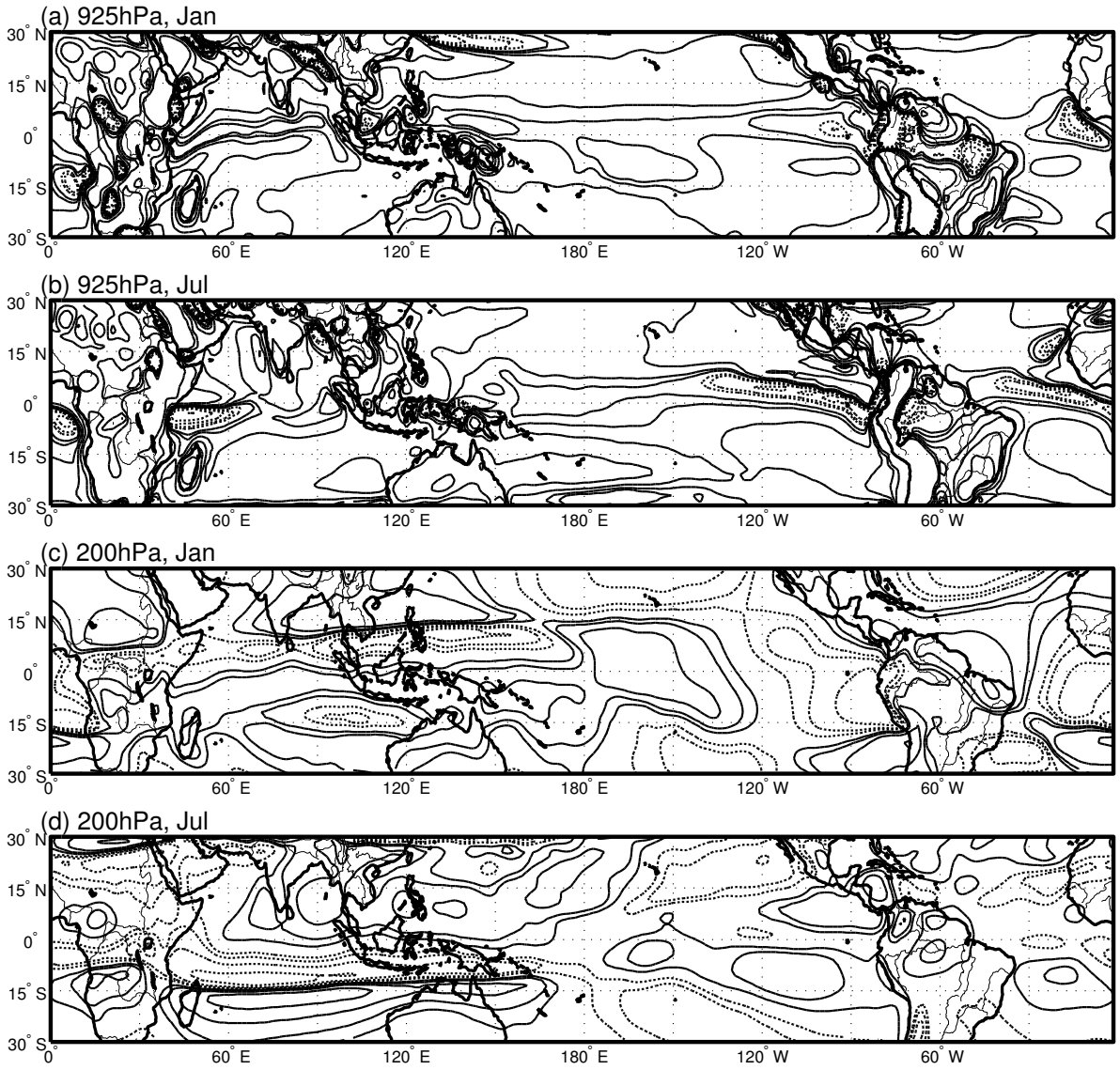

Figure 5.14: Rayleigh friction coefficient calculated based on regression. The contour values are [-6.4 -3.2 -1.6 -0.8 -0.4 -0.2 0.2 0.4 0.8 1.6 3.2 6.4]$\times 10^{-5} s^{-1}$. Solid and dashed lines represent positive and negative values, respectively. In order to focus on large scale features, the traditional 1-2-1 low pass filter is applied twice in both dimensions for each contour field.

of 15S in July). Correspondingly, there are also two types of upper troposphere upper troposphere regions that do not satisfy the condition. i.e. regions of zonal convergence such as over the tropical east Pacific and east Atlantic and cross-equator flows before turning their zonal direction such as the Asian monsoon flows between 0 and 15S .

5.7 Conclusions and discussion

ERA-Interim reanalysis daily data have been used in this study to examine the three-dimensional zonal momentum balance of the tropical atmospheric circulation in both January and July, which represent the mature global monsoon months in the southern hemisphere and northern hemisphere, respectively. We also did all the calculations with the NCEP/NCAR reanalysis dataset (Kalnay et al., 1996) and find no significant difference between the two reanalysis datasets. The following conclusions have been reached:

- In the atmospheric boundary layer (ABL), the pressure gradient force, the Coriolis force and surface friction are the dominant terms in the zonal momentum balance. The nonlinear advection term is important only in the Asian summer monsoon region. Linear dynamics is a good approximation for the zonal momentum equation within the ABL yet the equivalent Rayleigh friction coefficient is not spatially uniform. In general, the coefficient over the land is three times larger than that over the ocean.

- In the upper troposphere, the dominant terms in the zonal momentum balance are the pressure gradient force, the Coriolis force and the nonlinear advection term. The linear dynamics approximation is not as good as that in the ABL but still is applicable in regions such as the Walker Circulation and the Asian monsoon region.

- Near the equator, where the Coriolis force is small, the zonal momentum balance is in general among the pressure gradient force, nonlinear advection and the residual force (dominated by friction in the ABL and by the CMT in the free troposphere). The transient eddy force is in general secondary but becomes important in the longitudes with upper troposphere equatorial westerlies in January.

- The absolute angular momentum advection associated with the cross-equatorial Hadley circulation plays an important role in maintaining the global-zonal-mean equatorial upper troposphere easterlies and its change of strength between January and July also explains the intensity of the easterlies. The absolute angular momentum advection also has an influence on regional zonal flows, i.e. it strengthens the Asian monsoon easterlies from January to July and shifts the equatorial upper troposphere flow over the east Pacific from westerlies in January to easterlies in July.

Lin et al. (2008) showed that the mechanical damping in the Gill-type models for the annual mean Walker circulation consists of two sources: the nonlinear advection and the residual force. Our study shows that the transient eddy force is also important in the east upper branch of the Pacific Walker circulation in January when the westerlies dominate there and allow mid-latitude eddies to propagate to the equator. The transient eddy force might be neglected in the annual mean zonal momentum balance but can be important in particular months. Schneider and Bordoni (2008) demonstrated that eddy-mean flow interaction plays an important role in the seasonal cycle of the Hadley circulation, which also implies that the transient eddy force, although negligible in the annual mean circulation, can be important in the seasonal cycle.

The mechanisms for the dominance of the easterlies in the equatorial upper troposphere have been explored in Lee (1999) and Kraucunas and Hartmann (2005). Although the stationary wave associated with zonal asymmetric heating tends to drive a super rotational flow (westerlies) over the equatorial upper troposphere, the easterly acceleration associated with the cross-equatorial Hadley circulation often overwhelms this effect and drives the observed dominant easterlies. Our study confirms this point and shows that the absolute angular momentum advection indeed maintains the zonal mean easterlies in the equatorial upper troposphere while the stationary wave force has a westerly tendency but is much smaller. As the absolute angular momentum advection arises from the cross-equatorial Hadley circulation, which is controlled by the off-equator heating (Lindzen and Hou, 1988), the easterly acceleration by the absolute angular momentum advection varies

seasonally as the heating center moves north and south. Because the cross-equatorial Hadley circulation is stronger in the northern hemisphere summer than in the southern hemisphere summer, the easterly acceleration by the absolute angular momentum advection is stronger in the northern hemisphere summer and results in more intense upper troposphere equatorial easterlies. Although the westerly acceleration by the equatorial stationary waves has a similar pattern of seasonal variability as the easterly acceleration by the zonal mean meridional flow (Dima et al., 2005), its magnitude is much smaller than the easterly acceleration. Therefore, the prevalence of the tropical upper troposphere easterlies and the variability of their strength are determined by the zonal mean Hadley circulation and the associated absolute angular momentum advection.

We also extend this idea to the maintenance and seasonal variability of regional zonal flows and find that the variability of the strength of the Asian monsoon region easterlies and the shift of the direction of zonal flow over the east Pacific between January and July can also be explained by the variability of the absolute angular momentum advection associated with the cross-equatorial Hadley circulation. This is relevant to the interaction of the meridional Hadley circulation and the zonal Walker circulation, the two preeminent circulation systems in the tropics. Future work will examine this interaction on other time scales and its impact on climate in the tropics and extra-tropics.

As revealed in our study, the nonlinear advection term is in general negligible in the zonal momentum balance of the boundary layer but emerges as a major component over the Asian summer monsoon region. This is relevant to the dynamics of the monsoonal circulation, and can even potentially impact the variability of convection and precipitation in this region through the atmospheric dynamical instability (Tomas and Webster, 1997; Boos and Emanuel, 2009). Tomas and Webster (1997) noticed that organized convection appears off the equator in the summer hemisphere and not necessarily collocated with the warmest SST when there is a substantial cross-equatorial surface pressure gradient. This is the case for the Asian summer monsoon. In their explanation, they proposed a hypothesis that, in addition to the thermaldynamical control from SST, the inertial instability of the boundary layer atmospheric circulation plays an important role in regulating

the location and strength of convection. The region between the zero absolute vorticity contour in the summer hemisphere and the equator is inertially unstable and therefore favors convection even though the SST is not highest there. Boos and Emanuel (2009) (Fig. 11) also demonstrated that the inertial instability is closely related to the seasonal abrupt intensification of the Somali Jet. These results indicate that our study of zonal momentum balance is also relevant to the understanding of hydroclimate over the Asian monsoon region, including East Africa.

CHAPTER 6

Conclusions

There has been increased frequency and intensity of droughts over East Africa in recent decades while the majority of climate models from CMIP3/5 project that precipitation will increase in a warming climate forced by greenhouse gases (GHGs), suggesting the current drying condition will potentially be recovered in the future. To address the question of whether the current dry condition will continue or there will be recovery, we begin by studying decadal variability of the hydroclimate of East Africa and found that the drying trend of the East African long rains in recent decades most likely arose from natural decadal variability and is not of anthropogenic origin. The decadal variability of the East African long rains can be explained by the decadal variability of SST over the Pacific Ocean, with dry phases associated with positive SST anomalies over the western tropical Pacific and negative anomalies over the central and eastern tropical Pacific (La Niña-like).

We further assess performance of both SST-forced and fully coupled models in simulating the observed decadal variability of the long rains as well as the more fundamental aspect of the annual cycle of rainfall. It is found that the SST-forced ECHAM4.5 and ECHAM5 are able to capture the precipitation climatology, the SST anomaly pattern associated with decadal variability and the drying trend in recent decades. However, not all the models perform well (e.g. CCM3.6 is not even able to capture the recent drying trend). The SST-forced models of the CMIP5 AMIP experiments also capture the climatology of the East Africa precipitation, although with varying skill. The simulated East African long rains anomaly, which is only available from the models after 1979, does capture the recent observed drying trend in the multimodel mean and the associated SST anomaly pattern is consistent with the observed. Despite the good performance of the AMIP runs of the CMIP5 models, the multimodel mean of the fully coupled models of the CMIP5 historical experiment underestimates the East African long rains and overestimates the short rains with a considerable range of performance among the individual

models. The multimodel mean of the precipitation anomalies in the coupled models shows a weak wetting trend since 1950 that is much smaller than the internal variability. Hence the long rains drying trend in recent decades is inconsistent with the models' response to radiative forcing. Moreover, the SST anomaly pattern associated with the long rains in the coupled models has large discrepancies with the observations. Our results suggest caution in interpreting projections of East African precipitation from CMIP5 or in applying the relationship between East African precipitation and the SST spatial pattern in paleoclimate studies by appealing to coupled climate models. The above work is covered in Chapter 2.

Motivated by the challenges faced by the coupled models in simulating the correct rainfall annual cycle over East Africa, as well as the uniqueness of the bimodal annual cycle and comparatively dry annual mean climatology, we then use the ERA-Interim Re-Analysis data to analyze the associated annual cycles of atmospheric convective stability, circulation and moisture budget. The atmosphere over East Africa is found to be convectively stable year-round but with an annual cycle dominated by the surface moist static energy (MSE), which is in phase with the precipitation annual cycle. Throughout the year, the atmospheric circulation is dominated by a pattern of convergence near the surface, divergence in the lower troposphere and convergence again at upper levels. Consistently, the convergence of the vertically integrated moisture flux is mostly negative across the year, but becomes weakly positive in the two rainy seasons. It is suggested the semi-arid/arid climate in East Africa and its bimodal precipitation annual cycle can be explained by the ventilation mechanism, in which the atmospheric convective stability over East Africa is controlled by the import of low MSE air from the relatively cool Indian Ocean off the coast. During the rainy seasons, however, the off-coast sea surface temperature (SST) increases (and is warmest during the long rains season) and consequently the air imported into East Africa becomes less stable. This is covered in Chapter 3.

In Chapter 4, we directly investigate the coupled model induced bias of the East African rainfall annual cycle found in CMIP3/5 that overestimates the OND rainfall and underestimates the MAM rainfall, by comparing the historical run and the AMIP run for

each model, with particular emphasis on the MRI-CGCM3. The framework of convective instability (CI) and moist static energy (MSE) are shown to be able to link this bias to other tropical or global scale biases that have been found in previous studies. It is found that the historical minus AMIP monthly climatology rainfall biases can be explained by the bias of convective instability (CI), which is dominated by the near surface MSE. Insufficient ocean dynamical cooling and latent flux are dominant in developing warm bias over the western Indian Ocean the late JJAS and early OND and can explain the over all wet bias over East Africa during the OND rainy season, while insufficient short wave radiation and excess latent heat flux are responsible for the cold SST bias during boreal winter and spring and the consequent dry long rains bias.

To put the East African regional climate in context of the broader tropical climate and circulation and understand the circulation of the whole tropics, we analyze the zonal momentum balance of the tropical atmospheric circulation during the global monsoon mature months (January and July) in three dimensions based on the ERA-Interim reanalysis. It is found that the dominant terms in the balance of the atmospheric boundary layer (ABL) in both months are the pressure gradient force, the Coriolis force and the friction. The nonlinear advection term plays a significant role only in the Asian summer monsoon regions. In the upper troposphere, the pressure gradient force, the Coriolis force and the nonlinear advection are the dominant terms. The transient eddy force and the residual force (which can be explained as convective momentum transfer over open oceans) are secondary yet can not be neglected near the equator. Zonal mean equatorial upper troposphere easterlies are maintained by the absolute angular momentum advection associated with the cross-equatorial Hadley circulation. Equatorial upper troposphere easterlies over the Asian monsoon regions are also controllled by the absolute angular momentum advection but are mainly maintained by the pressure gradient force in January. The equivalent linear Rayleigh friction, which is widely applied in simple tropical models, is calculated and the corresponding spatial distribution of local coefficient and damping time scale are estimated from the linear regression. It is found that the linear momentum model is in general capable of crudely describing the tropical atmospheric circulation dynamics yet

the caveat should be kept in mind that the friction coefficient is not uniformly distributed and is even negative in some regions. This work is covered in Chapter 5.

Based on the findings that have been made in this thesis, we propose the following work that will potentially be conducted in the future research:

1. *Analyzing the internal variabilities.*

   Here we will extend the work of Yang et al. (2014b) by examining the East African droughts in the *piControl* and *sstClim* experiments from CMIP5. We will begin with analysis of the *piControl* pre-industrial control experiments, which will provide assessment of the internal variability of the droughts in the atmosphere-ocean coupled system in the absence of any anthropogenic or other radiative forcing. Then we will analyze the *sstClim* experiments, which are forced by climatological SSTs and sea ice imposed from *piControl* and ideal for assessing internal variability arising purely from atmosphere dynamics. We propose to address the questions of 1) whether the observed East African precipitation climatological annual cycle can be represented in the *piControl* and *sstClim* experiments; 2) whether there are decadal variabilities of droughts similar to that observed in the modern climate; 3) what the atmospheric thermal condition and circulation associated with the droughts look like; and 4) what the differences in droughts between the *piControl* and the *sstClim* experiments are given that the experiment includes an active ocean and the other does not.

2. *Investigating the natural variability over the past millennium.*

   Natural variability associated with East African droughts will be further analyzed by investigating the *past1000* experiment from CMIP5. This experiment simulates the Earth's climate during the period of 850–1850 and provides us the opportunity to assess the East African droughts resulting from purely natural forcing. The results will be compared to those in Yang et al. (2014b), where the simulations are driven by both natural and anthropogenic forcings. The proposed work here is expected to address the following questions: 1) What is the variability of East African droughts under purely natural forcing? 2) What is the difference between the

natural variability and the internal variabilities? 3) How does the natural variability differ from the variability in the past century as anthropogenic forcings emerged to be important?

3. *Conducting numerical experiments to study roles of different factors in generating the East African rainfall annual cycle.*

   It is shown in this thesis that the rainfall annual cycle over East Africa can be explained by the dynamics of sub-cloud MSE, which in turn is controlled by the off-coast SSTs and low level circulation over East Africa. We will conduct a suit of numerical experiments to isolate the influences from different factors. For example, we can set the zonal SST gradient to be zero over the Indian Ocean to look at the effect of east-west SST gradient. We can also reduce the intensity of convection over the Indo-Pacific warm pool to see if a Gill-type response can be observed over East Africa. The highlands over East Africa can be removed to examine whether the highlands cause drying or wetting of East Africa.

4. *Applying our findings to development research*

   As the wetting projections found in CMIP3/5 over East Africa are widely accepted by the development community as the foundation for climate adaptations and development policies, our findings in this thesis show that this kind of approach is potentially incorrect and might have undesired outcomes. We will communicate with the development community by showing what we have found and persuade the community to review this issue, and together with them, find an improved way to assess the future of East African hydroclimate and develop appropriate policy responses.

BIBLIOGRAPHY

Adler, R. F., et al., 2003: The version-2 Global Precipitation Climatology Project (GPCP) monthly precipitation analysis (1979-present). *J. Hydrometeor.*, **4 (6)**, 1147–1167.

Anchukaitis, K. J. and J. E. Tierney, 2013: Identifying coherent spatiotemporal modes in time-uncertain proxy paleoclimate records. *Clim. Dynam.*, **41 (5-6)**, 1291–1306.

Anyah, R. O. and W. Qiu, 2012: Characteristic 20th and 21st century precipitation and temperature patterns and changes over the Greater Horn of Africa. *Int. J. Climatol.*, **32 (3)**, 347–363.

Beltrando, G., 1990: Space-time variability of rainfall in April and October–November over East Africa during the period 1932–1983. *Int. J. Climatol.*, **10 (7)**, 691–702.

Beltrando, G. and P. Camberlin, 1993: Interannual variability of rainfall in the Eastern Horn of Africa and indicators of atmospheric circulation. *Int. J. Climatol.*, **13 (5)**, 533–546.

Berrisford, P., P. Kållberg, S. Kobayashi, D. Dee, S. Uppala, A. J. Simmons, P. Poli, and H. Sato, 2011: Atmospheric conservation properties in ERA-Interim. *Quart. J. Roy. Meteor. Soc.*, **137 (659)**, 1381–1399.

Bollasina, M. A. and Y. Ming, 2013: The general circulation model precipitation bias over the southwestern equatorial Indian Ocean and its implications for simulating the South Asian monsoon. *Clim. Dynam.*, **40**, 823–838.

Boos, W. and Z. Kuang, 2010: Dominant control of the South Asian monsoon by orographic insulation versus plateau heating. *Nature*, **463 (7278)**, 218–222.

Boos, W. R. and K. A. Emanuel, 2009: Annual intensification of the Somali jet in a quasi-equilibrium framework: Observational composites. *Q. J. R. Meteorol. Soc.*, **135 (639)**, 319–335.

Boos, W. R. and J. V. Hurley, 2013: Thermodynamic bias in the multimodel mean boreal summer monsoon. *J. Clim.*, **26**, 2279–2287.

Boos, W. R. and Z. Kuang, 2013: Sensitivity of the South Asian monsoon to elevated and non-elevated heating. *Sci. Rep.*, **3**, 1192.

Bryson, R. A. and P. M. Kuhn, 1961: Stress-differential induced divergence with application to littoral precipitation. *Erdkunde*, **15**, 287–294.

Cai, W. and T. Cowan, 2013: Why is the amplitude of the Indian Ocean Dipole overly large in CMIP3 and CMIP5 climate models? *Geophys. Res. Lett.*, **40 (6)**, 1200–1205.

Camberlin, P. and R. E. Okoola, 2003: The onset and cessation of the "long rains" in eastern Africa and their interannual variability. *Theor. Appl. Climatol.*, **54**, 43–54.

Camberlin, P. and N. Philippon, 2002: The East African March–May rainy season: Associated atmospheric dynamics and predictability over the 1968–97 period. *J. Climate*, **15 (9)**, 1002–1019.

Camberlin, P. and J. Wairoto, 1997: Intraseasonal wind anomalies related to wet and dry spells during the "long" and "short" rainy seasons in Kenya. *Theor. Appl. Climatol.*, **58 (1-2)**, 57–69.

Cane, M. A., A. C. Clement, A. Kaplan, Y. Kushnir, D. Pozdnyakov, R. Seager, S. E. Zebiak, and R. Murtugudde, 1997: Twentieth-century sea surface temperature trends. *Science*, **275 (5302)**, 957–960.

Carr, M. and C. Bretherton, 2001: Convective momentum transport over the tropical Pacific: Budget estimates. *J. Atmos. Sci.*, **58 (13)**, 1673–1693.

Chang, E. K., S. Lee, and K. L. Swanson, 2002: Storm track dynamics. *J. Climate*, **15 (16)**, 2163–2183.

Chen, J., B. E. Carlson, and A. D. Del Genio, 2002: Evidence for strengthening of the tropical general circulation in the 1990s. *Science*, **295 (5556)**, 838–841.

Chiang, J. and S. Zebiak, 2000: Surface wind over tropical oceans: Diagnosis of the momentum balance, and modeling the linear friction coefficient. *J. Climate*, **13**, 1733–1747.

Chou, C. and J. Neelin, 2003: Mechanisms limiting the northward extent of the northern summer monsoons over North America, Asia, and Africa. *J. Climate*, **16 (3)**, 406–425.

Chou, C. and J. D. Neelin, 2001: Mechanisms limiting the southward extent of the South American summer monsoon. *Geophys. Res. Lett.*, **28 (12)**, 2433–2436.

Clement, A. C., R. Seager, M. A. Cane, and S. E. Zebiak, 1996: An ocean dynamical thermostat. *J. Clim.*, **9**, 2190–2196.

Colas, F., J. C. McWilliams, X. Capet, and J. Kurian, 2012: Heat balance and eddies in the Peru-Chile current system. *Clim. Dyn.*, **39**, 509–529.

Compo, G. P. and P. D. Sardeshmukh, 2010: Removing ENSO-related variations from the climate record. *J. Climate*, **23 (8)**, 1957–1978.

Conway, D., C. Hanson, R. Doherty, and A. Persechino, 2007: GCM simulations of the Indian Ocean dipole influence on East African rainfall: Present and future. *Geophys. Res. Lett.*, **34 (3)**, L03 705.

Cook, B. I. and R. Seager, 2013: The response of the North American Monsoon to increased greenhouse gas forcing. *J. Geophys. Res. Atmos.*, **118 (4)**, 1690–1699.

Cook, K. H. and E. K. Vizy, 2013: Projected changes in East African rainy seasons. *J. Climate*, **26 (16)**, 5931–5948.

Dai, A. and K. Trenberth, 2002: Estimates of freshwater discharge from continents: Latitudinal and seasonal variations. *J. Hydrometeorol.*, **3**, 660–687.

Davey, M. and A. Gill, 1987: Experiments on tropical circulation with a simple moist model. *Quart. J. Roy. Meteor. Soc.*, **113 (478)**, 1237–1269.

de Boyer Montegut, C., G. Madec, A. S. Fischer, A. Lazar, and D. Iudicone, 2004: Mixed layer depth over the global ocean: An examination of profile data and a profile-based climatology. *J. Geophys. Res. Oceans*, **109**, C12 003.

Dee, D., et al., 2011: The ERA-Interim reanalysis: Configuration and performance of the data assimilation system. *Quart. J. Roy. Meteor. Soc.*, **137 (656)**, 553–597.

Deser, C., 1993: Diagnosis of the surface momentum balance over the tropical Pacific Ocean. *J. Climate*, **6 (1)**, 64–74.

Deser, C., A. S. Phillips, and J. W. Hurrell, 2004: Pacific interdecadal climate variability: Linkages between the tropics and the North Pacific during boreal winter since 1900. *J. Climate*, **17 (16)**, 3109–3124.

Dima, I., J. Wallace, and I. Kraucunas, 2005: Tropical zonal momentum balance in the NCEP reanalyses. *J. Atmos. Sci.*, **62**, 2499–2513.

Dutra, E., L. Magnusson, F. Wetterhall, H. L. Cloke, G. Balsamo, S. Boussetta, and F. Pappenberger, 2013: The 2010-2011 drought in the Horn of Africa in ECMWF reanalysis and seasonal forecast products. *Int. J. Climatol.*, **33 (7)**, 1720–1729.

Emanuel, K., J. David Neelin, and C. Bretherton, 1994: On large-scale circulations in convecting atmospheres. *Quart. J. Roy. Meteor. Soc.*, **120 (519)**, 1111–1143.

FEWS NET, 2011: East Africa: Past year one of the driest on record in the eastern Horn. U.S. Agency for International Development, Washington, D.C.

Findlater, J., 1969: A major low-level air current near the Indian Ocean during the northern summer. *Quart. J. Roy. Meteor. Soc.*, **95 (404)**, 362–380.

Fu, X. and B. Wang, 1999: The role of longwave radiation and boundary layer thermodynamics in forcing tropical surface winds. *J. Climate*, **12 (4)**, 1049–1069.

Funk, C., M. D. Dettinger, J. C. Michaelsen, J. P. Verdin, M. E. Brown, M. Barlow, and A. Hoell, 2008: Warming of the Indian Ocean threatens eastern and southern African food security but could be mitigated by agricultural development. *Proc. Natl. Acad. Sci.*, **105 (32)**, 11 081–11 086.

Gill, A., 1980: Some simple solutions for heat-induced tropical circulation. *Quart. J. Roy. Meteor. Soc.*, **106 (449)**, 447–462.

Goddard, L. and N. E. Graham, 1999: Importance of the Indian Ocean for simulating rainfall anomalies over eastern and southern Africa. *J. Geophys. Res. Atmos.*, **104**, 19,099–19,116.

Han, Z.-Y., T.-J. Zhou, and L.-W. Zou, 2012: Indian Ocean SST biases in a Flexible Regional Ocean Atmosphere Land System (FROALS) model. *Atmos. Ocean. Sci. Lett.*, **5 (4)**, 273–279.

Hastenrath, S., A. Nicklis, and L. Greischar, 1993: Atmospheric-hydrospheric mechanisms of climate anomalies in the western equatorial Indian Ocean. *J. Geophys. Res. Oceans*, **98**, 20,219–20,235.

Held, I. and B. Soden, 2006: Robust responses of the hydrological cycle to global warming. *J. Climate*, **19 (21)**, 5686–5699.

Herweijer, C. and R. Seager, 2008: The global footprint of persistent extra-tropical drought in the instrumental era. *Int. J. Climatol.*, **28 (13)**, 1761–1774.

Hoerling, M., et al., 2011: On North American decadal climate for 2011-20. *J. Climate*, **24 (16)**, 4519–4528.

Huang, B., Z. Z. Hu, and B. Jha, 2007: Evolution of model systematic errors in the tropical atlantic basin from coupled climate hindcasts. *Clim. Dyn.*, **28**, 661–682.

Huffman, G. J., R. F. Adler, D. T. Bolvin, and G. Gu, 2009: Improving the global precipitation record: GPCP version 2.1. *Geophys. Res. Lett.*, **36 (17)**.

Huffman, G. J., et al., 2007: The TRMM multisatellite precipitation analysis (TMPA): Quasi-global, multiyear, combined-sensor precipitation estimates at fine scales. *J. Hydrometeorol.*, **8 (1)**, 38–55.

Indeje, M., F. H. Semazzi, and L. J. Ogallo, 2000: ENSO signals in East African rainfall seasons. *Int. J. Climatol.*, **20**, 19–46.

Kalnay, E., et al., 1996: The NCEP/NCAR 40-year reanalysis project. *Bull. Amer. Meteor. Soc.*, **77 (3)**, 437–471.

Karnauskas, K., R. Seager, A. Giannini, and A. Busalacchi, 2013: A simple mechanism for the climatological midsummer drought along the Pacific coast of Central America. *Atmósfera*, **26 (2)**, 261–281.

Kelley, C., M. Ting, R. Seager, and Y. Kushnir, 2012: Mediterranean precipitation climatology, seasonal cycle, and trend as simulated by CMIP5. *Geophys. Res. Lett.*, **39 (21)**, L21 703.

Kiehl, J. T., J. J. Hack, G. B. Bonan, and B. Boville, 1996: Description of the NCAR community climate model(CCM 3). *Tech Note NCAR/TN-420+STR.*

Kinuthia, J. and G. Asnani, 1982: A newly found jet in North Kenya (Turkana Channel). *Mon. Wea. Rev.*, **110 (11)**, 1722–1728.

Kinuthia, J. H., 1992: Horizontal and vertical structure of the Lake Turkana jet. *J. of Appl. Meteorol.*, **31 (11)**, 1248–1274.

Kraucunas, I. and D. Hartmann, 2005: Equatorial superrotation and the factors controlling the zonal-mean zonal winds in the tropical upper troposphere. *J. Atmos. Sci.*, **62 (2)**, 371–389.

Laîné, A., H. Nakamura, K. Nishii, and T. Miyasaka, 2014: A diagnostic study of future evaporation changes projected in CMIP5 climate models. *Clim. Dynam.*, **42 (9-10)**, 2745–2761.

Lee, S., 1999: Why are the climatological zonal winds easterly in the equatorial upper troposphere? *J. Atmos. Sci.*, **56 (10)**, 1353–1363.

Lee, S. and I. M. Held, 1993: Baroclinic wave packets in models and observations. *J. Atmos. Sci.*, **50 (10)**, 1413–1428.

Levine, R. C., A. G. Turner, D. Marathayil, and G. M. Martin, 2013: The role of northern Arabian Sea surface temperature biases in CMIP5 model simulations and future projections of Indian summer monsoon rainfall. *Clim. Dyn.*, **41 (1)**, 155–172.

L'Heureux, M. L., S. Lee, and B. Lyon, 2013: Recent multidecadal strengthening of the Walker circulation across the tropical Pacific. *Nature Climate Change*, **3 (6)**, 571–576.

Li, G. and S. P. Xie, 2014: Tropical biases in CMIP5 multimodel ensemble: The excessive equatorial pacific cold tongue and double ITCZ problems. *J. Clim.*, **27**, 1765–1780.

Lin, J., B. Mapes, and W. Han, 2008: What are the sources of mechanical damping in Matsuno-Gill-type models? *J. Climate*, **21 (2)**, 165–179.

Lindzen, R. and A. Hou, 1988: Hadley circulations for zonally averaged heating centered off the equator. *J. Atmos. Sci.*, **45 (17)**, 2416–2427.

Lindzen, R. and S. Nigam, 1987: On the role of sea surface temperature gradients in forcing low-level winds and convergence in the tropics. *J. Atmos. Sci.*, **44 (17)**, 2418–2436.

Liu, L., S.-P. Xie, X.-T. Zheng, T. Li, Y. Du, G. Huang, and W.-D. Yu, 2013: Indian Ocean variability in the CMIP5 multi-model ensemble: the zonal dipole mode. *Clim. Dynam.*, **43 (5-6)**, 1715–1730.

Lott, F. C., N. Christidis, and P. A. Stott, 2013: Can the 2011 East African drought be attributed to human-induced climate change? *Geophys. Res. Lett.*, **40 (6)**, 1177–1181.

Lu, J., G. Vecchi, and T. Reichler, 2007: Expansion of the Hadley cell under global warming. *Geophys. Res. Lett*, **34**, L06 805.

Lyon, B., 2014: Seasonal drought in the Greater Horn of Africa and its recent increase during the March-May long rains. *J. Clim.*, **27**, 7953–7975.

Lyon, B., A. Barnston, and D. G. DeWitt, 2013: Tropical Pacific forcing of a 1998-99 climate shift: Observational analysis and climate model results for the boreal spring season. *Clim. Dynam.*, **43**, 893–909.

Lyon, B. and D. G. DeWitt, 2012: A recent and abrupt decline in the East African long rains. *Geophys. Res. Lett.*, **39 (2)**, L02 702.

Ma, D., W. Boos, and Z. Kuang, 2014: Effects of orography and surface heat fluxes on the south Asian summer monsoon. *J. Clim.*, **27 (17)**, 6647–6659.

Mason, S. J. and L. Goddard, 2001: Probabilistic precipitation anomalies associated with ENSO. *Bull. Amer. Meteor. Soc.*, **82 (4)**, 619–638.

Matsuno, T., 1966: Quasi-geostrophic motions in the equatorial area. *J. Meteor. Soc. Japan*, **44 (1)**, 25–42.

McCreary, J. P., P. K. Kundu, and R. L. Molinari, 1993: A numerical investigation of dynamics, thermodynamics and mixed-layer processes in the Indian Ocean. *Prog. Oceanogr.*, **31 (3)**, 181–244.

Mechoso, C., et al., 1995: The seasonal cycle over the tropical Pacific in coupled ocean-atmosphere general circulation models. *Mon. Weather Rev.*, **123**, 2825–2838.

Mitchell, T. D. and P. D. Jones, 2005: An improved method of constructing a database of monthly climate observations and associated high-resolution grids. *Int. J. Climatol.*, **25 (6)**, 693–712.

Murtugudde, R., R. Seager, and A. Busalacchi, 1996: Simulation of the tropical oceans with an ocean GCM coupled to an atmospheric mixed-layer model. *J. Clim.*, **9 (8)**, 1795–1815.

Murtugudde, R., R. Seager, and P. Thoppil, 2007: Arabian Sea response to monsoon variations. *Paleoceanography*, **22 (4)**, PA4217.

Mutai, C. C. and M. N. Ward, 2000: East African rainfall and the tropical circulation/convection on intraseasonal to interannual timescales. *J. Clim.*, **13 (22)**, 3915–3939.

Neelin, J., 1989: On the interpretation of the Gill model. *J. Atmos. Sci.*, **46**, 2466–2468.

Nicholson, S., 1996: A review of climate dynamics and climate variability in Eastern Africa. *The limnology, climatology and paleoclimatology of the East African lakes*, T. C. Johnson and E. O. Odada, Eds., Gordon and Breach, 25–56.

Nicholson, S. E., 2000: The nature of rainfall variability over Africa on time scales of decades to millenia. *Glob. Planet. Change*, **26 (13)**, 137–158.

Nicholson, S. E., 2011: *Dryland Climatology*. Cambridge Cambridge University Press, 528 pp.

Ogallo, L., 1988: Relationships between seasonal rainfall in East Africa and the southern oscillation. *J. Climatol.*, **8 (1)**, 31–43.

Okoola, R. E., 1999: A diagnostic study of the eastern Africa monsoon circulation during the northern hemisphere spring season. *Int. J. Climatol.*, **19 (2)**, 143–168.

Omondi, P., L. A. Ogallo, R. Anyah, J. M. Muthama, and J. Ininda, 2013: Linkages between global sea surface temperatures and decadal rainfall variability over Eastern Africa region. *Int. J. Climatol.*, **33 (8)**, 2082–2104.

Otieno, V. O. and R. Anyah, 2013: CMIP5 simulated climate conditions of the Greater Horn of Africa (GHA). part II: projected climate. *Clim. Dynam.*, **41 (7-8)**, 2099–2113.

Pierrehumbert, R. and K. Swanson, 1995: Baroclinic instability. *Annu. Rev. Fluid Mech.*, **27 (1)**, 419–467.

Pohl, B. and P. Camberlin, 2011: Intraseasonal and interannual zonal circulations over the equatorial Indian ocean. *Theor. Appl. Climatol.*, **104 (1-2)**, 175–191.

Privé, N. C. and R. A. Plumb, 2007a: Monsoon dynamics with interactive forcing. Part I: Axisymmetric studies. *J. Atmos. Sci.*, **64 (5)**, 1417–1430.

Privé, N. C. and R. A. Plumb, 2007b: Monsoon dynamics with interactive forcing. Part II: Impact of eddies and asymmetric geometries. *J. Atmos. Sci.*, **64 (5)**, 1431–1442.

Prodhomme, C., P. Terray, S. Masson, T. Izumo, T. Tozuka, and T. Yamagata, 2014: Impacts of Indian Ocean SST biases on the Indian Monsoon: as simulated in a global coupled model. *Clim. Dynam.*, **42 (1-2)**, 271–290.

Roeckner, E., et al., 1996: *The atmospheric general circulation model ECHAM-4: Model description and simulation of present-day climate*. Max-Planck-Institut fürr Meteorologie.

Roeckner, E., et al., 2006: Sensitivity of simulated climate to horizontal and vertical resolution in the ECHAM5 atmosphere model. *J. Climate*, **19 (16)**, 3771–3791.

Rudolf, B., A. Becker, U. Schneider, A. Meyer-Christoffer, M. Ziese, et al., 2010: GPCC status report December 2010. *GPCC, December*.

Russell, J. and T. Johnson, 2007: Little Ice Age drought in equatorial Africa: Intertropical Convergence Zone migrations and El Niño–Southern Oscillation variability. *Geology*, **35 (1)**, 21–24.

Schneider, E. K., 1996: A note on the annual cycle of sea surface temperature at the equator. *COLA Rep.*, **36**, 18pp.

Schneider, T. and S. Bordoni, 2008: Eddy-mediated regime transitions in the seasonal cycle of a Hadley circulation and implications for monsoon dynamics. *J. Atmos. Sci.*, **65 (3)**, 915–934.

Schreck, C. J. and F. H. M. Semazzi, 2004: Variability of the recent climate of eastern Africa. *Int. J. Climatol.*, **24**, 681–701.

Seager, R., 1991: A simple model of the climatology and variability of the low-level wind field in the tropics. *J. Climate*, **4 (2)**, 164–179.

Seager, R. and N. Henderson, 2013: Diagnostic computation of moisture budgets in the ERA-Interim reanalysis with reference to analysis of CMIP-archived atmospheric model data. *J. Climate*, **26 (20)**, 7876–7901.

Seager, R., N. Naik, and G. A. Vecchi, 2010: Thermodynamic and dynamic mechanisms for large-scale changes in the hydrological cycle in response to global warming. *J. Climate*, **23 (17)**, 4651–4668.

Seager, R., et al., 2007: Model projections of an imminent transition to a more arid climate in southwestern North America. *Science*, **316 (5828)**, 1181.

Shongwe, M. E., G. J. van Oldenborgh, B. van den Hurk, and M. van Aalst, 2011: Projected changes in mean and extreme precipitation in Africa under global warming. part II: East Africa. *J. Clim.*, **24**, 3718–3733.

Smith, T. M., R. W. Reynolds, T. C. Peterson, and J. Lawrimore, 2008: Improvements to NOAA's historical merged land-ocean surface temperature analysis (1880-2006). *J. Climate*, **21 (10)**, 2283–2296.

Sobel, A. H., J. Nilsson, and L. M. Polvani, 2001: The weak temperature gradient approximation and balanced tropical moisture waves. *J. Atmos. Sci.*, **58**, 3650–3665.

Suarez, M. and D. Duffy, 1992: Terrestrial superrotation: A bifurcation of the general circulation. *J. Atmos. Sci.*, **49 (16)**, 1541–1554.

Taylor, K. E., R. J. Stouffer, and G. A. Meehl, 2012: An overview of CMIP5 and the experiment design. *Bull. Amer. Meteor. Soc.*, **93 (4)**, 485–498.

Tierney, J. E., J. E. Smerdon, K. J. Anchukaitis, and R. Seager, 2013: Multidecadal variability in East African hydroclimate controlled by the Indian Ocean. *Nature*, **493 (7432)**, 389–392.

Tomas, R. A. and P. J. Webster, 1997: The role of inertial instability in determining the location and strength of near-equatorial convection. *Quart. J. Roy. Meteor. Soc.*, **123 (542)**, 1445–1482.

Trewartha, G. T., 1961: *The Earth's Problem Climates*. University of Wisconsin Press Madison, 334 pp.

Vecchi, G. A. and B. J. Soden, 2007: Global warming and the weakening of the tropical circulation. *J. Climate*, **20 (17)**, 4316–4340.

Verschuren, D., K. R. Laird, and B. F. Cumming, 2000: Rainfall and drought in equatorial east Africa during the past 1,100 years. *Nature*, **403 (6768)**, 410–414.

Vizy, E. K. and K. H. Cook, 2012a: Mid-twenty-first-century changes in extreme events over northern and tropical Africa. *J. Climate*, **25 (17)**, 5748–5767.

Vizy, E. K. and K. H. Cook, 2012b: Mid-twenty-first-century changes in extreme events over northern and tropical Africa. *J. Climate*, **25 (17)**, 5748–5767.

Waithaka, M., G. C. Nelson, T. S. Thomas, and M. Kyotalimye, 2013: East African agriculture and climate change. *Int. Food Policy Res. Inst. Briefs*, **76**, URL `http://www.ifpri.org/publication/east-african-agriculture-and-climate-change`.

Wang, B. and T. Li, 1993: A simple tropical atmosphere model of relevance to short-term climate variations. *J. Atmos. Sci.*, **50 (2)**, 260–260.

Wang, C., L. Zhang, and S. Lee, 2014: A global perspective on CMIP5 climate model biases. *Nat. Clim. Chang.*, **4**, 201–205.

Wilks, D. S., 2011: *Statistical methods in the atmospheric sciences*. Academic press, 704 pp.

Williams, A. P. and C. Funk, 2011: A westward extension of the warm pool leads to a westward extension of the Walker circulation, drying eastern Africa. *Clim. Dynam.*, **37 (11-12)**, 2417–2435.

Xie, P. and P. A. Arkin, 1997: Global precipitation: A 17-year monthly analysis based on gauge observations, satellite estimates, and numerical model outputs. *Bull. Amer. Meteor. Soc.*, **78 (11)**, 2539–2558.

Yang, W., J. Nie, P. Lin, and B. Tan, 2007: Baroclinic wave packets in an extended quasigeostrophic two-layer model. *Geophys. Res. Lett.*, **34 (5)**, L05 822.

Yang, W., R. Seager, and M. A. Cane, 2013: Zonal momentum balance in the tropical atmospheric circulation during the global monsoon mature months. *J. Atmos. Sci.*, **70 (2)**, 583–599.

Yang, W., R. Seager, M. A. Cane, and B. Lyon, 2014a: The annual cycle of the East African precipitation. *J. Clim.*, **Under review**.

Yang, W., R. Seager, M. A. Cane, and B. Lyon, 2014b: The East African long rains in observations and models. *J. Climate*, **27 (19)**, 7185–7202.

Zebiak, S., 1990: Diagnostic studies of Pacific surface winds. *J. Climate*, **3**, 1016–1031.